Electron dynamics in surface acoustic wave devices

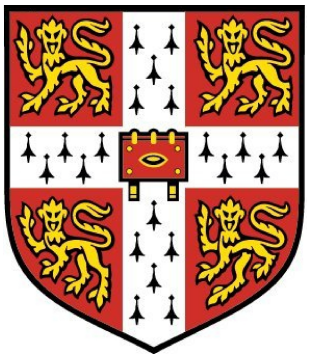

Adam Leslie Thorn

Gonville and Caius College

University of Cambridge

A thesis submitted for the degree of

Doctor of Philosophy

March 2009

Acknowledgements

A number of people have offered invaluable assistance to me throughout the course of my thesis. I would firstly like to express my thanks to my supervisor, Crispin Barnes; this work would not have been possible without him and he has been a source of much advice and support. I also enjoyed many discussions with Masaya Kataoka and Chris Ford, both of whom provided me with a great deal of guidance, and I thank Daniel Oi for introducing me to a number of interesting concepts. I also acknowledge funding from the Engineering and Physical Sciences Research Council.

A significant part of this work involved running computer simulations, and I have relied heavily upon resources provided by the CamGrid project to do this. Thanks also go to Frank Lee for his continual assistance with all of my computing troubles.

I am very grateful to all of my friends at the Cavendish, without whom my time there would have been far less enjoyable – in particular: Mike, Lee, Jenny, Jon G., Rob, Jon P., Vicki, Sam, and all the members of the SP curry club. I would also like to thank all of the members of the Caius Ultimate Frisbee team for providing me with a non-Physics-based distraction.

Finally, I thank all of the people who have offered me immeasurable friendship and support: Wei, Thomas, Tammy, Jennifer and – last but certainly not least – my family.

Declaration

The work presented in this thesis was carried out at the Semiconductor Physics Group in the Cavendish Laboratory, University of Cambridge between October 2004 and March 2009.

This dissertation is the result of my own work and includes nothing which is the outcome of work done in collaboration except where specifically indicated in the text. It has not been submitted in whole or in part for any degree at this or any other university, and is less than sixty thousand words long.

Abstract

Gallium arsenide is piezoelectric, so it is possible to generate coupled mechanical and electrical surface acoustic waves (SAWs) by applying a high-frequency voltage to a transducer on the surface of GaAs. By combining SAWs with existing low-dimensional nanostructures one can create a series of dynamic quantum dots corresponding to the minima of the travelling electric wave, and each dot carries a single electron at the SAW velocity ($\sim$ 2800 m/s). These devices may be of use in developing future quantum information processors, and also offer an ideal environment for probing the quantum mechanical behaviour of single electrons.

This thesis describes a numerical and theoretical study of the dynamics of an electron in a range of geometries. The numerical techniques for solving the time-dependent Schrödinger equation with an arbitrary time-dependent potential will be described in Chapter 2, and then applied in Chapter 3 to calculate the transmission of an electron through an Aharonov-Bohm (AB) ring. It will be seen that an important property of the techniques used in this thesis is that they can be easily adapted to study realistic geometries, and we will see features in the AB oscillations which do not arise in simplified analytic descriptions.

In Chapter 4, we will then study a device consisting of two parallel SAW channels separated by a controllable tunnelling barrier. We will use numerical simulations to investigate the effect of electric and magnetic fields upon the electron dynamics, and develop an analytic model to explain the simulation results. From the model, it will be apparent that it is possible to use this device to rotate the state of the electron to an arbitrary superposition of the first two eigenstates.

We then introduce coherent and squeezed states in Chapter 5, which are excited states of the quantum harmonic oscillator. Coherent and squeezed electronic states may be of use in quantum information processing, and could also arise due to unwanted perturbations in a SAW device. We will discuss how these states

can be controllably generated in a SAW device, and also discuss how they could then be detected.

In Chapter 6 we describe how to use the motion of a SAW to create a rapidly-changing potential in the frame of the electron, leading to a nonadiabatic excitation. The nonadiabatically-excited state oscillates from side to side within a 1D channel on a few-picosecond timescale, and this motion can be probed by placing a tunnelling barrier at one side of the channel. Numerical simulations will be performed to show how this motion can be controlled, and the simulation results will be seen to be in good agreement with recent experimental work performed by colleagues. Finally, we will show that this device can be used to measure the initial state of an electron which is an arbitrary superposition of the first two eigenstates.

Contents

Those who are not shocked when they first come across quantum theory cannot possibly have understood it.

Niels Bohr

1 Introduction

1.1 Quantum information processing

In 1936, Turing [1] laid the foundations for much of modern computer science when he introduced what is now generally called a Turing Machine (TM). Turing introduced TMs in order to study the notion of computability. Although this is a difficult notion to define formally, intuitively a problem is computable if one can define a series of instructions (i.e., an algorithm) which will result in the completion of the task if followed. The Church-Turing thesis states that a TM can perform any computable task, and so Turing Machines have proven to be of great interest in computer science.

A TM consists of a number of components. Firstly, they have a tape which can in principle be of infinite length. The tape is divided into a series of cells each of which can contain a letter taken from some finite alphabet. A head is able to read and write symbols on the tape, and can also move left and right along the tape. At any stage in the algorithm the machine is in one of a finite

number of states, and the behaviour of the system depends upon both the current state and the symbol read at the current position of the head. Thus, one step of an algorithm might be of the form: given that the current state is 16, if the symbol under the head is "A" then move one position left and change to state 23, whilst if the current symbol is "B" then change it to "C" and change to state 7. Despite the apparent simplicity of this description, all modern computers can be thought of as Turing Machines (although a TM may have an unlimited amount of storage space, so not all TMs are physically realisable). The majority of digital computers use binary logic and so use an alphabet consisting of only two symbols, typically labelled 0 and 1.

There exist many problems which could in principle be solved using a conventional computer but would in practice take an impractically long time to solve. An oft-cited example is finding the prime factors of large composite numbers; the difficulty of finding such factors is the basis for the widely-used RSA encryption algorithm [2]. Another problem which is very difficult to solve using classical computers is the simulation of many-body quantum mechanical systems, because the computational time required quickly increases with the number of particles considered. This is because the state of an ensemble of N particles each with m accessible quantum levels is described by a m^N dimensional complex vector, and so the Hamiltonian is represented as an m^N by m^N matrix.

One of the main reasons for simulating physical systems (quantum mechanical ones or otherwise) is that it is possible to investigate the effect of a range of assumptions and abstractions in order to develop a simple model for a seemingly complicated system. It may also be difficult to probe the system experimentally, perhaps because the characteristic length or time scales of the problem are difficult to access. Simulations may also provide information which cannot even in principle be found experimentally – for example, a simulation of a quantum system might provide the full wavefunction $|\psi\rangle$ whereas any measurable quantity depends only upon the probability density $|\langle\psi|\psi\rangle|^2$.

None the less, instead of simulating a quantum mechanical system one could in principle take the quantum system and measure its properties, thereby making use of quantum mechanical behaviour to acquire the desired information. This observation led Feynman [3] to suggest the possibility of a general quantum me-

chanical processor, or *quantum computer*, which exploits quantum mechanical phenomena to both store data and perform operations on that data. These ideas were further developed by Deutsch [4], and quantum algorithms for solving some problems which are in practice intractable using classical computers have been developed – for example, Shor's algorithm [5] for factoring large numbers and Grover's algorithm [6] for searching a database. The basic unit of information in a quantum computer is the quantum bit, or qubit, which is an arbitrary superposition of two quantum states: $\alpha|0\rangle + \beta|1\rangle$. Although there have also been proposals for quantum computation schemes based on d-level quantum systems, known as qudits, these will not be discussed here. As was remarked upon earlier, a system of N entangled qubits is extremely difficult to simulate classically because of the large Hilbert space needed to describe it, but this is also the origin of the power of quantum computers.

All physical manipulations of quantum states are written as unitary matrices: single qubit operations are most easily visualised using the Bloch sphere representation (see Section (1.1.1)), whilst an example of a two-qubit operation is the CNOT (controlled-NOT) gate: this gate flips the state of the second (or target) qubit if the first (or control) qubit is $|1\rangle$ whilst leaving it unchanged if the control qubit is $|0\rangle$. This operation can be written in a matrix representation:

$$U_{CNOT} = \begin{pmatrix} 1 & 0 & 0 & 0 \\ 0 & 1 & 0 & 0 \\ 0 & 0 & 0 & 1 \\ 0 & 0 & 1 & 0 \end{pmatrix} \tag{1.1}$$

where the basis is $|00\rangle$, $|01\rangle$, $|10\rangle$, $|11\rangle$ (the state $|ij\rangle$ corresponds to the first and second qubits having state $|i\rangle$ and $|j\rangle$ respectively). DiVincenzo [7] suggested a set of five criteria which must be satisfied by any realistic implementation of a quantum processor:

- **The existence of a well-defined two-level system**, such as the two spin states of a spin-$\frac{1}{2}$ particle, which are used to represent the states $|0\rangle$ and $|1\rangle$.

- **Initialisation:** it must be possible to prepare a known quantum state prior to the quantum computation, such as the ground state.
- **Measurement:** it must be possible to measure the state of a single qubit.
- **Universal set of gates:** it must be possible to controllably perform an arbitrary unitary transformation. It can be shown [8] that single qubit rotations about two orthogonal axes combined with the CNOT gate provides a universal set of gates.
- **Coherence:** the system must not be subject to excessive decoherence (for example, through interactions with the surrounding environment) over the course of the computation.

From these five criteria it is seen that the development of quantum information processing (QIP) is intimately linked to many aspects of fundamental quantum mechanics. Studying QIP thus not only offers great potential for future computing devices but is of importance for understanding fundamental quantum mechanics. This thesis will be concerned with a theoretical and computational study of electron dynamics in semiconductor nanostructures, and in particular we will study devices which use acoustic waves travelling across the surface of GaAs to transport single electrons. The remainder of this chapter will introduce the properties of these semiconductor devices, as well as examining some further motivating factors for studying these systems and then explaining the motives behind using a theoretical approach.

1.1.1 Bloch sphere representation

The Bloch sphere is a convenient geometric representation of a two-level quantum system and so will be used in much of the work that follows. Noting that global phase factors have no observable effects, an arbitrary two-level state can be written

$$|\psi\rangle = \cos\left(\frac{\theta}{2}\right)|0\rangle + e^{i\phi}\sin\left(\frac{\theta}{2}\right)|1\rangle \tag{1.2}$$

where $0 \leq \theta < \pi$ and $0 \leq \phi < 2\pi$ define a point on a three-dimensional unit sphere with the $|0\rangle$ and $|1\rangle$ basis states at the poles (see Fig. 1.1). θ and ϕ are

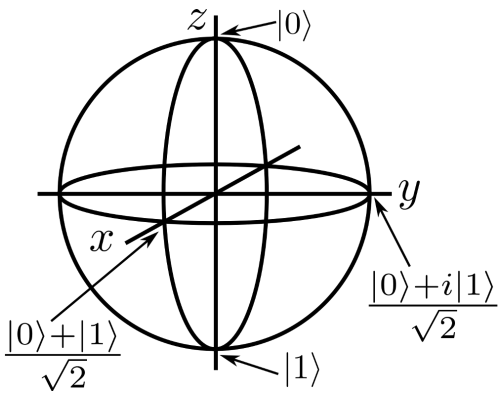

Figure 1.1: Bloch sphere representation of a two-level system.

the conventional angles in spherical polar co-ordinates. This mapping is possible because there is a homomorphism between $SO(3)$ and $SU(2)$ (specifically, $SU(2)$ is a double cover of $SO(3)$, which is the reason why Eq. (1.2) uses $\theta/2$ rather than θ). The generators of $SU(2)$ are the Pauli matrices,

$$\sigma_x = \begin{pmatrix} 0 & 1 \\ 1 & 0 \end{pmatrix}, \sigma_y = \begin{pmatrix} 0 & -i \\ i & 0 \end{pmatrix}, \sigma_z = \begin{pmatrix} 1 & 0 \\ 0 & -1 \end{pmatrix}. \tag{1.3}$$

The Bloch sphere description allows us to represent any unitary operation (up to a global phase change) as a rotation on the Bloch sphere: a rotation through an angle χ about the unit vector $\boldsymbol{n}$ is given by [8]

$$R_n(\chi) = e^{-i\chi \boldsymbol{n}\cdot\boldsymbol{\sigma}/2} = \mathbb{I}\cos\frac{\chi}{2} - i\boldsymbol{n}\cdot\boldsymbol{\sigma}\sin\frac{\chi}{2} \tag{1.4}$$

where $\boldsymbol{\sigma} = (\sigma_x, \sigma_y, \sigma_z)$. This also shows that the Pauli matrix σ_i produces a rotation about the ith axis of the Bloch sphere. Much of the work in this thesis will be concerned with solving the time-dependent Schrödinger equation (TDSE), and the formal solution to the TDSE involves the exponent of the Hamiltonian (which can be written as a linear combination of the σ_i). Equation (1.4) will therefore allow us to easily interpret the time evolution geometrically.

1.1.2 Unconventional quantum computing

The scheme for quantum computation discussed above requires one to perform a series of well-defined unitary operations on an initial quantum state. Other schemes, often referred to as "unconventional" quantum computing, have also been studied as possible ways of creating a quantum information processor, and we briefly discuss two such schemes here.

Adiabatic quantum computing

If a quantum system is initially in the ground state of a Hamiltonian which is then varied with time, it will remain in the instantaneous ground state if the time evolution is slow enough (i.e., adiabatic) [9]. This is a consequence of the quantum adiabatic theorem, which will be discussed in more detail in Chapter 6. Farhi *et al.* [10] proposed that this fact could be used to solve quantum computation problems. One begins with a system in the ground state of a Hamiltonian H_i which is easy to reach, for example by thermal relaxation. The system is then changed smoothly with time so that the Hamiltonian becomes H_f, where H_f is carefully chosen to have a ground state which encodes the solution to the problem being considered. Although the original problem considered in Ref. [10] was an optimisation problem, Aharonov *et al.* [11] showed that adiabatic quantum computation is equivalent to standard quantum computation. Experimental demonstrations of adiabatic quantum computation include solving an optimisation problem [12], simulating a Heisenberg spin chain [13], implementing Grover's algorithm [14] and factoring a composite number [15].

Geometric quantum computing

A major practical problem in building a working quantum computer is decoherence, which can rapidly introduce errors into a calculation. One of the fundamental operations in QIP is controllably changing the phase of a quantum state. Holonomic quantum computation [16] performs a global rotation of a quantum state vector without locally rotating it as seen in Fig. (1.2). This requires the adiabatic transport of a state vector around some loop in a curved Hilbert space.

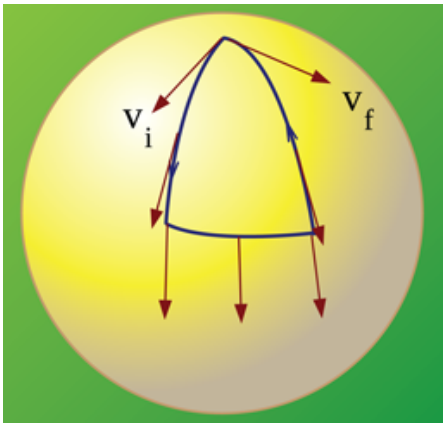

Figure 1.2: Illustration of "global rotation without local rotation". The state vector (shown in red) is adiabatically transported around a closed loop (blue) on the surface of a sphere in such a way that the angle between the vector and each loop segment is constant. The final vector V_f is rotated with respect to the initial vector V_i, so a "global rotation" has occurred. Taken from Ref. [24].

The angle between the state vector and a segment of the loop is constant (so there is no local rotation) but the final state is rotated with respect to the initial state (so a global rotation has been performed). This rotation is equivalent to performing a unitary transformation [17]; the transformation depends only upon the geometric properties of the loop and is independent of the time taken to traverse the loop. Also, because the transformation is a property only of the geometry of the loop, it is insensitive to local errors. For example, the spin of an electron may experience a randomly fluctuating magnetic field from nearby nuclei. Although this alters the dynamical phase of the electron, it may be possible to counteract this – for example, by using spin-echo techniques in the case of NMR [18, 19]. The geometric phase acquired is not affected by the fluctuating magnetic field, so geometric quantum computation is resilient against some of the errors which are a problem in conventional quantum computing. A number of physical systems have been considered for implementing a geometric quantum computer, including the optical manipulation of atoms [20] and ions [21], or solid state systems such as Josephson junctions [22] and GaAs quantum dots [23].

♦

Both of these unconventional quantum computing schemes rely upon the adiabatic manipulation of a quantum state. In Chapter 6 it will be seen that the issue of what exactly constitutes an adiabatic transformation in quantum mechanics is unclear at present. Some consequences of nonadiabatic evolution will then be investigated, and it will be seen that nonadiabatic transitions can produce states which may themselves be useful as a QIP resource.

1.2 Classical and quantum physics

Although quantum mechanics is an extremely successful mathematical theory, some unresolved issues still exist concerning its physical interpretation. Macroscopic objects obey the laws of classical mechanics, which has a number of fundamental differences with quantum mechanics. Some of the mathematical structure of quantum mechanics has direct analogues in classical mechanics – for example, some quantum mechanical Hamiltonians can be "derived" (in some sense) from classical mechanics by promoting the classical degrees of freedom to Hermitian operators. Although the correspondence principle [25] states that when quantum numbers become large the behaviour of quantum systems reproduces classical physics, it is unclear how to fully describe the transition from quantum to classical mechanics.

The quantum-to-classical transition is closely related to the so-called measurement problem in quantum mechanics. There are a range of quantum measurement frameworks which describe different regimes, such as the von Neumann projective measurement, quantum non-demolition measurements [26] and weak measurements [27]. However, the question of what precisely occurs when a quantum system is measured is still not fully answered, as exemplified by the Schrödinger's cat and Wigner's friend gedankenexperiments. In general terms, a measurement must somehow involve the transfer of information from the measured system to an observer, and by "observer" one normally means a macroscopic classical object (whether it be some piece of apparatus such as a photodiode or ammeter, or a person). Thus, understanding the processes that occur when a quantum system is measured requires an understanding of the interface between the quantum and classical worlds.

It will be seen in Chapter 5 that Gaussian quantum mechanical wavepackets possess a number of properties which are very similar to classical particles. Studying Gaussian wavepackets may yet shed light upon the quantum measurement problem (see Ref. [28] for a review and introduction), and Gaussian wavepackets also appear frequently in many branches of quantum information processing because they are the ground state of harmonic oscillators. The theme of studying Gaussian wavepackets will reappear throughout this thesis, and we will encounter a number of ways in which they can be created, manipulated and measured.

1.3 Semiconductor devices

Having given some motivation for the study of quantum mechanical systems, we now turn to the topic of using physical systems to investigate some of the issues we have raised. It has been proposed that qubits could be made in a range of physical systems, including devices based on NMR [29, 30], ion traps [31], superconductors [32], semiconductor devices [33] and linear optics [34]. This thesis will focus on semiconductor devices, which have a number of advantages compared to other material systems. Because semiconductors form the basis of almost all modern electronics there exists a great deal of mature technology to fabricate complicated semiconductor devices. Also, an important consideration for future QIP devices is the scalability of the underlying technology – any practical quantum computer must consist of many qubits, and so it must be possible to scale any physical implementation from one to many qubits. Again, given the breadth of existing knowledge concerning the fabrication of semiconductor devices they present an attractive avenue for QIP research.

The devices we will consider in this work are based upon GaAs/$Al_xGa_{1-x}As$ heterostructures (where $x \approx 0.3$) which have a two-dimensional electron gas (2DEG) near to the GaAs/AlGaAs interface. A typical example of a heterostructure is illustrated in Fig. 1.3. These heterostructures are created by molecular beam epitaxy (MBE), which can deposit atomic monolayers of different substances onto a wafer. GaAs has a zincblende crystal structure, which consists of a face centered cubic (f.c.c.) lattice of Ga atoms, with another f.c.c. lattice of As atoms displaced by $(\frac{1}{4}, \frac{1}{4}, \frac{1}{4})$ from this. AlGaAs has a crystal structure identical to

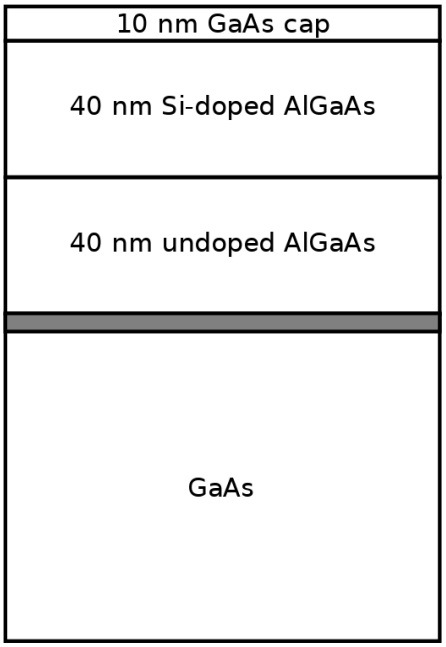

Figure 1.3: A typical heterostructure. A 2DEG forms in the grey region.

this, but with some fraction of the Ga sites occupied by Al. The lattice constant of $Al_{0.3}Ga_{0.7}As$ (5.65564 Å) is almost the same as that of GaAs (5.6533 Å) [35]. This discrepancy is small enough that there is very little mismatch between layers of GaAs and AlGaAs which would otherwise induce strain into the structure. This in turn would produce an unwanted electrostatic field due to the piezoelectric nature of GaAs (this piezoelectricity forms the basis for the production of surface acoustic waves, to be discussed in Section (1.4)).

MBE is also used to selectively dope the AlGaAs with Si where it acts as an n-type dopant because some of the Si dopants thermally ionise to donate electrons. These electrons migrate to the interface between the GaAs and AlGaAs layers – AlGaAs has a larger bandgap than GaAs, so the conduction band in GaAs is offset to be at a lower energy than the conduction band in AlGaAs. The extra negative charge that accumulates at the GaAs/AlGaAs interface causes the bands to bend, creating an approximately triangular well. The Si dopant density is chosen so that only the lowest eigenstate of this well lies below the Fermi energy of the electrons confined there, leading to the formation of a two-dimensional

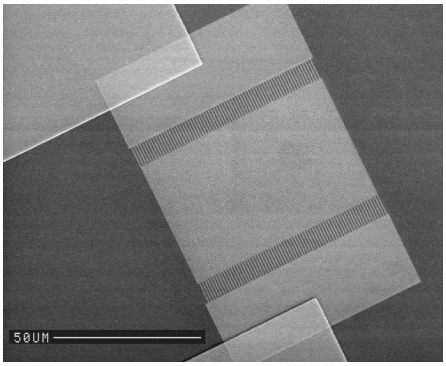

Figure 1.4: Scanning electron microscope image of a SAW transducer. Image courtesy of Mike Astley.

electron gas (2DEG). It should be noted that the Si donors are separated from the 2DEG by an undoped AlGaAs layer, which decreases the scattering between electrons in the 2DEG and the ionised donors.

1.4 Surface acoustic wave devices

Rayleigh [36] showed that it is possible to create acoustic waves which travel along the surface of an elastic material; the amplitude of these surface acoustic waves (SAWs) generally decays approximately exponentially with depth. Because GaAs is piezoelectric it is possible to generate SAWs in GaAs with an oscillating electric field. SAWs can be generated in practice by applying a radio-frequency voltage to an interdigitated transducer deposited on the surface of GaAs; a scanning electron microscope image of a SAW transducer is shown in Fig. (1.4). The wavelength of the generated SAW is determined by the spacing of the transducer fingers, and the SAW wavelength used throughout this work is $\lambda = 1$ μm. The speed of SAWs in GaAs is $v_{SAW} \simeq 2800$ m/s, and the relation $v = f\lambda$ then sets the frequency at $f \simeq 2.8$ GHz.

SAW transducers can be integrated with low-dimensional nanostructures, and a schematic diagram of a SAW device is shown in Fig. (1.5). The SAW travels across the surface of the semiconductor and encounters an etched mesa containing a 2DEG, typically 90 nm below the surface. Surface gates are deposited on the

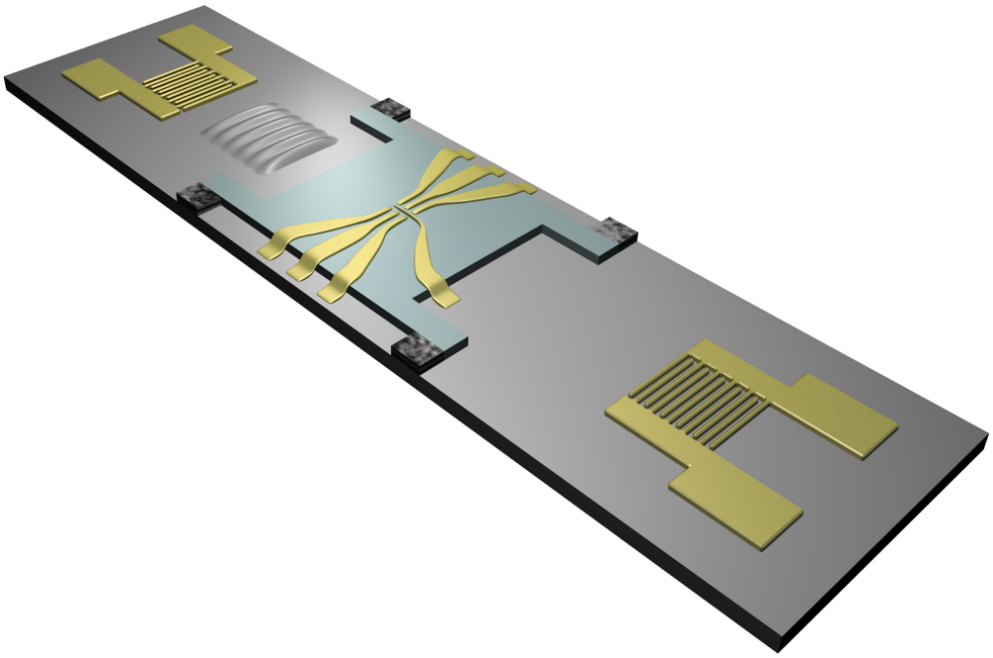

Figure 1.5: Illustration of a SAW device (not to scale). Transducers are located at both ends of the chip and generate SAWs when a radio-frequency voltage is applied to them. A mesa (shown in blue) is defined by an etch, and gold surface gates are then deposited on the mesa to define quasi-one-dimensional channels.

mesa; when a negative voltage is applied to these gates they will deplete electrons from the 2DEG beneath them. A simple example of a SAW device uses a pair of gates separated by a narrow gap (a split gate) to create a quasi one dimensional channel (Q1DC). SAWs can capture electrons from a 2DEG and transport them through a pinched-off Q1DC, and by tuning the SAW power and split gate voltage it is possible to ensure that each SAW minimum contains precisely N electrons for integer values of N. This produces a quantised current $I = Nef$ which leads to possible metrological applications [37–39]. The combination of a travelling SAW and a gate-defined channel leads to the formation of a series of dynamic quantum dots, and the fact that it is possible to carry precisely one electron in each of these dynamic quantum dots also means that they are a useful system for studying QIP, as discussed in the following section.

1.4.1 SAW quantum computer

Barnes *et al.* [40] proposed that SAW devices could be used for quantum information processing purposes. Their proposal is based upon using electrons transported in SAW minima as qubits, using either the spin or charge of the electrons. In the case of a spin qubit, the spin of an electron transported in a single SAW channel forms the qubit. It was proposed that single qubit operations could be performed through the application of local magnetic fields via nanomagnets (the fabrication of which is demonstrated in Ref. [41]), and two-qubit operations could be performed by having two parallel SAW channels meet at a controllable tunnel barrier. At the tunnel barrier the spins of neighbouring qubits would entangle, and the interaction could be controlled by varying the voltages applied to the gates defining the tunnel barriers. To read out the spins of the qubits at the end of the device, two possibilities exist. If a hole gas is fabricated at the end of the device, thereby forming a lateral np junction, the electrons carried by the SAW will recombine with the holes in this region generating polarised photons [42]. Gell *et al.* [43] have measured SAW-mediated light emission from a lateral np junction, and this work could be extended further to implement the proposal of Ref. [42]. Alternatively, Elzerman *et al.* [44] have measured the spin of an electron confined in a static quantum dot through spin-to-charge conversion. The electron

to be measured is allowed to tunnel onto the dot by lowering a tunnel barrier, and upon raising this barrier the electron is then trapped in the dot. A perpendicular magnetic field is also applied to lift the energy degeneracy of the two spin states. The Fermi energy of a 2DEG outside a tunnel barrier is tuned to be between the Zeeman-split levels, so one spin species is able to tunnel from the dot whilst the other is trapped there. The charge contained in the dot therefore depends upon the spin of the electron, and the charge state of the dot can be monitored by measuring the conductance of a 1D channel adjacent to it [45]. The conductance of such a channel is highly sensitive to changes in electrostatic potential, so if an electron leaves the dot there is a measurable change in the 1D conductance. Such a scheme could be incorporated into a SAW spin qubit device to measure the final spin state of the electrons.

Alternatively, a single electron which can be present in one of two parallel channels could be used as a charge qubit. The two logical qubit states correspond to the electron being in one channel or the other. Qubit rotations are performed in a similar manner to the spin qubit case, by having parallel SAW channels meet at a controllable tunnel barrier. Depending on which pair of channels meet, this corresponds to either a single-qubit rotation or a two-qubit rotation between neighbouring qubits. This scheme is depicted in Fig. (1.6). Region A of the figure illustrates a two qubit interaction, where two neighbouring qubits meet at a barrier. The two qubits interact via the Coulomb interaction, but the tunnel barrier between the channels is large enough to suppress tunnelling across the barrier. Regions B and C in Fig. (1.6) perform single qubit rotations. Measuring the final state of the qubits in this scheme is straightforward, as it only requires measurement of the current exiting each SAW channel. A novel scheme for performing charge-based quantum information processing in SAW devices will also be presented in Chapter 6.

The coherent manipulation of electrons has previously been demonstrated in a number of solid state systems, including quantum dots [46, 47] and superconductors [48, 49]. Bordone *et al.* [50] have also performed some preliminary numerical simulations of electron dynamics in two-channel SAW devices. There are two main advantages to using SAW devices as the basis of a quantum computer. Firstly, each successive SAW minimum is an independent quantum processor, so

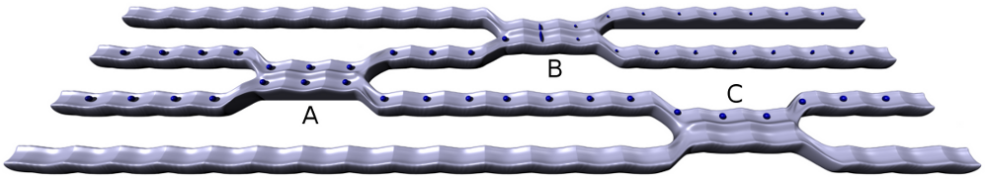

Figure 1.6: Schematic diagram of two SAW charge qubits. The top two channels form the first qubit and the bottom two channels form the second. Blue dots represent electron probability density. Region A: two-qubit interaction. Regions B and C: single qubit rotation.

given typical SAW operating frequencies of ~ 3 GHz billions of nominally identical operations are performed each second. This therefore allows the possibility of dealing with some error mechanisms by averaging the results from many successive calculations. Secondly, in principle such devices are reasonably easy to scale, as incorporating more qubits only requires the fabrication of more parallel SAW channels.

1.5 Motivation for a theoretical study

Experimental investigations of semiconductor devices have only a limited range of available probes – for example, when measuring SAW devices one normally measures the electrical current flowing through a gate-defined channel. This current may depend upon a multitude of experimental variables, including the voltages applied to each gate, the SAW amplitude, the temperature of the device, an externally applied magnetic field, or other parameters which may be either controllable or uncontrollable. Interpreting the effect of these external parameters on the quantum mechanical evolution of an electron is thus an extremely difficult task.

Performing simulations of the electron dynamics in nanostructures by numerically solving the Schrödinger equation can provide information which is not experimentally accessible, including complete knowledge of the electron wave function. From the wave function it is possible to calculate the probability that an electron is to be found in one region or another, which in turn allows one to predict the

flow of electrical currents. The results of such numerical simulations can thus be easily compared to experimental results, but the advantage of the simulation is that it allows one to see the underlying quantum mechanical origins of experimentally accessible quantities. For example, a simulation may show that changing a gate voltage leads to some particular excitation of the wave function, and hence a change in the measured current. Performing theoretical simulations in parallel with experimental measurements is thus an effective route to understanding.

Solving the time-dependent Schrödinger equation numerically with a general time-dependent potential is a daunting prospect. Typical experimental methodology requires measuring how properties of the system change as a function of many input parameters. In order to compare the simulation results to the measured data, the simulations need to be performed for thousands of different parameter values. Given that the timescale for performing a single simulation is of the order of hours, such an investigation requires the use of significant computational resources. The simulations presented in this thesis therefore rely heavily upon resources provided by the CamGrid project, which uses the Condor software [51] to provide a computational cluster of approximately 1000 processors.

1.6 Outline of work

In Chapter 2 the numerical techniques which are used to perform the numerical calculations in the rest of this thesis will be presented. Finite-differencing methods will be used to find a suitable representation of the Hamiltonian, and the Crank-Nicolson algorithm will be used to calculate quantum mechanical time evolution. These numerical techniques will then be applied to Aharonov-Bohm rings in Chapter 3; although these have been the subject of theoretical study in the past, the numerical techniques used in this work can be used to study effects which only arise in realistic geometries. In particular, we will see the effect of the Lorentz force upon Aharonov-Bohm oscillations, as well as the effect of gradually including higher-order interference processes.

Following this, in Chapter 4 we will discuss a SAW device consisting of two parallel channels separated by a controllable barrier. A detailed numerical investigation will be performed into the effect of firstly applying an electric field across

the channels, and secondly applying a perpendicular magnetic field. It will be seen from the numerical simulations that this leads to coherent oscillation of an electron wavefunction between the channels, and a theoretical model to explain this will be developed – the effect of the magnetic field will be included in this model via an infinitesimal Aharonov-Bohm effect. From this model, it will be seen that it is possible to perform an arbitrary single-qubit rotation of an electron in the two-channel SAW device using a geometry similar to a Mach-Zehnder interferometer.

Chapter 5 will study coherent and squeezed states, which are represented by Gaussian wavepackets. Although these states have been the subject of much study in quantum optics, their electronic analogues have received comparatively little attention. We will discuss how to generate these states in practice in SAW devices, as well as extending the simulations performed in Chapter 4 to determine what effect using these states has upon the coherent oscillations in a two-channel SAW device. The results will show a distinctive pattern for the current from the two SAW channels, which will be interpreted in light of the theoretical model in the preceding chapter.

In Chapter 6, we will see that it is possible to use a SAW device to create a rapidly-changing potential in the rest frame of an electron carried by the SAW; this leads to a nonadiabatic excitation of the electron. The SAW is used to create a series of dynamic quantum dots which are weakly coupled to a reservoir via a tunnelling barrier. The nonadiabatically-excited state oscillates from side to side within the dot, leading to a prediction of oscillatory behaviour in the tunnelling current through the barrier. In order to test this idea, the results of numerical simulations will be compared to experimental measurements performed by Masaya Kataoka and Mike Astley [52]. The tunnelling current will be seen to depend upon the coupling between the reservoir and the dynamic dot, as well as upon the low-energy spectrum of the dynamic dot. Both of these quantities depend upon the voltages applied to the gates which define the tunnelling region, and the dot spectrum will also change in a perpendicular magnetic field. Numerical simulations which account for the effect of the gate voltages will be performed, and we will find good agreement between the simulations and the experimental data. The behaviour of the tunnelling-current oscillations in a perpendicular magnetic

field will be explained using an analytic result for the low-energy spectrum of the dynamic dot.

We will then discuss potential applications of this tunnel barrier device in QIP, focussing especially upon using the device to measure the state of an electron. Numerical simulations will show that the tunnelling current discussed above provides information about the initial state of the electron: this current depends upon both the initial electron state and the suddenness of the change in the potential prior to the tunnelling region. In transitioning from an adiabatic to a nonadiabatic change in the potential, a smooth evolution in the behaviour of the tunnelling current will be seen. The tunnel barrier device can therefore be used to probe the initial electron state across a wide parameter space, and it can also be used to provide an indication of how nonadiabatic the change in potential is. Finally, Chapter 7 will summarise the work and suggest some potential avenues for future research.

Hilbert space is a big place

Carlton Caves

2 Numerical Methods

2.1 Introduction

One of the main goals of this work is to calculate numerical solutions of the time-dependent Schrödinger equation (TDSE). We are interested in the dynamics of an electron in 2D; the heterostructures discussed in Section (1.3) confine electron motion in the z direction so we will only consider motion in the 2D plane parallel to a heterojunction interface. For a single spinless particle, the TDSE is

$$H\psi(x,y,t) = -\frac{\hbar^2\nabla^2}{2m}\psi(x,y,t) + V(x,y,t)\psi(x,y,t) = i\hbar\frac{\partial\psi(x,y,t)}{\partial t} \tag{2.1}$$

The formal solution to Eq. (2.1) is

$$\psi(t) = U(t)\psi(0) \tag{2.2}$$

where

$$U(t) = T \exp\left(-\frac{i}{\hbar}\int_0^t H(s)ds\right) \tag{2.3}$$

is the time evolution operator (TEO), and T is the time-ordering operator. To solve Eq. (2.1) numerically, one must deal with the spatial and temporal derivatives in the Schrödinger equation separately. The techniques that will be used throughout this thesis will be presented in this chapter, and the methods that will be used to calculate an appropriate time-dependent potential in realistic SAW devices will then be discussed. Finally, we will review alternative techniques that have been used to numerically solve the TDSE and discuss why they are not well-suited to the problems considered in this work.

2.2 1D diffusion equation

The techniques we will use are best illustrated by considering the 1D diffusion equation, which shares many similarities with Eq. (2.1). The 1D diffusion equation for a density u and diffusion constant D is

$$\frac{\partial u}{\partial t} = D\frac{\partial^2 u}{\partial x^2} \tag{2.4}$$

If u and D in Eq. (2.4) are allowed to be complex, we arrive at the 1D TDSE for a particle in free space (Eq. (2.1) with $V = 0$).

We now represent the function $u(x,t)$ by its values at a discrete set of points $x_i = x_0 + i\delta x$, where δx is the grid spacing and i is an integer. We also discretise the time domain into steps of length δt, so that $t_n = n\delta t$. We will then define $u_i^n = u(x_i, t_n)$. In the following discussion, either the time or space index of u_i^n may be omitted for clarity if we are concerned only with the spatial or temporal variation of u. We next consider the Taylor expansions

$$u(x+\delta x) = u(x) + \delta x\frac{\mathrm{d}u}{\mathrm{d}x} + \frac{\delta x^2}{2!}\frac{\mathrm{d}^2u}{\mathrm{d}x^2} + \ldots \tag{2.5}$$

$$u(x-\delta x) = u(x) - \delta x\frac{\mathrm{d}u}{\mathrm{d}x} + \frac{\delta x^2}{2!}\frac{\mathrm{d}^2u}{\mathrm{d}x^2} + \ldots \tag{2.6}$$

$$\tag{2.7}$$

from which we see

$$\frac{\mathrm{d}^2u(x)}{\mathrm{d}x^2} \simeq \frac{u(x+\delta x) - 2u(x) + u(x-\delta x)}{\delta x^2} \tag{2.8}$$

or in the notation introduced above,

$$\frac{\mathrm{d}^2u_i}{\mathrm{d}x^2} \simeq \frac{u_{i+1} - 2u_i + u_{i-1}}{\delta x^2}. \tag{2.9}$$

The right hand side of Eq. (2.4) can therefore be written as the product of a matrix with a vector:

$$\delta x^2 \frac{\mathrm{d}^2u}{\mathrm{d}x^2} \rightarrow \begin{pmatrix} -2 & 1 & & & & \\ 1 & -2 & 1 & & & \\ & 1 & -2 & 1 & & \\ & & 1 & -2 & 1 & \\ & & & & \ddots & \end{pmatrix} \begin{pmatrix} u_1 \\ u_2 \\ u_3 \\ u_4 \\ \vdots \end{pmatrix} \tag{2.10}$$

where only the non-zero elements of the matrix are shown. The matrix form of the derivative in Eq. (2.10) is known as the finite-differenced representation. We also need to specify the boundary conditions – we will only be concerned with Dirichlet boundary conditions, and specifically the so-called hard wall condition that $u_L = u_R = 0$ where the grid is defined such that $x_i \in [x_L, x_R]$. This condition is imposed by setting the elements of the matrix in the finite-differenced representation of the differential operator which correspond to the boundaries equal to zero.

An important factor that must be considered in any numerical solution of a differential equation is the stability of the chosen algorithm, and we will use a von Neumann [53] analysis to investigate stability. Although other methods of stability analysis exist (see Ref. [54] for example), the von Neumann analysis is relatively straightforward to perform and interpret. This method considers the evolution of a general Fourier mode of the solution, so we write

$$u_j^n = \xi^n e^{ikj(\delta x)} \tag{2.11}$$

where k is a wavenumber, and $\xi = \xi(k)$ is a complex number referred to as the amplification factor. By substituting the solution (2.11) into Eq. (2.4), it can be seen that the time evolution of this Fourier mode is given by the integer powers of ξ. Thus, if $|\xi(k)| > 1$ for any value of k, there will be a Fourier mode of the solution which grows exponentially with time and so the solution scheme is unstable. The simplest schemes for performing the time discretisation of the 1D diffusion equation are

$$u_j^{n+1} - u_j^n = D(\delta t)\mathcal{L}u_j^n \tag{2.12}$$

$$u_j^{n+1} - u_j^n = D(\delta t)\mathcal{L}u_j^{n+1} \tag{2.13}$$

where

$$\mathcal{L}u^n = \frac{u_{j+1}^n - 2u_n^j + u_{j-1}^n}{\delta x^2} \tag{2.14}$$

The discretisations (2.12) and (2.13) (respectively called the forward-time and backward-time schemes) are identical, except for the time step at which the spatial derivative is taken on the right-hand side of the equation. In general, one will start with an initial condition $u(x, 0) = f(x)$ at time step $n = 0$, and then repeatedly use a rule such as (2.12) or (2.13) to find the solution at subsequent time steps. There is then an important difference between the forward- and backward-time schemes: determination of u^{n+1} requires only the multiplication of a vector by a matrix in the forward-time scheme of Eq. (2.12). However, in the backward-time scheme of Eq. (2.13) one must solve a system of linear equations to find u^{n+1} which is computationally demanding. Schemes of the former type are known as explicit schemes, as the solution at time step $n+1$ is given explicitly by knowledge of the solution at time step n. In contrast, schemes such as the backward-time method are known as implicit schemes. From substituting the solution (2.11) into the 1D diffusion equation, the amplification factor for the forward-time scheme can be shown to be [55]

$$\xi(k) = 1 - \alpha \sin^2\left(\frac{k\delta x}{2}\right) \tag{2.15}$$

where $\alpha = 4D\delta t/\delta x^2$. The forward-time scheme is therefore conditionally stable: $|\xi(k)| \leq 1$ if $2D\delta t/\delta x^2 \leq 1$. One can similarly determine the amplification factor for the backward-time scheme; it is

$$\xi(k) = \frac{1}{1 + 4\alpha \sin^2\left(\frac{k\delta x}{2}\right)} \tag{2.16}$$

Given that $\alpha > 0$ and $\sin^2\theta > 0$ for all θ, $\xi(k) \leq 1$ for all values of δx and δt: the backward-time scheme is unconditionally stable. However, the time evolution schemes given by Eqs. (2.12) and (2.13) are only first-order accurate in time. The accuracy can be improved by using the Crank-Nicolson (CN) method [56] which is both unconditionally stable and second-order accurate in time. The CN method can be thought of as the average of the forward- and backward-time schemes:

$$u_j^{n+1} - u_j^n = \frac{D\delta t}{2\delta x^2}\left[(u_{j+1}^n - 2u_j^n + u_{j-1}^n) + (u_{j+1}^{n+1} - 2u_j^{n+1} + u_{j-1}^{n+1})\right] \tag{2.17}$$

and then separately grouping the terms that depend upon u^{n+1} and u^n,

$$u_j^{n+1} - \frac{D\delta t}{2\delta x^2}\left[(u_{j+1}^{n+1} - 2u_j^{n+1} + u_{j-1}^{n+1})\right] = u_j^n + \frac{D\delta t}{2\delta x^2}(u_{j+1}^n - 2u_j^n + u_{j-1}^n) \tag{2.18}$$

The amplification factor for the CN scheme is [55]

$$\xi = \frac{1 - 2\alpha \sin^2\left(\frac{k\delta x}{2}\right)}{1 + 2\alpha \sin^2\left(\frac{k\delta x}{2}\right)} \tag{2.19}$$

and so the scheme is stable for all δx and δt.

Although the CN scheme is implicit, determining u^{n+1} from u^n is relatively straightforward due to the sparse nature of the matrix in Eq. (2.10). Equation (2.18) can be written as the matrix equation $Au^{n+1} = Bu^n$, where the matrix A has the tridiagonal form of Eq. (2.10). Such a system of linear equations is computationally easy to solve using standard library routines.

2.3 2D Schrödinger equation

We now generalise the previous discussion of the 1D diffusion equation to the 2D Schrödinger equation. The move from 1D to 2D is straightforward, but introduces significant computational differences. We discretise the wavefunction $\psi(x, y, t)$ in a similar fashion to the way we discretised the solution to the diffusion equation $u(x, t)$: a rectangular grid with spacing δx (δy) in the x (y) direction is used, and the indexing system is defined by $x_j = x_0 + j\delta x$, $y_k = y_0 + k\delta y$, $t_n = n\delta t$. We then write $\psi^n_{j,k} \equiv \psi(x_0 + j\delta x, y_0 + k\delta y, n\delta t)$. The components of $\nabla^2\psi_{j,k}$ are the generalisations of Eq. (2.8):

$$\frac{\partial^2\psi_{j,k}}{\partial x^2} = \frac{\psi_{j+1,k} - 2\psi_{j,k} + \psi_{j-1,k}}{\delta x^2} \tag{2.20}$$

$$\frac{\partial^2\psi_{j,k}}{\partial y^2} = \frac{\psi_{j,k+1} - 2\psi_{j,k} + \psi_{j,k-1}}{\delta y^2} \tag{2.21}$$

The $V\psi$ term from Eq. (2.1) is replaced by $V^n_{j,k}\psi^n_{j,k}$, where $V^n_{j,k} \equiv V(x_j, y_k, t_n)$. If the spatial grid used has N points in the x direction and M points in the y direction, the discretised wavefunction will then be written as a vector of length NM. The first N elements of this vector are $\psi^n_{1,1}, \psi^n_{2,1} \ldots \psi^n_{N,1}$. The elements $N+1, N+2 \ldots 2N$ will be $\psi^n_{1,2}, \psi^n_{2,2} \ldots \psi^n_{N,2}$ and so on. The finite differenced form of the Hamiltonian H will be represented as an $NM \times NM$ matrix which acts on this vector. Taking for definiteness the case $N = 3$, $M = 4$, the product $H\psi$ is (setting $\hbar = 2m = 1$)

$$\begin{pmatrix}
\beta & \alpha_x & . & \alpha_y & & & & & & & & \\
\alpha_x & \beta & \alpha_x & . & \alpha_y & & & & & & & \\
. & \alpha_x & \beta & . & . & \alpha_y & & & & & & \\
\alpha_y & . & . & \beta & \alpha_x & . & \alpha_y & & & & & \\
 & \alpha_y & . & \alpha_x & \beta & \alpha_x & . & \alpha_y & & & & \\
 & & \alpha_y & . & \alpha_x & \beta & . & . & \alpha_y & & & \\
 & & & \alpha_y & . & . & \beta & \alpha_x & . & \alpha_y & & \\
 & & & & \alpha_y & . & \alpha_x & \beta & \alpha_x & . & \alpha_y & \\
 & & & & & \alpha_y & . & \alpha_x & \beta & . & . & \alpha_y \\
 & & & & & & \alpha_y & . & . & \beta & \alpha_x & . \\
 & & & & & & & \alpha_y & . & \alpha_x & \beta & \alpha_x \\
 & & & & & & & & \alpha_y & . & \alpha_x & \beta
\end{pmatrix}
\begin{pmatrix}
\psi^n_{1,1} \\ \psi^n_{2,1} \\ \psi^n_{3,1} \\ \psi^n_{1,2} \\ \psi^n_{2,2} \\ \psi^n_{3,2} \\ \psi^n_{1,3} \\ \psi^n_{2,3} \\ \psi^n_{3,3} \\ \psi^n_{1,4} \\ \psi^n_{2,4} \\ \psi^n_{3,4}
\end{pmatrix} \tag{2.22}$$

where $\alpha_x = 1/(\delta x)^2$, $\alpha_y = 1/(\delta y)^2$ and $\beta = -2(\alpha_x + \alpha_y) + V_{j,k}$. Elements which are zero are omitted from the matrix in (2.22).

We also need to ensure that we impose appropriate boundary conditions to the differential equation. Here we will always impose the Dirichlet boundary condition that the wavefunction is zero at the boundaries of the region, which corresponds physically to placing an infinitely high potential barrier around the computational domain. This is enforced by setting the matrix elements corresponding to positions on any of the boundaries to zero, but in practice we will always choose a spatial region which is sufficiently large to ensure that the wavefunction is never incident on a boundary. The matrix in (2.22) only has nonzero elements along 5 bands: the diagonal, those immediately above and below the diagonal, and those N above and below the diagonal. One must therefore treat this as a banded matrix with bandwidth $2N + 1$, and solving such a system of equations is computationally much more demanding than solving the tridiagonal system of equations that arose in the 1D case. For problems involving static potentials this is not a significant problem, but with time-dependent potentials this algorithm places significant demands on computational resources. However, in the following section we will describe a modification to the time evolution algorithm discussed above which simplifies the numerical calculations. Before doing so, we remark that an alternative method of arriving at the Crank-Nicolson method in the context of solving the Schrödinger equation is to make use of Cayley's form [55] for the TEO,

$$\exp(-iH(\delta t)/\hbar) \simeq (\mathbb{I} + iH(\delta t)/2\hbar)^{-1}(\mathbb{I} - iH(\delta t)/2\hbar) \tag{2.23}$$

and so the wave vectors at time steps n and $n+1$ are related by

$$\left(\mathbb{I} + \frac{iH(\delta t)}{2\hbar}\right)\psi^{n+1} = \left(\mathbb{I} - \frac{iH(\delta t)}{2\hbar}\right)\psi^{n} \tag{2.24}$$

which is clearly of the same form as Eq. (2.18). An important property of Cayley's form is that it ensures the TEO is unitary and so probability is conserved.

2.3.1 Split operator techniques

Split operator techniques can be used to greatly simplify the numerical solution of partial differential equations [54, 55]. The method relies upon writing a differential operator as a linear combination of N parts:

$$\mathcal{L}u = \mathcal{L}_1 u + \mathcal{L}_2 u + \cdots + \mathcal{L}_N u \tag{2.25}$$

where we wish to solve a general partial differential equation which is first order in time,

$$\frac{\partial u}{\partial t} = \mathcal{L}u \tag{2.26}$$

For each of the $\mathcal{L}_i$, we define $\mathcal{U}_i$ to be the operator that would perform the time evolution if $\mathcal{L}_i$ were the only operator on the right hand side of Eq. (2.26) – that is, if $\mathcal{L} = \mathcal{L}_i$ then

$$u^{n+1} = \mathcal{U}_i(u^n, \Delta t). \tag{2.27}$$

The process for performing a whole time step Δt for the entire operator in Eq. (2.25) is then to apply each of the evolution operators $\mathcal{U}_i$ in turn:

$$\begin{aligned} u^{n+1/N} &= \mathcal{U}_1(u^n, \Delta t) \\ u^{n+2/N} &= \mathcal{U}_2(u^{n+1/N}, \Delta t) \\ &\cdots \\ u^{n+1} &= \mathcal{U}_N(u^{n+(N-1)/N}, \Delta t) \end{aligned}$$

This technique can be adapted slightly to the form which will be used throughout this work – the alternating direction implicit technique. The $\mathcal{U}_i$ defined previously now include all the parts of the full operator $\mathcal{L}$ but is only required to be numerically stable for the $\mathcal{L}_i$ part of the operator (although when using the Crank-Nicolson method to perform the time evolution all of the operators are unconditionally stable). Thus, at any stage in the algorithm one of the $\mathcal{L}_i$ leads to an implicit set of linear equations whilst the other parts of $\mathcal{L}$ are handled explicitly. The process for performing a whole time step is the same as above,

except a series of fractional time steps $\Delta t/N$ are used:

$$\begin{aligned} u^{n+1/N} &= \mathcal{U}_1(u^n, \Delta t/N) \\ u^{n+2/N} &= \mathcal{U}_2(u^{n+1/N}, \Delta t/N) \\ &\cdots \\ u^{n+1} &= \mathcal{U}_N(u^{n+(N-1)/N}, \Delta t/N) \end{aligned}$$

In the context of solving the TDSE in two dimensions, the Laplacian operator is split into two parts: $\mathcal{L} = \mathcal{L}_x + \mathcal{L}_y$ where $\mathcal{L}_x = \partial^2/\partial x^2$, $\mathcal{L}_y = \partial^2/\partial y^2$. As only one of $\mathcal{L}_x$ or $\mathcal{L}_y$ is implicit at any stage in the algorithm each time step requires the solution of two tridiagonal systems similar to Eq. (2.10), which is a significantly faster operation than solving the band diagonal system (2.22).

2.3.2 Magnetic fields

Although Eq. (2.1) includes a time-varying electric potential, it will also be desirable to incorporate a static perpendicular magnetic field into the numerical simulations. We will use the magnetic vector potential $\boldsymbol{A} = (-By, 0, 0)$ which leads to the magnetic field $\boldsymbol{B} = (0, 0, B)$. In the presence of a magnetic field (and taking $V = 0$ for brevity), the quantum mechanical Hamiltonian for a particle of charge q is

$$H = \frac{1}{2m}\left(-i\hbar\nabla - q\boldsymbol{A}\right)^2 \tag{2.28}$$

$$= \frac{1}{2m}\left(-i\hbar\partial_x + qBy\right)^2 + \frac{1}{2m}(-i\hbar\partial_y)^2 \tag{2.29}$$

$$\frac{2ma^2}{\hbar^2}H = -\left(a\partial_x + \frac{iqBya}{\hbar}\right)^2 - a^2\partial_y^2 \tag{2.30}$$

where in Eq. (2.30) we have introduced the parameter a which has the dimension of length. Throughout this work, a is typically chosen to be 5 nm. We next make use of the approximation $\theta^2 \simeq 2\cosh\theta - 2$ which follows from the Taylor

expansion of $\cosh\theta$, and note that

$$\begin{aligned}\cosh(a\partial_y)\psi(x,y) &= \frac{1}{2}(e^{a\partial_y}+e^{-a\partial_y})\psi(x,y) &(2.31)\\ &= \frac{1}{2}\left(1+a\partial_y+\frac{a^2}{2}\partial_y^2\ldots\right)\psi(x,y)+\\ &\quad \frac{1}{2}\left(1-a\partial_y+\frac{a^2}{2}\partial_y^2\ldots\right)\psi(x,y) &(2.32)\\ &= \frac{1}{2}(\psi(x,y+a)+\psi(x,y-a)). &(2.33)\end{aligned}$$

Similarly, defining $\gamma = iqBya/\hbar$,

$$\begin{aligned}\cosh(a\partial_x+\gamma)\psi(x,y) &= \frac{1}{2}(e^{a\partial_x}e^{\gamma}+e^{-a\partial_x}e^{-\gamma})\psi(x,y) &(2.34)\\ &= \frac{1}{2}(e^{\gamma}\psi(x+a,y)+e^{-\gamma}\psi(x-a,y)). &(2.35)\end{aligned}$$

Combining Eqs. (2.33) and (2.35) with Eq. (2.30) leads to

$$\begin{aligned}\frac{2ma^2}{\hbar^2}H\psi(x,y) &= 4\psi(x,y)-\psi(x,y+a)-\psi(x,y-a)\\ &\quad -e^{iqBya/\hbar}\psi(x+a,y)-e^{-iqBya/\hbar}\psi(x-a,y) &(2.36)\end{aligned}$$

Equation (2.36) is known as Harper's equation and has been studied by Hofstadter [57] in the context of a 2D tight-binding model for a lattice with spacing a. It should also be noted that when $B = 0$, Eq. (2.36) reduces to the finite differenced Hamiltonian arising from Eqs. (2.20) and (2.21). Given this form for the spatial discretisation of the Hamiltonian, it is then possible to again apply the split operator techniques of Section (2.3.1) to perform the time evolution.

2.4 Lorentz transformation

Many of the simulations performed later in this thesis can be simplified by noting that an electron carried by a SAW is well-confined to one SAW minimum which then traverses a distance on the order of a few microns. The size of the computational domain can be greatly reduced by Lorentz transforming into the rest frame

of the SAW minimum which carries the electron, noting that $|\boldsymbol{v}| \ll c$ where $\boldsymbol{v}$ is the SAW velocity and c is the speed of light. Using unprimed symbols to represent quantities in the laboratory frame and primed symbols for the SAW frame (which moves at a speed v in the x direction relative to the laboratory frame), the electric potential ϕ and the components of the magnetic vector potential $\boldsymbol{A}$ transform as

$$\phi' = \gamma(v)\phi - \gamma(v)vA_x \tag{2.37}$$
$$A'_x = \gamma(v)A_x - \gamma(v)v\phi/c^2 \tag{2.38}$$
$$A'_y = A_y \tag{2.39}$$
$$A'_z = A_z \tag{2.40}$$

where $\gamma(v) = (1-v^2/c^2)^{-1/2}$ as usual. We will be using $v = 2700\,\mathrm{ms}^{-1}$ throughout this work, so can take $\gamma(v) = 1$ and $v/c^2 = 0$. However, even with these approximations Eq. (2.37) for the electric potential differs between the two frames in the presence of a non-zero magnetic vector potential $\boldsymbol{A}$, which will need to be included in the numerical simulations.

2.5 Electric potential

The electric potential experienced by electrons in a SAW device can be written as the sum of the potential due to the metallic surface gates and the potential due to the travelling SAW. The typical mode of operation of the SAW devices considered in this thesis involves using the surface gates to remove all of the charge in the 2DEG beneath them so that 1D channels are formed. The potential due to the gates is therefore given by the solution to Laplace's equation, $\nabla^2\phi(\boldsymbol{r}) = 0$, with appropriate boundary conditions. A full determination of the SAW potential requires the simultaneous solution of a wave equation for the mechanical wave with an equation describing the piezoelectric response of GaAs (Eqs. (2) and (3) of Ref. [58]), which in general is a difficult numerical problem. However, it will be seen that it is straightforward to use the calculated result for the SAW potential in the numerical simulations performed here.

2.5.1 Gate potential

Davies *et al.* [59] have demonstrated that it is possible to calculate the bare electrostatic potential due to voltages applied to an arbitrary pattern of polygonal surface gates. The method described in [59] uses a Fourier transform to solve Laplace's equation with the boundary condition $V = 0$ on the ungated surface. Their basic result considers an infinite triangle at a potential V_g with one edge along the x-axis and an angle $2A$ at the origin. The potential at the point $\boldsymbol{r}$ due to this infinite triangular region is then

$$\phi(\boldsymbol{r}) = \frac{V_g}{\pi} \arctan \frac{z \sin A}{(r - x)\cos A - y \sin A} \tag{2.41}$$

where $r^2 = x^2 + y^2 + z^2$. The xy plane is taken to be parallel to the plane of the 2DEG, and $z = 0$ at the surface and becomes increasingly positive into the semiconductor.

Equation (2.41) is useful because any simple polygon (one which does not intersect itself) can be decomposed into disjoint triangles. The process of decomposing a polygon into triangles requires one to find so-called "ears" of a polygon. If an N-sided polygon (or N-gon) has vertices labelled $p_1, p_2, \ldots p_N$, vertex p_i is an ear if the line joining p_{i-1} to p_{i+1} lies entirely within the polygon (note that the terms $i \pm 1$ are determined modulo N, so $p_{i+N} = p_i$). If vertex p_i is an ear, the triangle with vertices p_{i-1}, p_i, p_{i+1} can be removed to leave an $(N-1)$-gon. The process then continues with successively smaller polygons until the initial polygon has been entirely converted into triangles. Meisters' theorem [60] guarantees that this algorithm will be successful; it states that any polygon with more than 3 sides has at least two ears. Triangles will therefore be removed from the original N-gon until it is a quadrilateral, which always have two ears. This quadrilateral will decompose to a further two triangles (for a total of $N - 2$ triangles in general for an N-gon) at which point the algorithm terminates. An example of the decomposition of a hexagon into four triangles is illustrated in Fig. (2.1).

Given that any triangular gate can be created by superposing three infinite triangles (due to the linearity of Laplace's equation) as illustrated in Fig. (2.2), Eq. (2.41) can therefore be used to calculate the potential due to any polygonal

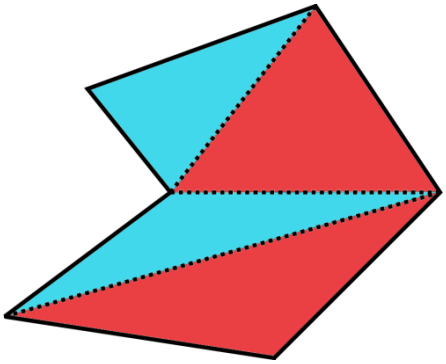

Figure 2.1: One possible decomposition of a hexagon into four distinct triangles.

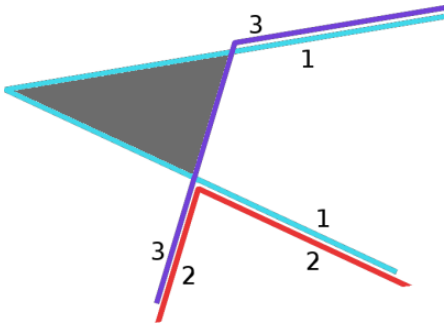

Figure 2.2: Three semi-infinite triangles are superposed to create a triangle (the semi-infinite triangles have been offset slightly for clarity). A voltage $-V_g$ is applied to the triangles with edges marked 1 (blue) and 2 (red), whilst a voltage $+V_g$ is applied to the triangle with edges marked 3 (purple). The grey triangle is then at voltage $-V_g$.

gate. It is also straightforward to obtain analytic expressions for the components of $\nabla\phi$ from Eq. (2.41) which will be useful in Section (2.5.3).

2.5.2 SAW potential

Aizin *et al.* [61] calculated the SAW potential analytically when a metal strip is placed across the surface of a semiconductor, so the metal partially screens the electric wave. The presence of the metal on the surface would also affect the propagation of the mechanical wave, though this is neglected in Ref. [61]. Their main result is that the electrical wave is approximately sinusoidal away from the metal strip and is a damped sinusoid under the metal. Rahman *et al.* [58]

later used finite-element methods to numerically solve the equations governing the SAW motion. An important advantage of such techniques is their ability to incorporate non-trivial geometries – the simulations are for a realistic split gate geometry with vacuum above the surface of the device. Although this leads to different behaviour from that found by Aizin *et al.* [61] for the SAW under the surface gates, away from the gates the result is qualitatively similar: the SAW is approximately sinusoidal with amplitude $O(10\text{ mV})$.

As we will only be concerned with the behaviour of electrons in the 1D channels formed between gates (i.e., not beneath the metal gates) in this thesis, a sinusoidal travelling wave will be used for the SAW potential. Previous theoretical work on the dynamics of electrons carried in SAWs (for example, the classical simulations of Robinson & Barnes [62] and the quantum mechanical simulations in Refs. [63, 64]) used a sinusoidal potential and were able to well reproduce many features seen experimentally in the quantisation of SAW currents. Also, Schneble *et al.* [65] have shown how to determine the amplitude of the SAW by measuring the conductance through a quantum dot as a function of the power applied to the SAW transducer. Using this technique, the typical SAW amplitude in the experimental device considered in Chapters 4 and 6 was estimated to be ∼50 mV [66]. The SAW amplitude used in the simulations in this thesis will therefore generally be a few 10s of mV.

2.5.3 Bicubic approximation

When using the results of Section (2.5.1) to calculate a potential for use in solving the 2D TDSE, some implementational difficulties arise. Equation (2.41) shows that calculating the gate potential requires the evaluation of many arctangent functions, which is a computationally expensive operation. The typical grid spacing used in the simulations will be ∼ 5–10 nm. However, the length scale on which the potential due to the gates can change is roughly the depth of the 2DEG. As this depth is 90 nm for the devices considered here, calculating the gate potential on a grid with a 5 nm spacing is expected to be unnecessary. Also, when working in the rest frame of the SAW it will in general be necessary to recalculate the potential due to the gates at each time step.

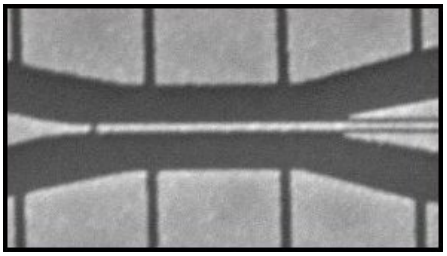

Figure 2.3: Scanning electron microscope image of the central region of the device to be studied in later chapters.

The time needed to calculate the electric potential can be greatly reduced by using a bicubic interpolation [55]. The gate potential is calculated on a grid which is relatively coarse compared to that used in solving the TDSE, and which covers the entire computational domain in the laboratory frame. Given a rectangular grid cell and the value of a function $f(x, y)$ at each corner, along with the values of the derivatives $\partial f/\partial x$, $\partial f/\partial y$ and $\partial^2 f/\partial x \partial y$, the bicubic interpolation returns an interpolated value f_i at any point within the cell. Two important properties of the interpolating function used here are that $f_i = f(x, y)$ at the grid points, and that in crossing from one cell to the next both f_i and its gradient are continuous.

The algorithm makes no guarantee about the accuracy of the interpolated function and so we now estimate this accuracy for the central region of the device which will be studied in Chapters 4 and 6 (see Fig. (2.3)). Ten thousand points are chosen at random within the central part of the device and the interpolated potential V_i is calculated at each point. The exact potential $V(x, y)$ is also calculated at these points, and the maximum relative difference $|V_i - V(x, y)|/V(x, y)$ is plotted in Fig. (2.4) for a range of grid spacings. The figure shows an approximately exponential dependence of the error on the grid spacing. An error of less than 0.01% is achieved using a grid spacing of 10 nm without placing a significant demand on computational time, so this spacing will be used whenever the potential due to a gate pattern is calculated.

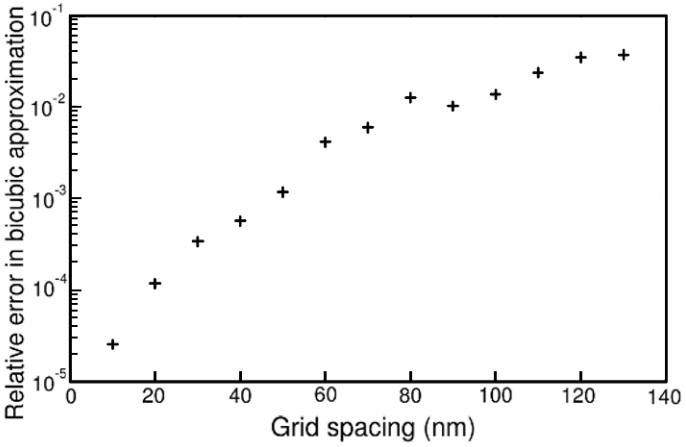

Figure 2.4: Error in bicubic approximation for the device depicted in Fig. (2.3).

2.6 Other numerical techniques

As well as the methods that have been described in this chapter, a number of other techniques exist for numerically solving the TDSE. Finite element methods (FEMs) have been applied to a range of differential equations [67], and Watanabe & Tsukada [68] applied finite element methods to the TDSE with a static potential. Finite element methods are well-suited to problems which possess a complicated geometry, rather than the simple rectangular grid used in the earlier derivation of the finite-difference method. However, a rectangular grid will be seen to be sufficient for all of the problems considered in this thesis, and the primary advantage of finite-difference methods over FEMs is that they are substantially simpler to implement.

There are also a number of techniques other than the Crank-Nicolson method which could be used to calculate the time evolution of a particle obeying the TDSE. The Crank-Nicolson method is accurate to second order in the time step [55], and Iitaka [69] derived some related schemes for solving the TDSE which are accurate to higher order. However, the methods they derive are only conditionally stable and also do not automatically ensure that the time evolution is unitary.

A higher-order accuracy can also be achieved by using Runge-Kutta methods to integrate the time derivatives (see, for example, Ref. [70]). Maksym [63] used

high-accuracy methods based upon the Crank-Nicolson algorithm [71] to calculate (to an accuracy of better than 1 part in 10^{10}) the transmission of an electron through a time-dependent barrier and applied the results to investigate current quantisation in a SAW device. It will later be seen that such high accuracy is not required for the problems considered in this thesis. Instead, the significant difficulty in performing the simulations in this work is that the time evolution will be calculated for thousands of different potentials (due to using many different gate voltages or magnetic field strengths in a similar manner to experimental measurements of semiconductor devices). The computation time needed for the simulations is therefore an extremely important factor, and it was seen that the alternating direction implicit method introduced in Section (2.3.1) is fast as it only requires the solution of tridiagonal matrix problems.

It is also possible to accurately represent the TEO as a linear sum of Chebyshev polynomials [72]; however, such techniques only give the wavefunction at the end of the time period considered and calculating the wavefunction at short time intervals is in practice very difficult. In contrast, methods such as the Crank-Nicolson algorithm calculate the wavefunction at each time step, and this will be of great use in interpreting the simulation results. A further disadvantage of using a Chebyshev polynomial representation is that these techniques are difficult to adapt to a time-dependent potential.

In summary, the choice of finite-difference methods in combination with the Crank-Nicolson algorithm has a number of advantages for this work. They are simple to implement, which reduces the likelihood of programming error. These methods also ensure that the time evolution is unitary and unconditionally stable, as well as being well-suited to problems with arbitrary time-dependent potentials. Finally, the problems considered in this thesis have a high-dimensional parameter space due to the fact that the devices are defined by many surface gates, each of which will in general have a different voltage applied. It is therefore necessary to use techniques which require relatively short computation time, and this condition is satisfied by the finite-difference and Crank-Nicolson methods.

We choose to examine a phenomenon which is impossible, absolutely impossible, to explain in any classical way, and which has in it the heart of quantum mechanics.

Richard Feynman

3

The Aharonov-Bohm Effect

3.1 Introduction

In this chapter we will introduce the Aharonov-Bohm (AB) effect, which is a quantum mechanical single-particle interference effect. We will review past theoretical and numerical work performed on AB rings in 2D nanostructures, and see that although the theoretical work we review can reproduce a number of the features seen in experiments, it does not fully take account of the geometry of physical AB rings. The numerical methods described in the previous chapter will therefore be applied to a realistic geometry, and two effects in particular will be studied: the effect of the Lorentz force, and incorporating trajectories that transit around the ring multiple times. The investigation of the latter effect will require the implementation of absorbing boundary conditions in order to render the problem computationally tractable. Although a number of methods for imposing such boundary conditions exist, they are typically non-Markovian and energy-dependent (which restricts their accuracy) and implementing them

in practice is difficult. We will therefore develop a straightforward implementation for absorbing boundary conditions in AB rings and similar geometries and demonstrate its accuracy.

3.2 The Aharonov-Bohm Effect

In Newtonian mechanics, the dynamics of a particle with charge q and mass m is described in terms of the electric field $\boldsymbol{E}$ and the magnetic field $\boldsymbol{B}$ through Newton's second law:

$$m\ddot{\boldsymbol{r}} = q(\boldsymbol{E} + \dot{\boldsymbol{r}} \times \boldsymbol{B}) \tag{3.1}$$

where $\boldsymbol{r}$ is the position vector of the particle. However, in the Lagrangian and Hamiltonian formulations of classical mechanics, the quantities that enter into the dynamical equations are the electric (scalar) potential ϕ and magnetic (vector) potential $\boldsymbol{A}$, defined such that $\boldsymbol{E} = -\nabla\phi$ and $\nabla \times \boldsymbol{A} = \boldsymbol{B}$ (we assume static magnetic fields for simplicity). The Lagrangian for this particle is then written in terms of ϕ and $\boldsymbol{A}$:

$$\mathscr{L} = \frac{1}{2}m|\dot{\boldsymbol{r}}|^2 - q(\phi - \dot{\boldsymbol{r}} \cdot \boldsymbol{A}) \tag{3.2}$$

It had been supposed that the magnetic potential was a purely mathematical tool until Aharonov & Bohm [73] showed that physically measurable effects can arise in regions where $\boldsymbol{B}$ is zero if $\boldsymbol{A}$ is non-zero. A charged particle which moves in a 4-vector potential $A_\mu = (\phi/c, \boldsymbol{A})$ acquires a phase S given by

$$S = \frac{q}{\hbar}\int A_\mu \mathrm{d}x^\mu = \frac{q}{\hbar}\int (\phi(t')\mathrm{d}t' - \boldsymbol{A} \cdot \mathrm{d}\boldsymbol{x})\,. \tag{3.3}$$

The effect of the magnetic potential can best be seen by considering the case where $\phi = 0$. We consider the case when a wavefunction splits into two equal parts which each take one of two paths Γ_1, Γ_2 which enclose a magnetic flux Φ between them as shown in Fig. (3.1). From Eq. (3.3), the phase acquired in

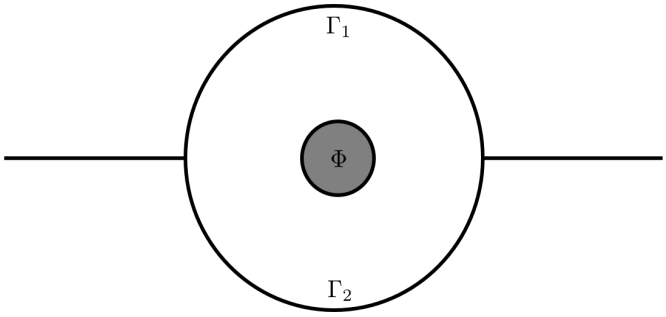

Figure 3.1: Geometry for the Aharonov-Bohm effect. Two paths Γ_1 and Γ_2 form a closed loop which encloses the magnetic flux Φ.

traversing path i ($i = 1, 2$) is

$$S_i = -\frac{q}{\hbar}\int_{\Gamma_i} \boldsymbol{A}\cdot \mathrm{d}\boldsymbol{x} \tag{3.4}$$

so the phase difference between the two parts of the wavefunction is

$$\Delta S = |S_2 - S_1| = \frac{q}{\hbar}\oint_{\Gamma} \boldsymbol{A}\cdot \mathrm{d}\boldsymbol{x} = \frac{q}{\hbar}\int_D \boldsymbol{B}\cdot \mathrm{d}\boldsymbol{S} = 2\pi\frac{q}{h}\Phi \tag{3.5}$$

having converted the line integral to a surface integral using Stokes' theorem and recalling that $\boldsymbol{B} = \nabla \times \boldsymbol{A}$. Γ is the closed loop formed by Γ_1 and Γ_2 and Φ is the magnetic flux through Γ (for a uniform magnetic field of magnitude B this will be $\Phi = BA$ where A is the area of the closed loop). There will therefore be constructive interference when $\Delta S = 2\pi n$ for integer n, whereas when $\Delta S = 2\pi(n+\frac{1}{2})$ the two paths destructively interfere and so the probability of transmission through the ring drops to zero. The conductivity of the ring will therefore exhibit periodic oscillations as a function of B.

From Eq. (3.5), it follows that the condition for constructive interference is $BA = nh/e$ (now taking $q = e$ for an electron); Fig. (3.2) illustrates the trajectories corresponding to $n = 1$ and $n = 2$. The $n = 1$ situation arises from two paths which each traverse one half of the ring, whilst $n = 2$ corresponds to one of the paths instead circling the ring one and a half times. Because the higher-order paths effectively enclose a greater area, the B-period of the conductance oscil-

lations decreases. The Fourier transform of the magnetoconductance therefore exhibits a number of peaks (for different values of n) typically referred to as h/ne oscillations. The presence of the higher-order h/ne oscillations requires phase coherence to be maintained over a longer time, and Hansen *et al.* [74] used this fact to determine the phase coherence length in an etched GaAs ring by measuring the amplitude of the first six Fourier peaks.

The AB effect has been experimentally investigated in a number of systems. The first experiment was performed by Chambers [75], using a metal whisker to provide the magnetic field. They took great care to ensure that the magnetic field outside the whisker was zero, so that any effect they measured had to be due to the magnetic vector potential rather than some effect of a Lorentz force acting upon the electrons. More recently, Webb *et al.* [76] examined transmission through 2D metal rings, whilst Timp *et al.* [77] and Ford *et al.* [78] performed experiments using GaAs heterostructures. The former used etched rings, whilst the latter used surface gates to define a ring. The Aharonov-Bohm effect is also relevant in other systems, such as antidots [79] and carbon nanotubes [80]. It should be noted that many of these experiments are not strictly measuring the originally proposed Aharonov-Bohm effect, as the charged particles experience a non-zero magnetic field. This introduces a Lorentz force, and the effect of this will be discussed in Section (3.5).

Also, AB rings have been of use in studying fundamental aspects of quantum mechanics. Buks *et al.* [81] used an Aharonov-Bohm ring with a quantum dot embedded in one arm to perform a "which path" measurement. A quantum point contact (QPC) adjacent to the dot was used as a charge detector: the presence of charge in the dot alters the electrostatic potential in that region, and the conductance of the QPC is highly sensitive to this [82]. Detecting the presence of charge in one arm of the ring provides "which path" information and so leads to a decrease in the AB oscillation amplitude. More recently, Chang *et al.* [83] performed similar measurements comparing the effect of performing a which-path measurement on the h/e and $h/2e$ oscillation amplitudes. They also measured a decrease in the amplitude of the h/e oscillation, but the effect of the measurement on the amplitude of the $h/2e$ oscillation is reduced because detecting charge in

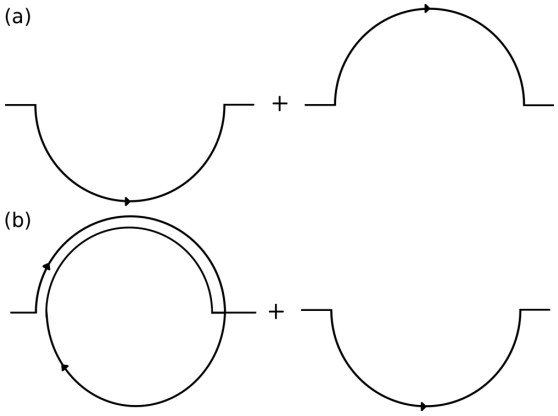

Figure 3.2: Examples of different trajectories in an AB ring. a) two paths each traverse half the ring, leading to an h/e oscillation. b) One path traverses the ring 1.5 times; if this interferes with a path traversing half of the ring it will lead to an $h/2e$ oscillation.

one arm does not necessarily provide which-path information in that case (see Fig. (3.2)).

3.3 Previous theoretical work

Büttiker *et al.* [84] derived a theoretical result for the transmission through an AB ring using an S-matrix approach. The geometry they studied consists of a ring connected to two leads, and they calculate the conductivity of the ring by considering the transmission and reflection probabilities between the ring and the leads. The model they use is one-dimensional (i.e. it neglects the fact that the leads and arms have non-zero width), and assumes that the transmission probability from the leads into either of the two arms of the ring is equal. This latter assumption is reasonable for metals, where the effect of the Lorentz force is smaller than in semiconductors due to the larger effective electron mass in metals.

Vasilopoulos *et al.* [85] generalised this model to allow for asymmetric scattering into the arms of the ring. The asymmetry is characterised by the ratio of the transmission amplitudes into either arm; the ratio of these two amplitudes is denoted λ, so that $\lambda = 1$ corresponds to the symmetric case whilst $\lambda = 0$ corresponds to injection into only one arm. Figure (3.3) shows the transmission

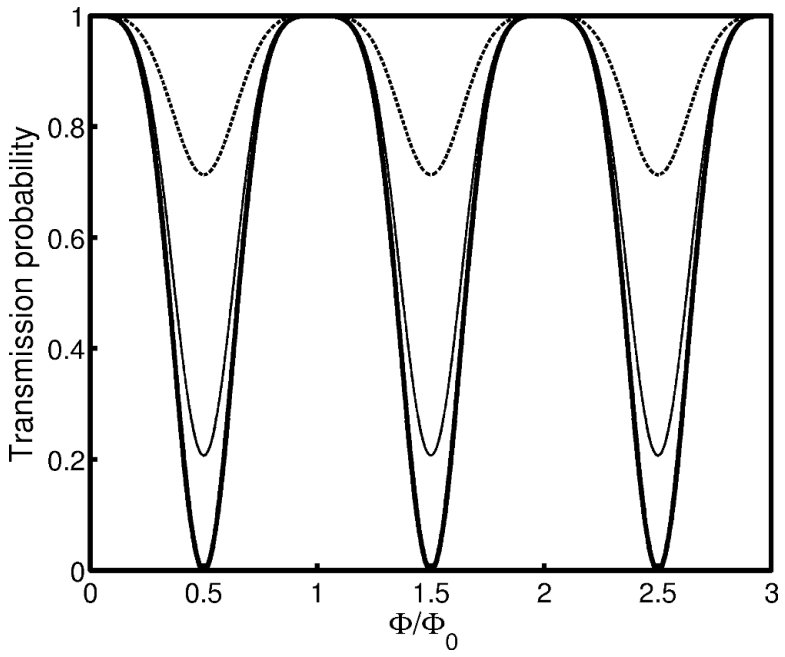

Figure 3.3: Results from theoretical model of AB oscillations in Ref. [85] as the flux enclosed Φ varies, for three values of the symmetry parameter λ described in the text. Thick line: $\lambda = 1$. Thin line: $\lambda = 0.75$. Dashed line: $\lambda = 0.5$. As the asymmetry is increased (i.e. smaller λ) the oscillation amplitude decreases.

probability through an AB ring for three values of λ (calculated using Eq. (8) of Ref. [85]). The transmission probability is periodic in the number of flux quanta $\Phi_0 = h/e$ enclosed as expected, and the oscillation amplitude also decreases as λ is decreased due to incomplete destructive interference – the Lorentz force leads to preferential injection into one arm. However, the asymmetry will in general be a geometry-dependent function of B and this is not easily accounted for in a model of this type.

Szafran & Peeters [86, 87] have performed numerical simulations to determine the transmission probability through AB rings. They expand the wavefunction using a basis of Gaussians centered at a series of points, and the locations of these points determines the geometry of the simulated device. Although this method can simulate some of the effects arising from a realistic geometry, it can only consider occupation of the lowest transverse subband. The numerical methods described in Chapter 2 can take full account of the geometry of the device, which

will be seen to lead to more complicated structure in the magnetoconductance of an AB ring.

3.4 Absorbing boundary conditions

The numerical methods presented in Chapter 2 use hard-wall boundary conditions. Although this is not a problem if the wavepacket is always well-confined, for open systems such as AB rings the wavefunction will reach the edge of the computational domain at some point in the simulation. When it does so it will reflect off the boundary leading to spurious interference effects, and so this restricts the time over which the electron dynamics can be simulated. Although this limit can be relaxed by using a larger computational domain, this leads to a substantial increase in the computational resources required and so may not be practical. A better solution is to use "absorbing" boundary conditions (ABCs) which (in the ideal case) have a reflection probability of zero, but implementing these is non-trivial.

The basic problem with implementing ABCs can be seen by considering the solution to the 1D Schrödinger equation for a plane wave $\psi = \exp(-i(\omega t - kx))$, which leads to the dispersion relation

$$\hbar k = \pm\sqrt{2m(\hbar\omega - V(x))} \tag{3.6}$$

where we assume a time-independent potential $V(x)$ which varies slowly on the length scale of the wavelength $\lambda = 2\pi/k$, and the positive (negative) solution corresponds to a right- (left-) going wave. We then need to transform Eq. (3.6) back into the space-time domain, which will lead to a differential equation given that $k \Leftrightarrow -i\partial/\partial x$, $\omega \Leftrightarrow i\partial/\partial t$ when Fourier transforming. The first problem that arises is that the square root in the right hand side of Eq. (3.6) is not a rational function and so needs to be approximated before the equation can be converted into a differential equation (Frensley [88] reviews the problem of boundary conditions in open systems, and in particular Appendix D discusses the time dependent Schrödinger equation). Shibata [89] uses a linear approximation and considers only the 1D problem, whilst Kuska [90] instead uses a rational function

approximation and also generalised to the 2D case. Both of these methods lead to an energy-dependent reflection coefficient at the boundaries. A further problem with these methods is that they are non-Markovian – in order to absorb the wave packet, full knowledge of its past state is required.

Conventional implementations of ABCs gradually remove the wavefunction from the system at each time step. For an Aharonov-Bohm ring, however, the wavepacket quickly breaks into separate packets. For example, shortly after the start of the simulation the wavepacket can be seen to consist of three distinct components: one portion which reflects from the ring back into the entrance lead, and one portion in each of the two arms. If the left-moving packet can be reliably identified it can then be removed from the problem. Although we discuss only the left lead here, an equivalent description applies to right-moving packets in the right lead. In order to identify discrete packets in the left lead, we begin by defining an integrated probability density

$$P_i = \int_{x_B}^{x_B+i(\delta x)} |\psi(x,y)|^2 \,\mathrm{d}x\,\mathrm{d}y \tag{3.7}$$

where x_B is the x-ordinate of the left edge of the domain, δx is the grid spacing in the x direction and i is an integer. The y integration is performed over the whole of the computational domain. Starting at $i = 0$ we calculate $P_{i+1} - P_i$ until i has become large enough that $x_B + i(\delta x)$ reaches the end of the lead. The condition for identifying a packet is $P_{i+1} - P_i < \epsilon_1$, and it was found in practice that the numerical simulations are more stable if a minimum threshold is set for the packet by using the condition $P_i > \epsilon_2$. The parameters ϵ_1 and ϵ_2 are both small, typically ~ 0.01, and the algorithm is illustrated in Fig. (3.4). It should be noted that this algorithm relies partly upon the fact that in the AB ring geometry, the part of the wavefunction which reflects back into the left lead consists only of left-moving components. If a packet is identified in this way it is removed by setting the wavefunction equal to zero in that region. This scheme is straightforward to implement, and in Section (3.5) the accuracy of this technique will be demonstrated.

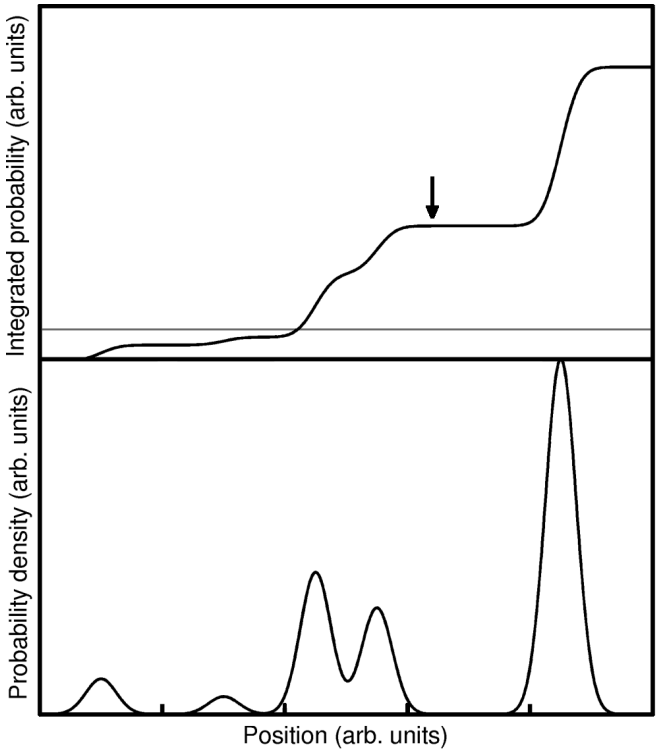

Figure 3.4: Illustration of algorithm for implementing absorbing boundary conditions in the lead of an AB ring, drawn in 1D for simplicity. The bottom panel shows the probability density as a function of position within the lead, and shows a series of separate packets. The top panel shows the integrated probability density; the flat regions in the top panel satisfy the condition for identifying a packet and the grey line marks the threshold value ϵ_2 (see main text for details). The algorithm will remove probability weight to the left of the position marked by the arrow.

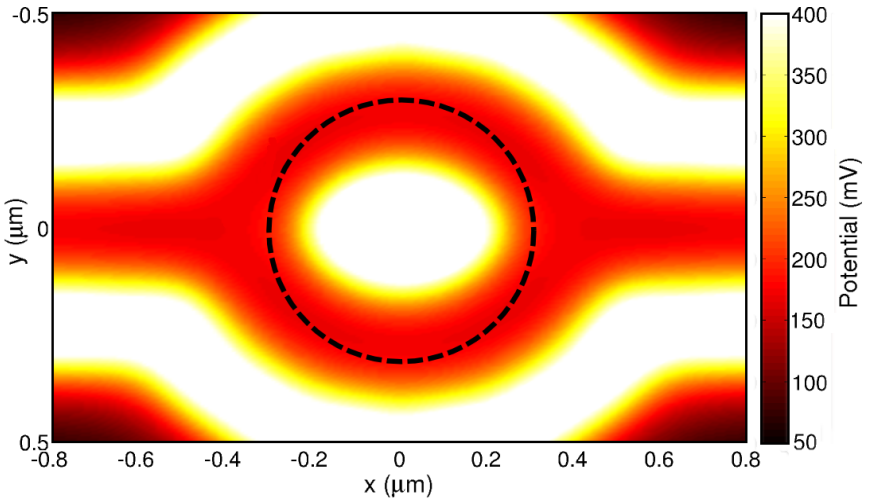

Figure 3.5: Central region of the potential used for AB ring device. The dashed circle has a radius of 311 nm, and so encloses a single magnetic flux quantum in a field of 13 mT.

3.5 Numerical results for AB ring

In this section the numerical techniques developed in the previous chapter will be used to simulate the transmission of an electron through an AB ring which is defined by a realistic pattern of surface gates. The potential due to the gates was calculated using the methods of Section (2.5.1) and the central part of the potential is plotted in Fig. (3.5). The figure does not show the full extent of the leads to either side of the ring; the length of leads used will depend upon whether or not absorbing boundary conditions are used. The lithographic width of the leads and arms in the gate design used is 100 nm, and the mean radius of the ring is approximately 310 nm. In typical experiments on AB rings in semiconductors there may be a high probability of reflection at the lead-ring interface. However, as the purpose of these simulations is to examine interference due to the AB effect, the gate voltages used are chosen to minimise the probability of reflection from the ring.

At the start of the simulation, the wavefunction is localised to the left lead. The wavefunction perpendicular to the leads is the numerically-determined ground state of the transverse potential, which is approximately Gaussian. The wave-

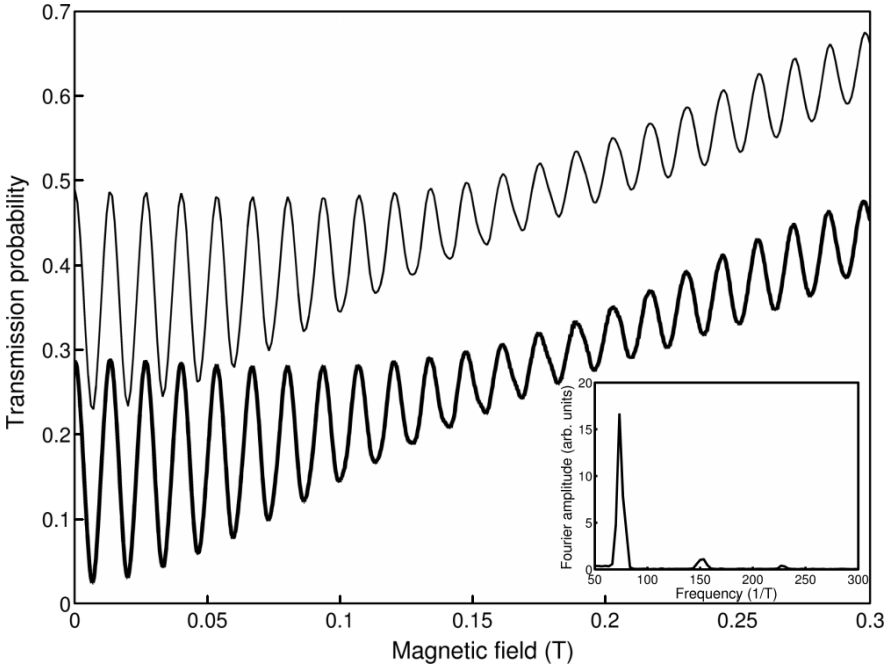

Figure 3.6: Transmission probability through an Aharonov-Bohm ring after 45 ps. Thin line: non-absorbing boundaries, offset by 0.2 for clarity. Thick line: absorbing boundary conditions. Inset: Fourier transform of the transmission probability. The peak at 73.5 T^{-1} *arises from a trajectory which encloses a single flux quantum in an area of* $3.05 \times 10^{-13} m^2$.

function parallel to the leads is chosen to also be Gaussian, with a width approximately equal to the transverse width. The wavefunction is then given an initial speed of 10^5 ms^{-1} (equivalent to an energy of 1.9 meV for an electron in GaAs) in the x direction. The transmission probability after 45 ps is found by integrating the probability density for $x > 1.2$ μm. Figure (3.6) firstly shows the transmission probability as a function of B without absorbing boundary conditions, with 5 μm-long leads. The figure also shows the transmission probability using the absorbing boundaries described in Section (3.4). The use of ABCs allows the computational domain to be greatly decreased in size, with leads which are 1.5 μm in length. The transmission probability calculated using ABCs is clearly in very good agreement with that calculated using non-absorbing boundary conditions (NABCs); the maximum difference in transmission probability between the two calculations in Fig. (3.6) is 0.009.

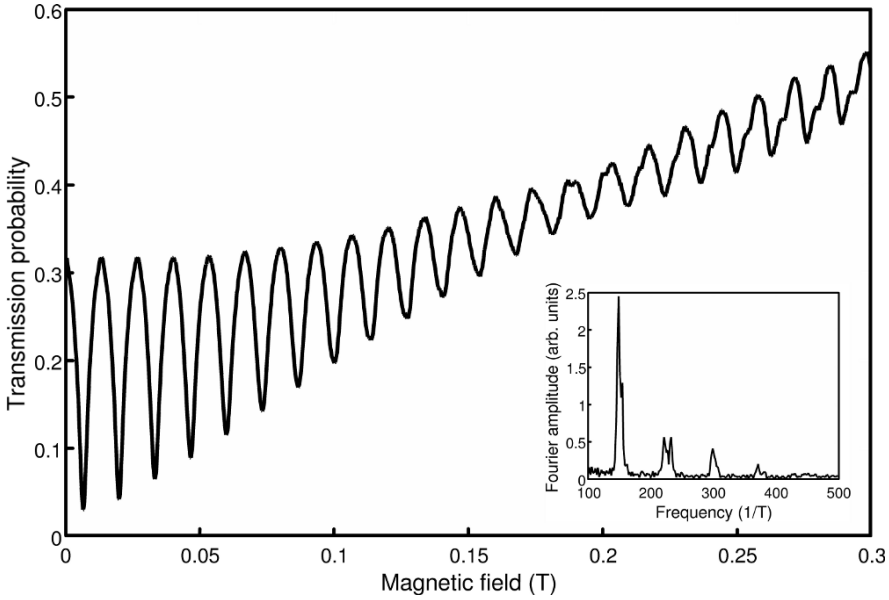

Figure 3.7: Transmission probability through an Aharonov-Bohm ring after 95 ps. Inset: Fourier transform, showing only the higher-order peaks. The peaks are at integer multiples of the fundamental frequency (73.5 T^{-1}*), corresponding to trajectories which encircle the ring from two to five times. The peak for the* h/e *oscillation is not shown.*

The Fourier transform of the transmission probability is shown in the inset to Fig. (3.6). The first peak corresponds to a period of 13.6 mT, which corresponds to enclosing one magnetic flux quantum in a ring of radius 311 nm, consistent with the lithographic dimensions of the simulated device. Smaller peaks at frequencies twice and three times this fundamental frequency are also visible, which arise from trajectories that perform more than one loop around the ring and so enclose multiple flux quanta.

Figure (3.7) then shows the transmission probability after 95 ps, calculated using ABCs. This calculation would have been impractical using NABCs as the leads would have needed to be significantly longer in order to avoid spurious effects from reflections from the edge of the computational domain. Increasing the simulation time allows trajectories which make multiple loops around the ring to occur, and so this corresponds qualitatively to an experiment with increased coherence time. Alternatively, multiple loops around the ring are more likely to occur experimentally if the ring has a smaller radius. For example, Hansen *et al.*

[74] and Wright [91] both measured AB oscillations in rings defined by an etch in similar GaAs heterostructures. The former used a ring with 490 nm radius and saw up to the $n = 6$ AB oscillation, whilst the latter used a radius of 2 μm and saw only the $n = 1$ and $n = 2$ oscillations.

The transmission probability in Fig. (3.7) exhibits some features which deviate from a simple sinusoidal oscillation. Firstly, there is a general trend for the AB oscillation amplitude to decrease with increasing magnetic field. A similar effect is also seen in the simulations of Szafran & Peeters [86, 87]. The decreasing amplitude can be attributed to the fact that as the field is increased, the Lorentz force increases the transmission amplitude from the entrance lead into one arm of the ring. The phase acquired along each path S_1, S_2 in Eq. (3.4) must then be weighted by the probability density for finding the electron in either arm. The Lorentz force also leads to an overall increase in the background transmission probability by decreasing the probability that the incoming electron reflects at the entrance to the ring, and above a magnetic field of approximately 0.15 T the transmission probability is greater than at zero magnetic field.

The transmission probability in Fig. (3.7) also shows another deviation from simple sinusoidal behaviour: higher-frequency components to the oscillation are clearly visible, as confirmed by the Fourier transform which shows peaks at up to five times the fundamental frequency of 73.5 T^{-1}. Some of the peaks in the Fourier transform are also split into two. Yau *et al.* [92] suggest that this structure in the Fourier transform can arise from the geometric phase acquired in the presence of a spin-orbit interaction, but the simulations presented here do not include spin-orbit effects.

Although Liu *et al.* [93] have attributed similar features to mixing between multiple transverse subbands in the arms of the rings, calculations by Tan & Inkson [94] showed that the experimental results of Ref. [93] were due to clockwise- and anticlockwise-travelling states having different orbital radii. The difference in frequencies seen in the Fourier transform of Fig. (3.7) leads to beating with an envelope period of 0.17 T, and beating with this period is visible in the transmission probability. The envelope period in the results of Tan & Inkson [94] was approximately 40 mT for a ring of radius 800 nm with arm width 300 nm. Although it is difficult to compare the results of Tan & Inkson [94] directly to this

work as they use an analytic form for the potential which does not closely match the one used here, we can use their result to make an approximate estimate of the shift in frequencies expected. For the potential used in these simulations the energy difference between the two lowest transverse subbands is $\hbar\omega \simeq 4$ meV. The mean radius of the ring was previously shown to be 311 nm, and using Eq. (9) of Ref. [94] the lowest-energy clockwise and anticlockwise states are expected to produce AB oscillations which differ in frequency by approximately 6%. The difference in the frequencies for the $h/2e$ oscillation is 4.0%, and for the $h/3e$ oscillation it is 5.4%. It is thus likely that the splitting seen here does indeed arise from the difference between clockwise and anticlockwise states.

3.6 Conclusions

In this chapter we used the numerical methods discussed earlier in this thesis to simulate the transmission of an electron wavepacket through an Aharonov-Bohm ring. We saw that an important advantage of the techniques used here is the ability to incorporate all of the effects that arise in a realistic geometry, including the reduction of the Aharonov-Bohm oscillation amplitude due to the Lorentz force preferentially injecting the wave packet into one arm of the ring. The simulations also demonstrate the emergence of the higher-order h/ne ($n > 1$) oscillations when the simulation time is increased to enable multiple loops around the AB ring to be made. Simulating this latter effect was made computationally tractable by developing a method to handle absorbing boundary conditions which is straightforward to implement. This enables the size of the computational domain to be significantly reduced (thereby greatly reducing the time needed to perform the simulation) without spurious effects arising due to reflection from the edge of the domain. Another advantage of the techniques used in this chapter is that they could be extended in a straightforward manner to simulate more complicated potentials – for example, an AB ring with quantum dots in the arms, or a ring with an added random background disorder potential. Kvon *et al.* [95] suggested that disorder could lead to the suppression of some of the higher-order peaks, and this could be tested with simulations similar to those performed here.

Time and tide wait for no man.

Proverb

4

Coherent electron oscillations in SAW devices

4.1 Introduction

This chapter is concerned with analysing single-electron coherent dynamics in a SAW device which consists of two parallel channels separated by a controllable tunnel barrier; such a device is a fundamental component of many SAW-based quantum information processing schemes. Numerical simulations will be used to investigate the effect of electric and magnetic fields upon the electron dynamics, and it will be seen that in both cases the electron oscillates between the two channels with a field-dependent frequency. A theoretical model will then be developed to explain the results from the simulations through an analytic calculation of the time evolution operator. A magnetic field will be incorporated into the model using an infinitesimal Aharonov-Bohm effect, and by Lorentz transforming into the rest frame of a SAW minimum the model can be extended to include both

a transverse electric field and a perpendicular magnetic field. Finally, it will be demonstrated that it is possible to rotate the state of the electron to any position on the Bloch sphere by applying a perpendicular magnetic field to a Mach-Zehnder geometry.

4.2 Description of SAW device

In this chapter we will study electron dynamics in the device depicted in Fig. (4.1), designed by Masaya Kataoka based upon the proposal in Ref. [40]. The device consists of two parallel SAW channels, each of which is connected to independent source and drain Ohmic contacts. The two channels gradually come together and meet at a narrow gate which defines a controllable tunnelling barrier. In the vicinity of the barrier the two gates labelled TC and BC in Fig. (4.1) can be used to control the electric potential in the two channels. After approximately 1 μm the channels then separate, and the current from each channel can be measured.

Understanding the charge dynamics in this device is of great importance for both the spin and charge qubit schemes discussed in Section (1.4.1). For charge qubits, this device could be used to perform a single qubit rotation. Alternatively, in a spin qubit scheme the frequency of a two-qubit rotation is determined by the energy $\gamma^2/4U$, where U is the on-site Coulomb energy and γ is the coupling energy between neighbouring SAW channels. In Section (4.4.1) it will be seen that γ also controls the frequency of a single-qubit rotation for a single charge qubit. An understanding of how to determine and control this coupling experimentally is therefore needed in order to design a two-qubit spin gate.

4.3 Numerical simulations

The method presented in Section (2.5.1) is used to solve the Laplace equation to find the potential which arises when voltages are applied to the gate design shown in Fig. (4.1). This will lead to a realistic potential because the voltages applied to the the surface gates in an experiment would be sufficiently negative to completely remove the 2D electron gas, so a self-consistent solution of the Poisson and Schrödinger equations is not necessary. The potential used will

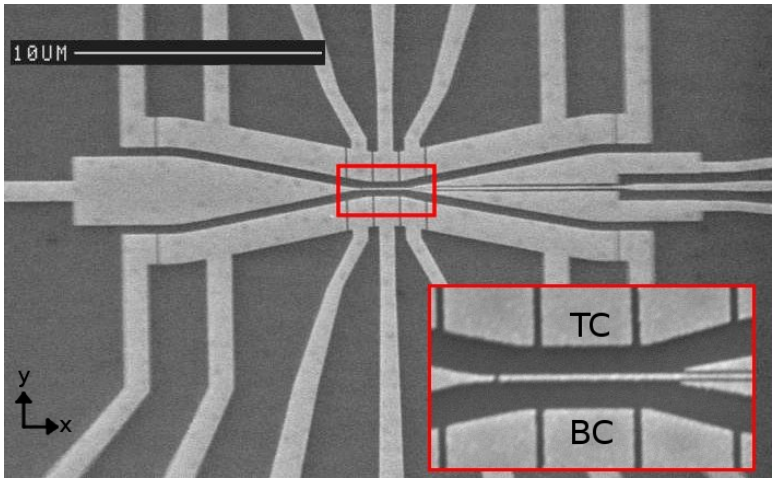

Figure 4.1: SEM image of a two-channel SAW device. A transducer (not shown) is located to the left of the device and generates SAWs which move from left to right. The gates labeled TC and BC are used to change the electric potential in each channel. The inset shows a close-up of the barrier region where the two channels meet and tunnelling between the two channels is possible.

always approximate a double-well potential (corresponding to the two channels), and throughout this chapter we assume a SAW amplitude of 20 mV [65].

At the start of the simulations, the electron is localised to one SAW minimum in the top-left entrance lead, away from the tunnel barrier which is centered at $y = 0$. The initial wavefunction is the numerically-determined ground state of this minimum, and the electron is then given a velocity equal to the velocity of the SAW-defined dynamic quantum dot. It should be noted that all of the simulations presented here are performed in the rest frame of the SAW, so the dot only has a non-zero velocity in the y direction due to the orientation of the channel. This initial state is then evolved for 0.85 ns; after this time the wavefunction has moved past the barrier region and into the exit leads. Figure (4.2) shows a typical result from such a simulation; the probability density at a series of different times is shown, and it is seen that the wavefunction oscillates between the two channels.

The voltages used for the simulation in Fig. (4.2) were chosen so that the potential in the top and bottom SAW channels is the same. An important quantity of interest is the probability $P_T(t)$ that the electron is to be found in the top

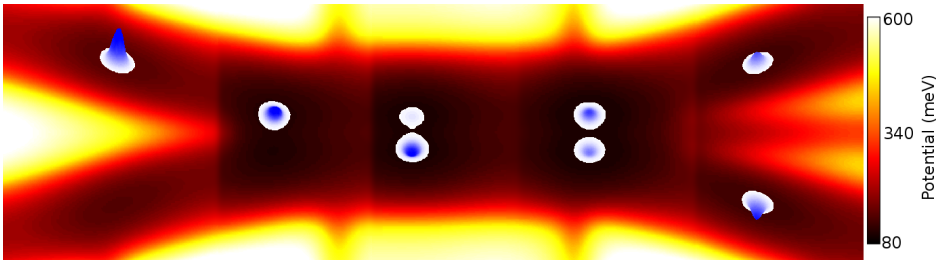

Figure 4.2: Typical result from simulation of two channel SAW device with a relatively high barrier between the channels. The electron probability density (in blue) is shown at five different times, and is seen to oscillate between the two channels.

SAW channel at time t, and at the end of the simulation P_T is the probability that the electron exits to the top-right lead. $P_T(t)$ is calculated by numerically integrating the probability density for $y > 0$, and is plotted in Fig. (4.3) for a typical calculation (note that different barrier heights are used in Figs. (4.2) and (4.3)). The probability of the electron occupying the top channel oscillates with time, and we now proceed to consider the effect of transverse electric and perpendicular magnetic fields on this oscillation.

4.3.1 Effect of electric field

An electric field is applied across the device by altering the voltages V_{TC} and V_{BC} applied to the TC and BC gates (see Fig. (4.1)). The difference in the voltages $\Delta V = V_{TC} - V_{BC}$ is applied symmetrically, so that $V_{TC} = V_0 + \Delta V/2$, $V_{BC} = V_0 - \Delta V/2$. Figure (4.4) shows how the probability of the electron exiting from the top-right lead varies as a function of ΔV and the barrier gate voltage V_B. For the gate voltages used in these simulations, the electron performs ~ 15 oscillations along the length of the barrier. Due to the time-consuming nature of these simulations only the case where $\Delta V > 0$ was investigated in detail, although some simulations were also performed with $\Delta V < 0$ which suggested that the results are symmetric in ΔV. Changing the gate voltages leads to a change in the frequency of the oscillation depicted in Fig. (4.3). As the time for which oscillation between the two channels can occur is fixed by the length

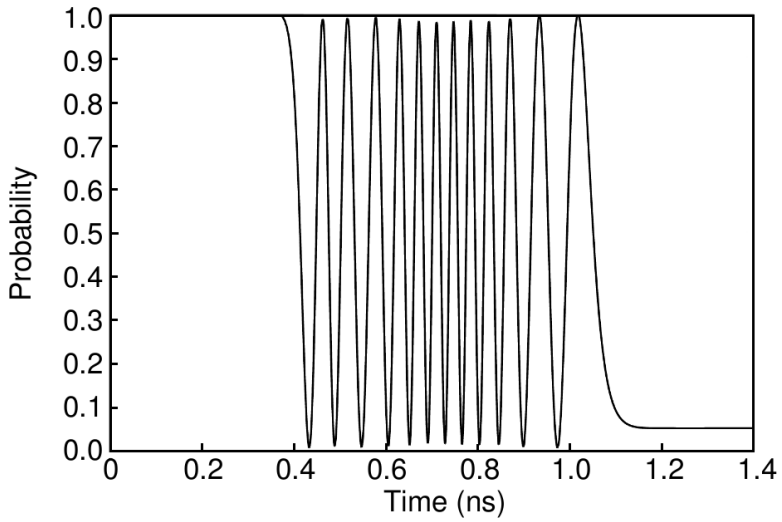

Figure 4.3: Probability of electron occupying the top SAW channel as a function of time with a relatively low barrier between the channels. The central ~ 0.6 *ns is the time for which the electron is able to tunnel at the barrier separating the channels.*

of the barrier, this then leads to the periodic oscillation in the final occupation probability seen in Fig. (4.4).

4.3.2 Effect of magnetic field

A magnetic field was then applied, with no electric field across the device ($\Delta V = 0$) and with V_B chosen so that the electron performs $\sim$ 1–3 oscillations between the channels as it is carried past the barrier. The results from these simulations are shown in Fig. (4.5). In a similar manner to Section (4.3.1), the electron oscillates between the two channels as a function of time, and the frequency of this oscillation depends upon the barrier gate voltage and magnetic field. Comparing Fig. (4.4) with Fig. (4.5), there is a qualitative similarity in the effect of ΔV and B upon the oscillations. In order to understand the origin of this similarity, a model that describes the oscillation process will now be developed.

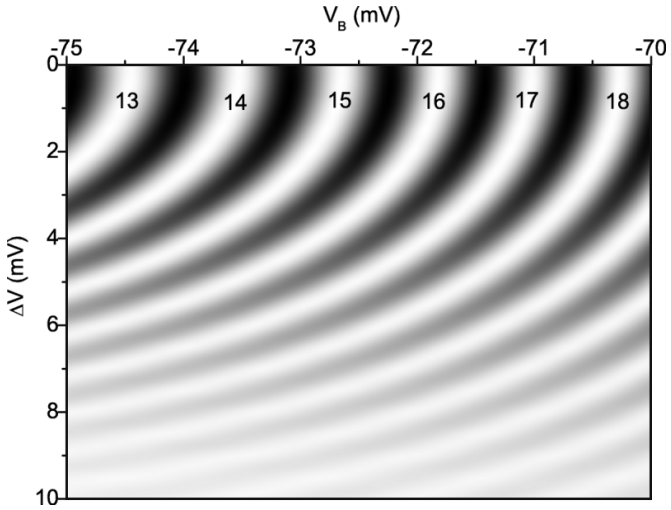

Figure 4.4: Results from numerical simulation of electron dynamics in an electric field, for an electron injected into the top channel. White (black) indicates that the electron exits from the top (bottom) channel. The number of oscillations performed as the electron travels along the barrier region is indicated on each of the white contours.

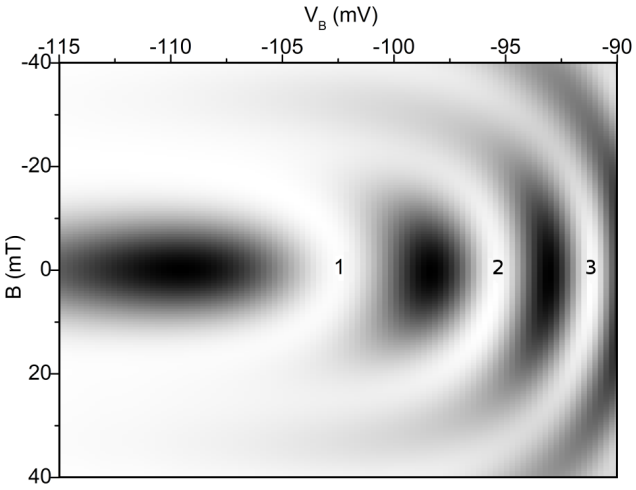

Figure 4.5: Results from numerical simulation of electron dynamics in a perpendicular magnetic field, for an electron injected into the top channel. White (black) indicates that the electron exits from the top (bottom) channel. The number of oscillations performed as the electron travels along the barrier region is indicated on each of the white contours.

4.4 Theoretical model

4.4.1 Electric field model

In order to determine the basis set to be used in developing a model, the wavefunction at each time step in the numerical simulations was decomposed into a linear combination of the instantaneous eigenstates $\psi_i(t)$. For all of the numerical simulations that were performed, the wavefunction can be well-represented by a superposition of the first two instantaneous eigenstates – writing $\psi(t) = \sum_i a_i \psi_i(t)$, it was found that $a_0^2 + a_1^2 > 0.99$. The coupled SAW channels can be viewed as a double-well potential: in the limit of an infinitely high barrier between the two wells the two lowest eigenstates are degenerate if the potential is symmetric, and the states are also localised to one channel or the other in this limit. These two localised states will be used as the basis in the model, and denoted as $|0\rangle$ and $|1\rangle$ for the state localised to the upper and lower channel respectively.

Without loss of generality the zero of energy is chosen so that the basis states have energy $\pm\epsilon/2$; $\epsilon = 0$ therefore corresponds to a symmetric potential, whilst setting $\epsilon \neq 0$ tips the potential towards one well or the other. This is equivalent to changing ΔV in the numerical simulations. The coupling between the two states is $\langle 1|H|0\rangle = \langle 0|H|1\rangle = -\gamma/2$. The Hamiltonian in the $\{|0\rangle, |1\rangle\}$ basis is therefore

$$H = \frac{1}{2}\begin{pmatrix} \epsilon & -\gamma \\ -\gamma & -\epsilon \end{pmatrix} \tag{4.1}$$

$$= \frac{1}{2}(\epsilon\sigma_z - \gamma\sigma_x) \tag{4.2}$$

The time evolution operator is then found by making use of Eq. (1.4) to exponentiate this Hamiltonian:

$$U(t) = \begin{pmatrix} c(t) - i\epsilon s(t)/\Delta & i\gamma s(t)/\Delta \\ i\gamma s(t)/\Delta & c(t) + i\epsilon s(t)/\Delta \end{pmatrix}$$

$$= c(t)\mathbb{I} + \frac{i\gamma s(t)}{\Delta}\sigma_x - \frac{i\epsilon s(t)}{\Delta}\sigma_z \tag{4.3}$$

where $\Delta^2 = \epsilon^2 + \gamma^2$, $c(t) = \cos(t\Delta/2\hbar)$ and $s(t) = \sin(t\Delta/2\hbar)$. By comparing Eq. (1.4) to Eq. (4.3), we see that this time evolution operator (TEO) corresponds to a rotation about the axis $\boldsymbol{n} \propto (-\gamma s(t)/\Delta, 0, \epsilon s(t)/\Delta)$ with the rotation angle ϕ satisfying $c(t) = \cos\frac{\phi}{2}$. The rotation angle after a time T is therefore

$$\phi = T\Delta/\hbar \tag{4.4}$$

Because the time evolution operator in Eq. (4.3) contains only σ_x and σ_z operators the rotation axis can be characterised by the angle χ between the rotation axis and the polar axis (i.e. the z-axis) of the Bloch sphere, and this angle is given by

$$\sin\chi = \frac{n_x}{|\boldsymbol{n}|} = -\gamma/\Delta \tag{4.5}$$

The time T for which the electron can tunnel through the barrier is taken to be 0.6 ns from Fig. (4.3). From Eq. (4.4) the electron oscillates between the states $|0\rangle$ and $|1\rangle$ at a frequency $\Delta/\hbar$, so the number of oscillations n is given by $2n\pi{=}T\Delta/\hbar$. For integer values of n the final state of the electron is $|0\rangle$, for half-integer values the final state is $|1\rangle$, and for other values the final state is some intermediary superposition.

This description assumes that tunnelling between the two channels is completely suppressed before the electron reaches the barrier region, and that γ is constant and large enough to allow tunnelling for the length of the barrier region. It would be straightforward to instead allow a smooth variation of γ along the barrier by considering a series of small time steps, each with a different $\gamma(t)$, and then numerically calculating the time-ordered product of the TEOs for each step. Some calculations were performed with a Gaussian variation of $\gamma(t)$ with time, but the results were not significantly different from using constant γ. The advantage of using a constant value for γ is that it enabled the simple analytic expressions given by Eqs. (4.4) and (4.5) to be derived, and this will allow a comparison to be made to the results with a magnetic field in the next section.

4.4.2 Magnetic field model

The model of electric dynamics in an electric field can be adapted to include the effect of a perpendicular magnetic field, and for simplicity we begin by setting $\epsilon = 0$, and so $\Delta = \gamma$. From Eq. (3.3), a particle with charge e moving in a magnetic field $(0, 0, B)$ acquires an Aharonov-Bohm phase

$$S = \exp\left(-i \int e\boldsymbol{A} \cdot \mathrm{d}\boldsymbol{x}/\hbar\right). \tag{4.6}$$

The magnetic vector potential is chosen to be $\boldsymbol{A} = (-By, 0, 0)$, and the centres of the two SAW channels are taken to be at $y = \pm a$, where $a = 80$ nm for the device geometry depicted in Fig. (4.1). The tunnelling region is split into a series of N small steps of length $dx = v(dt)$ where v is the SAW velocity, and in each step the two basis states will acquire different Aharonov-Bohm phases by virtue of their different y positions – the state $|0\rangle$ acquires the phase

$$S_0 = \exp\left(-ieBav(dt)/\hbar\right) \tag{4.7}$$

whilst the phase acquired by the state $|1\rangle$ is

$$S_1 = \exp\left(ieBav(dt)/\hbar\right) \tag{4.8}$$

This description can be thought of as representing the tunnelling region by a series of consecutive Aharonov-Bohm loops, each enclosing an infinitesimal flux $\delta\Phi$ as shown in Fig. (4.6).

The diagonal elements of the TEO (4.3) are therefore modified to arrive at the TEO for a single step dt,

$$U_B(dt) = \begin{pmatrix} c(dt)e^{-i\theta} & is(dt) \\ is(dt) & c(dt)e^{i\theta} \end{pmatrix} \tag{4.9}$$

$$= \mathbb{I}c(dt)\cos\theta + i\sigma_x s(dt) - i\sigma_z c(dt)\sin\theta \tag{4.10}$$

where $\theta = eBav(dt)/\hbar$ and $c(dt) = \cos(\gamma(dt)/2\hbar)$, $s(dt) = \sin(\gamma(dt)/2\hbar)$ (this is the same as the definition of the functions $c(t)$ and $s(t)$ introduced earlier, with

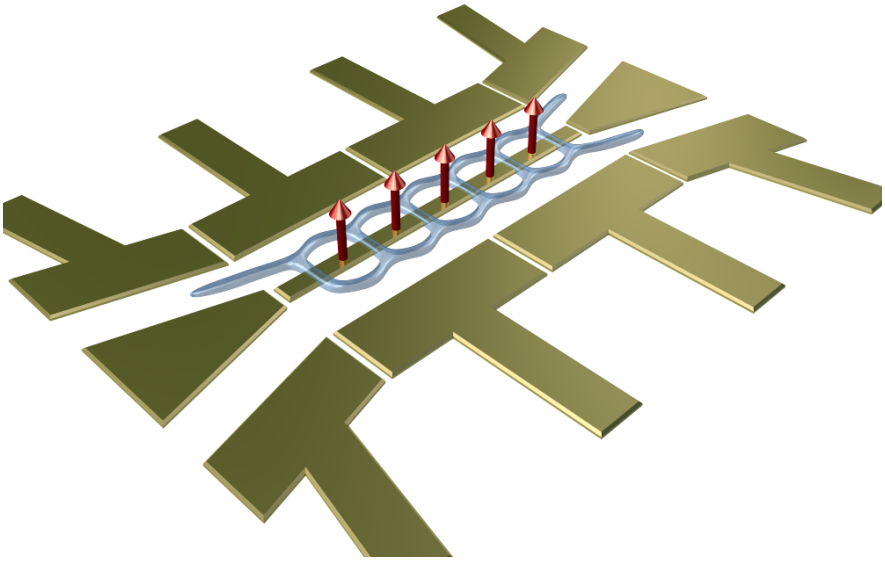

Figure 4.6: Diagram illustrating the model of the effect of a magnetic field in a two-channel SAW device. The electron trajectory (blue) forms a series of infinitesimal loops as it oscillates between the channels. Each loop therefore encloses a magnetic flux (red arrows) which changes the phase of the states in the two channels.

$\Delta = \gamma$). As in Section (4.4.1), the TEO is most easily thought of as a rotation on the Bloch sphere; from Eq. (1.4) the rotation angle ϕ satisfies $c(dt)\cos\theta = \cos(\phi/2)$ and the rotation axis is $\boldsymbol{n} \propto (-s(dt), 0, c(dt)\sin\theta)$.

The time evolution operator for the entire tunnelling region is then

$$U_B(T) = U_B(Ndt) = \lim_{dt\to 0} \prod^{N} U_B(dt) \tag{4.11}$$

Rather than evaluating this product directly, however, it is simpler to find expressions for the orientation of the rotation axis and the rotation angle in the limit $dt \to 0$. For the former, we will need to make use of the fact that

$$\lim_{x\to 0+} \frac{\sin x}{\sqrt{\sin^2 x + \cos^2 x \sin^2 \alpha x}} = \frac{1}{\sqrt{1+\alpha^2}}. \tag{4.12}$$

Letting $x = \gamma(dt)/2\hbar$ and $\alpha = 2eBav/\gamma$, the angle χ between the rotation axis and the polar axis of the Bloch sphere then satisfies

$$\sin\chi = \frac{1}{\sqrt{1+\alpha^2}} \tag{4.13}$$

To find the rotation angle, we note that

$$2\arccos(\cos x\cos(\alpha x)) \simeq 2x\sqrt{1+\alpha^2} \tag{4.14}$$

as $x \to 0$, which follows from a Taylor expansion. The total rotation angle is then

$$\phi_{tot} = N\phi = \frac{\gamma T\sqrt{1+\alpha^2}}{\hbar} \tag{4.15}$$

because there are N rotations through the small angle ϕ and $T = N(dt)$.

Figures (4.7) and (4.8) illustrate the rotation described by Eqs. (4.13) and (4.15). They show the evolution of the wavefunction on the Bloch sphere as a function of time for two different rotation angles ϕ_{tot}. Figure (4.7a) and (4.8a) show the $B = 0$ case. From Eq. (4.13), the angle between the polar axis and the rotation axis is $\pi/2$ when $B = 0$ – i.e., the Bloch vector rotates around the x axis. As the magnetic field is then increased in parts (b-d) of the two figures, the rotation axis tilts towards the z axis.

From Eqs. (4.13) and (4.15), it is straightforward to calculate the final state of the electron for a given set of device parameters. The parameter n_0 is used to define the coupling between the two channels; n_0 is defined to be the number of oscillations performed at $B = 0$, $\epsilon = 0$ (thus $2n_0\pi = \gamma T/\hbar$ from the definition of n in Section (4.4.1) and making use of the fact that $\Delta = \gamma$ when $\epsilon = 0$). With the wavefunction initialised in the top channel, Fig. (4.9) shows the probability that the electron is in the top channel after the time T as a function of B and n_0.

The crescent-like features in Fig. (4.9) can be understood by considering the condition required for the rotation angle to be $\phi_{tot} = 2m\pi$ for integer m, which corresponds to the final state being $|0\rangle$. From Eq. (4.15) this occurs when $2m\pi = 2n_0\pi\sqrt{1+\alpha^2}$, which for successive values of m leads to the white crescent-shaped features of Fig. (4.9) given that $\alpha \propto B$.

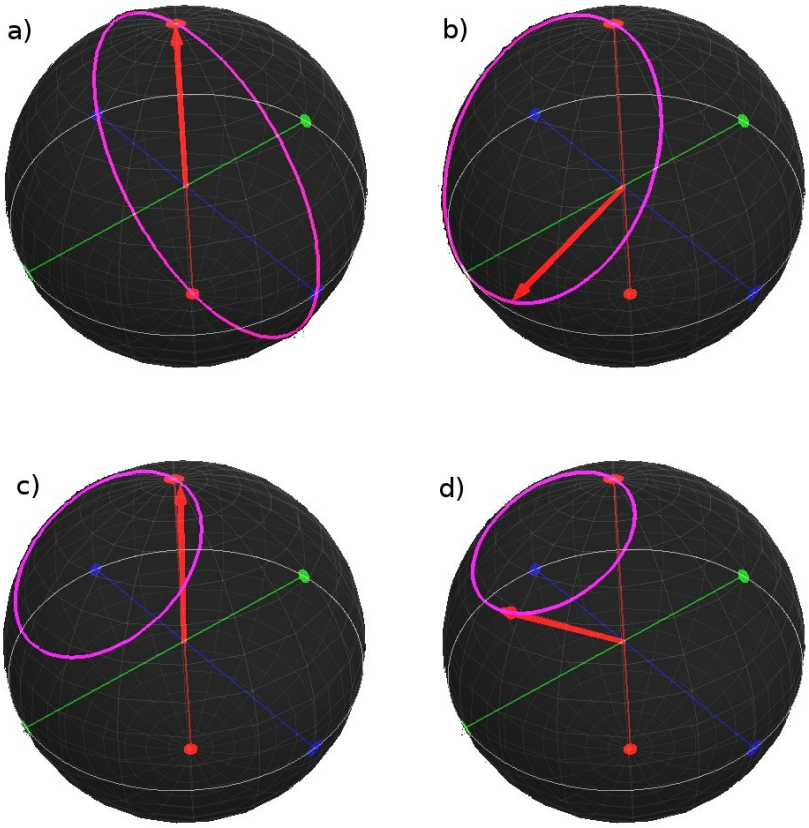

Figure 4.7: Bloch sphere representation of oscillation between parallel channels ($\phi_{tot} = 2\pi$). The pink circle illustrates the trajectory on the Bloch sphere and the red arrow indicates the final state. a) 0 mT, b) 16 mT, c) 28 mT, d) 36 mT.

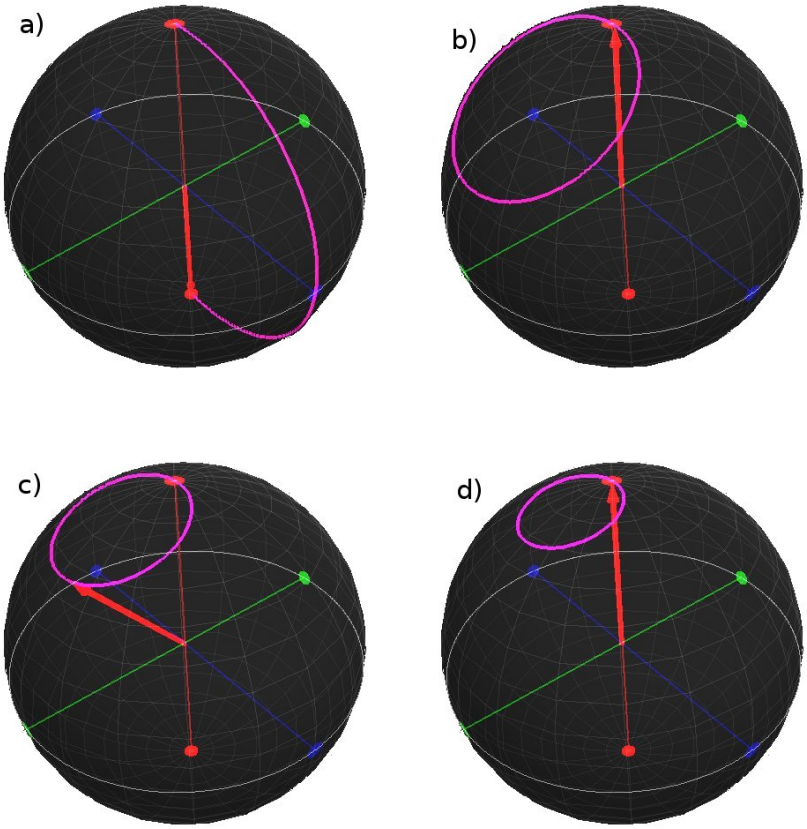

Figure 4.8: Bloch sphere representation of oscillation between parallel channels ($\phi_{tot} = \pi$). The pink circle illustrates the trajectory on the Bloch sphere and the red arrow indicates the final state. a) 0 mT, b) 14 mT, c) 22 mT, d) 31 mT.

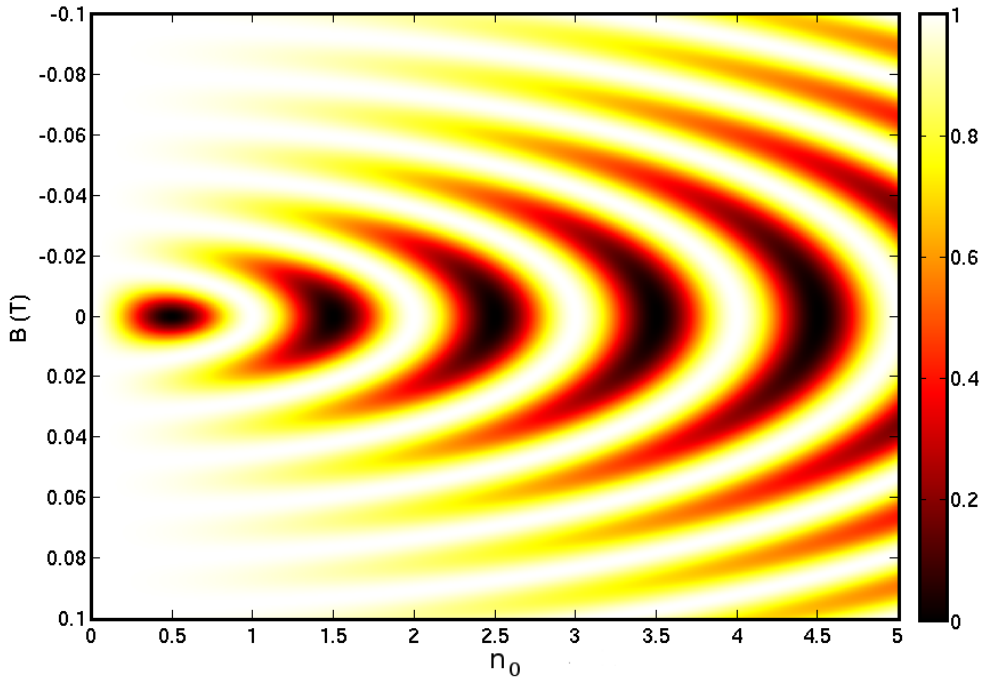

Figure 4.9: Results from analytic model of electron dynamics in a magnetic field. The electron is initially in the state $|0\rangle$; the colour scale shows the probability that the final state is then $|0\rangle$. The tunnel coupling is set by n_0, the number of oscillations performed at zero magnetic field.

We finally remark that there is very good agreement between the results from the numerical simulations in Fig. (4.5) and the results from the model in Fig. (4.9). There is an approximately exponential scaling between the barrier gate voltage in Fig. (4.5) and the tunnel coupling in Fig. (4.9): as the barrier gate is made more negative, tunnelling is expected to be exponentially suppressed.

4.4.3 Equivalence of models via Lorentz transform

As was discussed briefly in Section (4.3.2) and can be seen from a comparison of Figs. (4.4) and (4.5), the magnetic field B and the electric field provided by the gate voltage difference ΔV had similar effects upon the simulation results. The theoretical model developed in this chapter allows the reason for this to be understood by Lorentz transforming from the laboratory frame S to the rest-frame S' of the SAW. The Aharonov-Bohm phases introduced into the operator (4.9) vanish in S': there is no motion in the x direction and so $\boldsymbol{A} \cdot \mathrm{d}\boldsymbol{x} = 0$. However, the electric potential V' in frame S' is modified from the electric potential in V due to the non-zero magnetic vector potential: $V' = \gamma_v V - e\gamma_v v A_x$ where $\gamma_v = (1 - v^2/c^2)^{-1/2}$. The Lorentz transformation also changes the element of proper time: $dt' = dt/\gamma_v$. This leads to the result that a magnetic field B in frame S is equivalent to setting $\epsilon = 2veBa$ in frame S' (the factor of 2 arises because the energies of the two states were defined to be $\pm\epsilon/2$). Indeed, it can be verified that Eqs. (4.5) and (4.4) are the same as Eqs. (4.13) and (4.15) upon substituting this value for ϵ.

Given the manifestly covariant nature of the quantum mechanical phase acquired in the presence of an electromagnetic 4-potential it is perhaps not surprising that this equivalence between electric and magnetic fields should exist. The Lorentz transformation of the electromagnetic 4-potential underlies the form of the classical expression for the Lorentz force, so the models developed in this chapter illustrate an interesting connection between the infinitesimal Aharonov-Bohm phase and the Lorentz force [96]. It is also possible to use this observation to determine the effect of applying both a magnetic and electric field – Section (4.4.1) considered the situation where $B = 0$, $\epsilon \neq 0$ whilst Section (4.4.2) considered

$B \neq 0$, $\epsilon = 0$. In order to generalise the model to allow both $B \neq 0$ and $\epsilon \neq 0$, one needs only to replace ϵ by $\epsilon + 2veBa$ in the results derived in Section (4.4.1).

4.5 Single-qubit rotations

In quantum optics, the Mach-Zehnder interferometer (MZI) is a prototypical single-particle interference device [97]. The MZI consists of two beamsplitters and is illustrated in Fig. (4.10). Although the original interferometer used beams of photons, solid state devices operating in the Quantum Hall regime have been fabricated and measured [98, 99] and thus constitute electronic analogs of the original MZI. Rodriquez *et al.* [100] proposed that a SAW device could also be used as an electronic MZI, using a gate design similar to that shown in Fig. (4.11). The barriers labeled 1 and 3 in Fig. (4.11) each operate in a similar manner to the single barrier in Fig. (4.1), and are equivalent to optical beamsplitters in the optical MZI. The model discussed in Section (4.4) can therefore be used to completely describe the dynamics of an electron in this device by allowing the coupling γ to vary with time and then calculating the time-ordered product of a series of TEOs each having the form of Eq. (4.3).

As was shown in Section (4.4.3), applying a perpendicular magnetic field is equivalent to changing ϵ. Therefore, in a magnetic field the time evolution at a weak barrier (regions 1 and 3 of Fig. (4.11)) will be some combination of σ_x and σ_z rotations, as described by Eq. (4.3). When the barrier is large, the channels are decoupled so $\gamma = 0$ (region 2 of Fig. (4.11)). The evolution will then be only a σ_z rotation because from Eq. (4.5) the rotation axis will be aligned with the z axis of the Bloch sphere. As an example, the three barrier regions are taken to all have length 0.135 μm and the value of n_0, which defines the coupling strength, is set to 0.5, 0 and 1 respectively for the three barrier regions. The strength of the perpendicular magnetic field was 50 mT, so setting n_0 to 0.5 no longer gives a $\pi/2$ rotation (and similarly $n_0 = 1$ is no longer a π rotation). These parameters are comparable to those used earlier for the single-barrier device. Figure (4.12) shows the evolution of the Bloch vector with time and illustrates that the three regions correspond to either a combined σ_x and σ_z rotation or a pure σ_z rotation. With a fixed external magnetic field, it is therefore possible to rotate a single

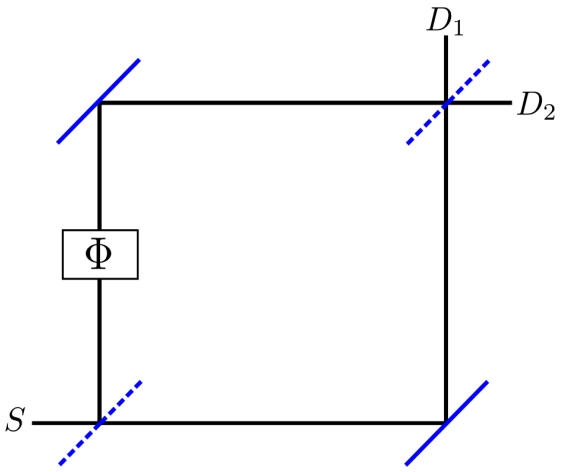

Figure 4.10: Mach-Zehnder interferometer. Particles are injected from the source S and encounter beam splitters (blue dashed lines) and mirrors (blue solid lines). One arm of the interferometer is subject to a phase change Φ which leads to interference patterns at the detectors D_1 and D_2.

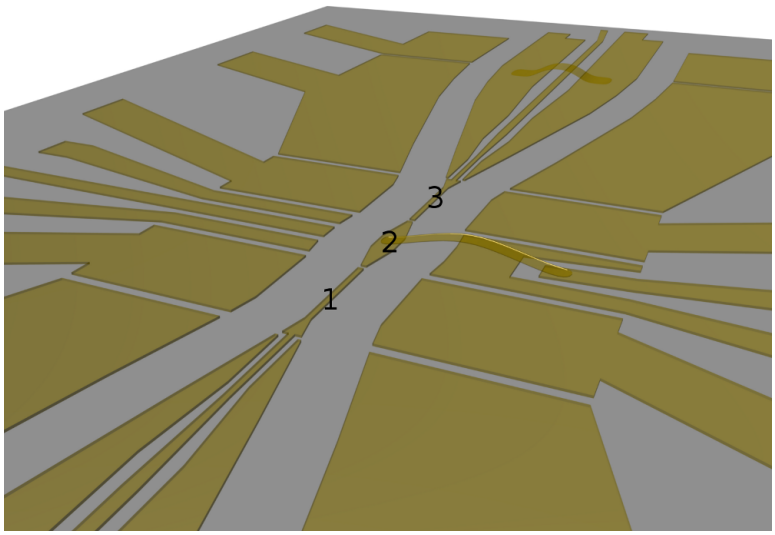

Figure 4.11: Proposed gate design for a SAW Mach-Zehnder interferometer (courtesy of M. Kataoka). Two parallel channels are separated by a series of controllable barriers. Barriers 1 and 3 couple the two channels together, whilst barrier 2 (contacted via an air bridge) is large and decouples the channels.

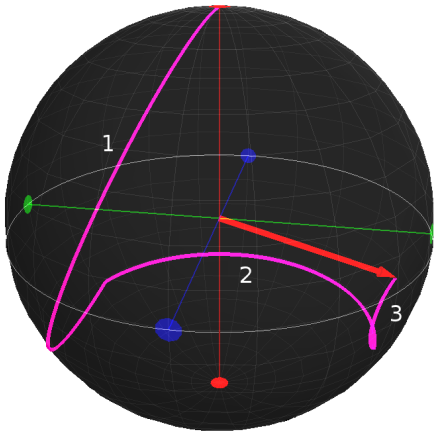

Figure 4.12: Evolution of the Bloch vector for a SAW MZI; see text for device parameters. The labels 1-3 refer to the three different regions marked in Fig. (4.11). The time evolution is shown by the pink trajectory and the red arrow indicates the final state.

qubit to any point on the Bloch sphere by controlling the tunnel couplings with the applied gate voltages.

4.6 Conclusions

In this chapter, the results from detailed numerical simulations of electron dynamics in a two-channel SAW device were presented. The potential used in the simulations was calculated from a realistic gate design using the method from Section (2.5.1), and a narrow barrier gate was used to control the coupling between the two channels. The simulations showed that the electron oscillates coherently between the two channels, and the frequency of this oscillation depends upon the voltages applied to the gates around the tunnelling region (which created a transverse electric field) and also upon the strength of a perpendicular magnetic field. The behaviour in an electric field was modelled analytically using a two-level Hamiltonian, and the model was extended to include the effect of a magnetic field via an infinitesimal Aharonov-Bohm effect. Using this model, it was shown that using gates to define a Mach-Zehnder-like geometry in combination with a magnetic field enables the state to be rotated to any position on the Bloch sphere.

Let your rapidity be that of the wind, your compactness that of the forest.

Sun Tzu

5

Coherent and squeezed states

5.1 Introduction

In this chapter we will discuss the dynamics of Gaussian wavefunctions in a harmonic potential. The ground state of the harmonic potential $V = \frac{1}{2}m\omega^2 x^2$ is a Gaussian centered at $x = 0$ with wavefunction $\psi_0(x) = A\exp(-m\omega x^2/2\hbar)$ (where A is a normalisation constant). We will consider two classes of excited states: those which are displaced from $x = 0$, and those with a standard deviation not equal to that of the ground state. These two types of state are known respectively as coherent and squeezed states; although coherent and squeezed photonic states have been the subject of much study in quantum optics, their electronic counterparts have received comparatively little attention.

The chapter will begin with a discussion of the mathematical properties of coherent and squeezed states. A number of applications in quantum information processing have been suggested for the photonic states, and similar applications may exist for electronic states. It is also of great importance to consider how

these states might be generated in a SAW device, both intentionally and unintentionally. It is often assumed, both in this thesis and in other work, that an electron is in a well-prepared state prior to performing some series of coherent manipulations. In practice, electrons in solid state devices are subject to uncontrollable perturbations due to interactions with the environment. Although it is difficult to completely characterise such perturbations, their effects will include changing the width or position of 1D channels. Understanding the effect of such perturbations is thus crucial for any study of electron manipulation in SAW devices, and it will be seen that examining coherent and squeezed states leads to a useful framework for interpreting the effects of these perturbations. Numerical simulations will then be used to investigate the factors affecting the controllable generation of coherent states using electrons carried in a SAW; it will be seen that the SAW amplitude is a crucial factor in this. We will finish by determining the effect that using coherent and squeezed states has upon the coherent oscillations in a two-channel SAW device discussed in the previous chapter.

♦

Before describing the dynamics of a general Gaussian wavefunction in a harmonic potential, we begin by introducing a mathematical tool which will be of use in the later discussion: the Wigner distribution.

5.2 Wigner distribution

The Wigner distribution for a wavefunction $\psi(x)$ is defined as [101]

$$f_w(p,q) = \frac{1}{2\pi\hbar}\int_{-\infty}^{\infty} e^{ips/\hbar}\left\langle q-\frac{s}{2}\middle|\psi\right\rangle\left\langle\psi\middle|q+\frac{s}{2}\right\rangle ds \tag{5.1}$$

where q and p are conjugate variables – q is a position co-ordinate and p is the momentum conjugate to that co-ordinate. If the q or p dependence is integrated

out of f_w, one finds

$$\int_{-\infty}^{\infty} f_w(p,q)dp = |\psi(q)|^2 \tag{5.2}$$

$$\int_{-\infty}^{\infty} f_w(p,q)dq = |\psi(p)|^2 \tag{5.3}$$

which are the co-ordinate and momentum probability distributions respectively. This motivates the interpretation of f_w as a quasiprobability distribution in phase space, although f_w can be negative so it can not be strictly interpreted as a probability distribution. The Wigner distribution for a quantum particle is the analogue of the phase-space trajectory of a classical particle, and it will be used in the description of Gaussian states in the remainder of this chapter.

5.3 Gaussian in a harmonic potential

In general, it is not possible to analytically determine the quantum-mechanical time evolution of an arbitrary state in an arbitrary potential. However, the evolution of a Gaussian wavefunction in a harmonic potential is amenable to a straightforward theoretical analysis. A general Gaussian wavefunction can be written

$$\psi(x,t) = N \exp\left(-\beta(t)(x - x_0(t))^2 + \frac{i}{\hbar}p_0(t)(x - x_0(t)) + \frac{i}{\hbar}\gamma(t)\right) \tag{5.4}$$

where N is a normalisation constant, $x_0(t)$ and $p_0(t)$ are time-dependent quantities which give the mean position and momentum of the wavefunction, γ is a phase factor and $\beta(t)$ is related to the standard deviation σ of the Gaussian ($\beta = 1/2\sigma^2$). It can be shown [101] that for the harmonic potential $V(x) = \frac{1}{2}m\omega^2x^2$, these quantities satisfy

$$x_0(t) = x_0(0)\cos(\omega t) + \frac{p_0(0)}{m\omega}\sin(\omega t) \tag{5.5}$$

$$p_0(t) = p_0(0)\cos(\omega t) - m\omega x_0(0)\sin(\omega t) \tag{5.6}$$

$$\beta(t) = a\frac{\beta(0)\cos(\omega t) + ia\sin(\omega t)}{i\beta(0)\sin(\omega t) + a\cos(\omega t)} \tag{5.7}$$

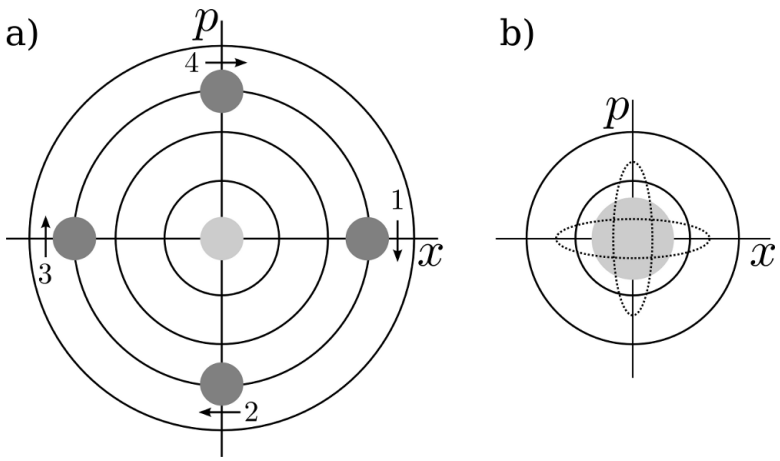

Figure 5.1: Wigner distributions for coherent and squeezed states. The black circular contours indicate classical trajectories of different energies, and the light grey circle shows the Wigner distribution of the ground state. a) Wigner distribution for a coherent state (dark grey circles) for a state with an initial x displacement at four times. b) Wigner distribution for a squeezed state (dashed ellipses). The state oscillates between the two ellipses, and so the width of the x projection oscillates between being greater than and less than the ground state.

where $a = m\omega/2\hbar$. (The evolution of the time-dependent phase $\gamma(t)$ is unimportant for the purposes of the current discussion.) From Eq. (5.7) it is clear that if $\beta(0) = a$ (corresponding to a standard deviation equal to that of the ground state) then $\beta(t) = a$ for all t. If either of x_0 or p_0 is non-zero, the mean position and momentum of the wavefunction then oscillate sinusoidally with time, in close analogy to a classical particle in a harmonic potential. The Wigner distribution of a state with non-zero $x_0(0)$ and $p_0(0) = 0$, $\beta(0) = a$ is plotted in Fig. (5.1a). A state such as this is known as a coherent state.

Alternatively, if $x_0(0) = p_0(0) = 0$ but $\beta(0) \neq a$ then the average position and momentum of the state remain zero for all time, but the width of the state oscillates as a function of time. From Eq. (5.7), it is possible to show that the standard deviation oscillates periodically between two values σ_{min} and σ_{max} such that $\sigma_{max}/\sigma_{min} = \beta(0)/a$. The Wigner distribution for such a state is shown in Fig. (5.1b); the two dashed ellipses in the figure are known as quadrature-squeezed states and have reduced uncertainty in one of p or q.

5.4 Coherent and squeezed states

Coherent states

Coherent states were first investigated by Schrödinger [102] in an attempt to find a quantum system which exhibited essentially classical behaviour. We saw in Section (5.3) that displacing a Gaussian wavefunction from the centre of a harmonic potential leads to a trajectory for the mean position which is the same as that for a classical particle; this is a manifestation of Ehrenfest's theorem [103]. None the less, coherent states remain quantum mechanical in nature, and Glauber [104] showed how to describe them in terms of quantum mechanical operators. Coherent states can be generated by applying the displacement operator $D(\alpha)$ to the vacuum state $|0\rangle$. The displacement operator is defined as

$$D(\alpha) = \exp\left(\alpha a^\dagger - \alpha^* a\right) \tag{5.8}$$

where α is a complex number which sets the magnitude of the displacement, $a^\dagger, a$ are the creation and annihilation operators and $a|0\rangle = 0$. The coherent state $|\alpha\rangle$ is then defined as $|\alpha\rangle = D(\alpha)|0\rangle$. Coherent states are also eigenstates of a, and have been the subject of much study in optics because they well describe the light created by a laser above threshold [105] (this is when the output is dominated by stimulated rather than spontaneous emission). The overlap between two different coherent states is [106]

$$\langle\alpha'|\alpha\rangle = \exp(-|\alpha - \alpha'|^2) \tag{5.9}$$

Thus, although different coherent states are not strictly orthogonal, for sufficiently large $\alpha - \alpha'$ the two states are effectively orthogonal. Consequently, Ralph *et al.* [107] have suggested using a pair of coherent states $|\pm\alpha\rangle$ with $\alpha \geq 2$ as a qubit. More recently, Lund *et al.* [108] have suggested that with suitable error correction, states with $\alpha = \pm 1.2$ have a sufficiently small overlap to be useful in quantum computation. A coherent state can be written as a superposition of the

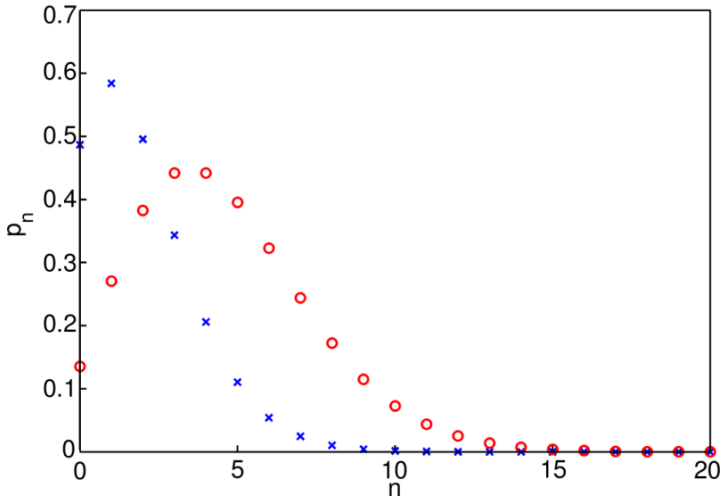

Figure 5.2: Overlap $p_n = \langle n|\alpha\rangle$ (from Eq. (5.10)) between a coherent state and the eigenstates of the harmonic oscillator, for $\alpha = 1.2$ (blue crosses) and $\alpha = 2$ (red circles).

eigenstates $|n\rangle$ of a harmonic oscillator:

$$|\alpha\rangle = \sum_{n=0}^{\infty} \alpha^n \frac{e^{-|\alpha|^2/2}}{\sqrt{n!}} |n\rangle \tag{5.10}$$

The value of α is related to the distance by which the wavefunction is displaced from the origin: the co-ordinate representation of a coherent state is [101]

$$\langle x|\alpha\rangle = N \exp\left(\frac{-m\omega}{2\hbar}\left[x - \sqrt{\frac{2\hbar}{m\omega}}\alpha\right]^2\right) \tag{5.11}$$

where N is a normalisation constant. Using $\hbar\omega = 2$ meV as a representative energy spacing in SAW devices, the centre of the state is therefore displaced by 34α nm so $\alpha = 2$ and $\alpha = 1.2$ correspond to displacements of 68 and 41 nm respectively. A displacement of this magnitude should therefore be achievable in practice, and Figure (5.2) shows the coefficients $p_n = \langle n|\alpha\rangle$ for these two values of α.

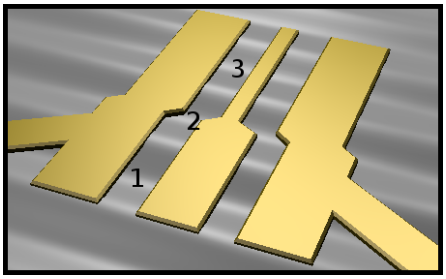

Figure 5.3: Schematic gate design for generating a coherent state. 1) The electron is initially in a 1D channel. 2) The channel shifts suddenly to one side, leaving the electron displaced from the centre of the channel. 3) The electron oscillates from side to side. (Two such channels are depicted)

Electronic coherent states could be generated in SAW devices using a gate design similar to that shown in Fig. (5.3). The electron is initially confined in a SAW minimum travelling along a Q1DC, and the channel then shifts to one side. If this shift is gradual then the electron will adiabatically follow the changing potential [9] and remain in an instantaneous eigenstate. However, if there is a sudden change in potential the electron will be displaced to one side of the channel and then oscillate from side to side. Exactly what is meant by a "sudden" change in the potential will be examined carefully in Chapter 6, where we will discuss experimental evidence demonstrating that the nonadiabatic excitation of an electron in a SAW device is feasible.

Squeezed states

Squeezed states can be created by applying the squeezing operator $S(\zeta)$ to the vacuum state, where

$$S(\zeta) = \exp\left(\frac{1}{2}(\zeta^* a^2 - \zeta(a^\dagger)^2)\right) \tag{5.12}$$

ζ is generally referred to as the squeezing parameter, and a squeezed state is written as $|\zeta\rangle = S(\zeta)|0\rangle$. In contrast to Eq. (5.8) which was an exponent of a linear function of the ladder operators, Eq. (5.12) involves the exponent of a quadratic function of the ladder operators. Because of this, squeezed light

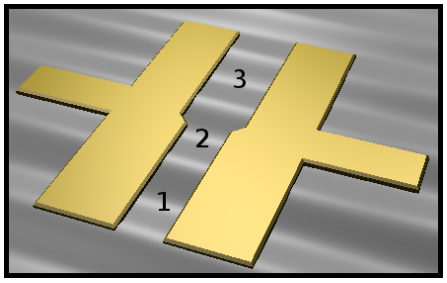

Figure 5.4: Schematic gate design for generating a squeezed state. 1) The electron is initially in a channel with subband spacing $\hbar\omega_1$. 2) The channel suddenly changes in width. 3) The standard deviation of the transverse wavefunction no longer matches that of the instantaneous ground state, so the wavefunction is now squeezed.

states are experimentally difficult to produce as non-linear optical interactions are required [109]. In contrast to the optical case, creating a squeezed electron wavefunction in a SAW device requires only that the width of the SAW channel vary with position: if the electron is initially in the ground state of a SAW minimum in a channel with confinement energy $\hbar\omega_1$ which then suddenly changes to $\hbar\omega_2$, the electron wavefunction will be squeezed. A schematic gate design for performing this process is shown in Fig. (5.4).

The co-ordinate representation of squeezed states was found by Rai & Mehta [110] to be

$$\langle x|\zeta\rangle = \frac{N}{\sqrt{1-2\theta}} \exp\left(-\frac{m\omega}{2\hbar}\frac{2\theta+1}{2\theta-1}x^2\right) \tag{5.13}$$

where

$$\theta = \frac{\zeta^* \tanh(2|\zeta|)}{2|\zeta|} \tag{5.14}$$

The overlap between two different squeezed states (i.e., between two Gaussians with standard deviations σ_1 and σ_2) is

$$\int_{-\infty}^{\infty} \psi_1^* \psi_2 dx = \sqrt{\frac{2\sigma_1\sigma_2}{\sigma_1^2+\sigma_2^2}} \simeq \sqrt{\frac{2\sigma_2}{\sigma_1}} \tag{5.15}$$

where the approximation holds when $\sigma_1^2 \gg \sigma_2^2$. Following the discussion in Section (5.3), taking σ_1 and σ_2 to be the extremal standard deviations of a squeezed

Gaussian wavefunction gives an overlap of $\sqrt{2\beta(0)/a}$. The two extremal states between which a squeezed Gaussian oscillates with time can thus be made approximately orthogonal for suitable $\beta(0)$, and Gottesman *et al.* [111] therefore suggested (in the context of quantum optics) that these states could be used as a qubit. To achieve an overlap of 1%, for example, requires that $\beta(0) = (5\times10^{-5})a$. For a typical ground state of an electron in a SAW device, the standard deviation is $\sigma \simeq 100$ nm and so this choice of $\beta(0)$ requires an initial standard deviation of 0.7 nm, which is unattainable for the devices considered in this work.

There are uses of squeezed states which do not require the states to be as strongly squeezed as this, however. There is a wide range of applications for squeezed light, many of which make use of the fact that the fluctuations in the amplitude or phase of the electromagnetic field can be reduced. Caves [112] proposed that squeezed light could be used to aid in the detection of gravity waves, and this idea was further developed by Pace *et al.* [113]. Xiao *et al.* [114] later demonstrated that squeezed light could be used to enhance the signal-to-noise ratio of interference fringes in a Mach-Zehnder interferometer. It has also been suggested that squeezed light could be a useful resource for the teleportation of coherent states [115]. There has been little study of how to generate squeezed electronic states, but it is possible they may prove to be a useful resource for performing experiments analogous to those performed with squeezed light. Aside from their potential applications, it is also important to understand under what conditions squeezed electronic states are generated as the undesired squeezing of an electronic state presents a potential source of error for other QIP schemes based on electron dynamics.

5.5 Practical generation of coherent states

Figure (5.3) illustrated the essential principle behind using a SAW device to generate a coherent state: the electron must travel along a 1D channel which suddenly shifts sideways without a significant change in confinement energy (as this might also lead to squeezing). If the shift in potential is slow, the electron adiabatically follows the potential and will remain in an instantaneous eigenstate. It will now be shown that it is therefore also necessary to consider the amplitude

of the SAW potential, as this affects the abruptness of the change in potential experienced by the electron. Throughout this section the co-ordinate system used is defined so that the SAW travels along the x axis. The direction of SAW travel will also be referred to as the *longitudinal* direction, and the *transverse* direction is perpendicular to this.

When an electron is carried along a gate-defined channel by a SAW, it will in general experience a time-varying electric field parallel to the direction of SAW motion which depends upon the pattern of the gates and the voltages applied to them. The dynamics of the electron then change depending upon the magnitude of this electric field relative to the electric field created by the SAW. There are three regimes of interest, depicted in Fig. (5.5). If the channel is approximately flat, so the longitudinal electric field from the gates can be neglected, the electron simply moves along the channel at the SAW velocity. If there is a large positive electric field (an "uphill" potential), the velocity of the electron is decreased relative to the SAW velocity, whilst if there is a large negative electric field (a "downhill" potential) the velocity of the electron is increased. This can be seen in Fig. (5.6), which plots the average electron position (determined from numerical simulations) for the three cases. We ignore the possibility that the electric field is large enough to overcome the SAW confinement, as this lies outside the regime in which SAW devices are typically operated.

If the longitudinal channel potential is flat, it is difficult to generate a sudden change in the transverse potential experienced by the electron. The characteristic minimum length scale of features that can be created in the potential at the 2DEG using surface gates is approximately equal to the depth of the 2DEG which is 90 nm in this work – this length scale corresponds to a time of $\sim$ 30 ps at the SAW velocity. However, Fig. (5.6) shows that when the longitudinal potential is not flat the electron velocity can become greater than the SAW velocity, effectively leading to a more rapid change in the potential.

The consequences of this for the generation of coherent states is shown in Figs. (5.7) and (5.8), which show the results of simulating electron motion with two different SAW amplitudes. We now use a gate design similar to that shown in Fig. (5.3), except multiple gates are used so that the potential in the three regions of the figure can be independently controlled. The voltages applied to the

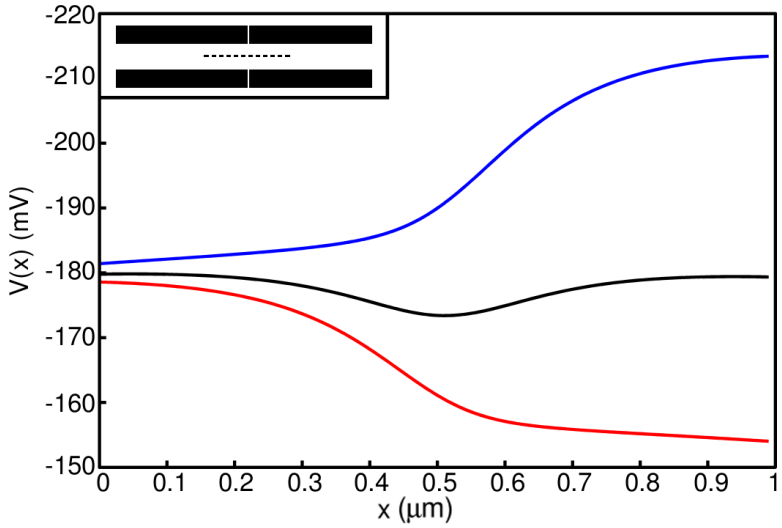

*Figure 5.5: Potential along the centre of the Q1DC with gate design shown in the inset. The two left gates are both at -1 V throughout, and the two right gates are at -0.8 V (red curve), -1 V (black curve) and -1.2 V (blue curve). The potentials are calculated along the dashed line (*1 μm *in length) shown in the inset.*

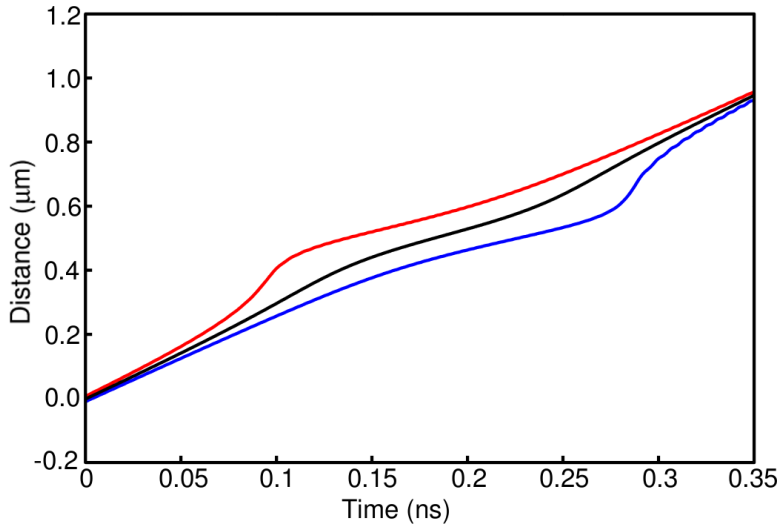

Figure 5.6: Average x position of an electron carried in a SAW along a Q1DC. The three lines correspond to the three potentials plotted in Fig. (5.5).

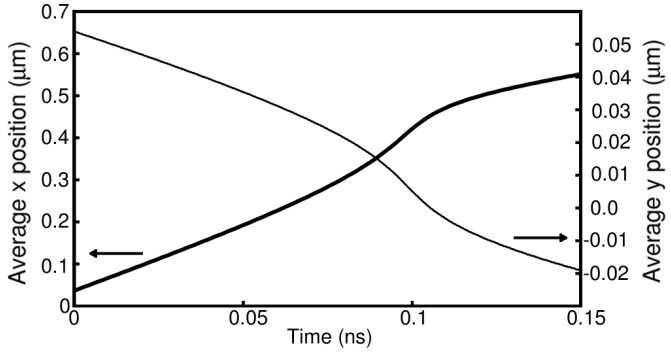

Figure 5.7: Average position of an electron carried by a SAW along a kinked channel, with a SAW amplitude of 35 mV. The position varies smoothly with time. Thick line, left axis: average x position. Thin line, right axis: average y position.

gates are chosen so that the potential in region 2 of Fig. (5.3) is lower than region 1. The electron thus experiences a "downhill" potential as it is carried along the channel, similar to the red line of Fig. (5.5). With a SAW amplitude of 35 mV (Fig. (5.7)), the electron accelerates around the time ~ 0.1 ns but the change in potential is insufficiently abrupt to excite the electron into a coherent state. However, reducing the SAW amplitude slightly to 31.5 mV (Fig. (5.8)) leads to greater acceleration, and the average position of the electron then oscillates with time. The direction of oscillation is approximately parallel to the angled part of the channel, and so in this instance the amplitude of the x oscillation (~ 25 nm) is greater than that of the y oscillation (~ 5 nm). It should be possible to change the relative amplitudes of these oscillations by changing the angle between the different sections of the channel. The slight decrease in the oscillation amplitude at later times in Fig. (5.8) is due to an essentially classical effect: there is a slight increase in the potential experienced by the electron in region 3 of Fig. (5.3) due to the gate design used, leading to a slight reduction in the kinetic energy.

5.6 Effect upon two-channel oscillation

Having shown how coherent states may be generated in a SAW device, it is now pertinent to ask how they could be detected experimentally. We therefore now repeat the numerical simulations that were first seen in Chapter 4 of electron

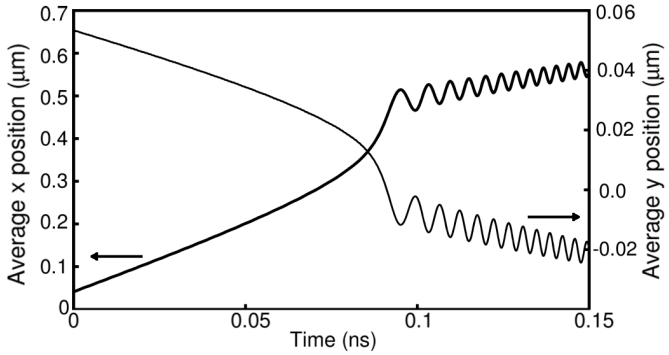

Figure 5.8: Average position of an electron carried by a SAW along a kinked channel, with a SAW amplitude of 31.5 mV. The position oscillates after approximately 90 ps. Thick line, left axis: average x position. Thin line, right axis: average y position.

oscillation between two parallel SAW channels separated by a tunnelling barrier, but now using coherent and squeezed initial states. This will model the effect of changing either the position or width of a 1D channel, which might arise in an experiment from an unwanted perturbation. An alternative scheme for measuring an electron which oscillates from side to side in a SAW channel will be presented in Chapter 6.

Figure (5.9) shows the central region of the simulated device. The electron oscillates between the two channels as a function of time, and the frequency of this oscillation is altered by changing the voltage applied to the gates labelled "TC" and "Barrier". A full discussion of this effect can be found in Chapter 4. Setting the TC voltage to -700 mV creates a symmetric double-well potential, and changing the TC voltage then leads to a transverse electric field. For the gate voltages used here, $\hbar\omega \simeq 2$ meV in the entrance leads to the left of the tunnel barrier. As discussed in Section (5.4), a displacement of $\sim$40 nm (so that $\alpha = 1.2$) is then sufficient to generate approximately orthogonal states which could be used as a qubit.

The ground state of a SAW minimum in the (top) entrance lead is determined numerically and then displaced laterally by 40 nm. The probability that the electron occupies the top channel (and so exits to the top-right of the device) is calculated by numerically solving the time-dependent Schrödinger equation and plotted in Fig. (5.10). Similarly, to simulate the effects of a squeezed state, the

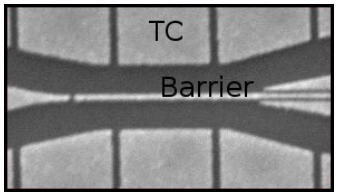

Figure 5.9: SEM image of the simulated device, which consists of two parallel SAW channels separated by a narrow barrier. The importance of the gate labelled TC is discussed in the text.

numerically-determined ground state is reduced in width without altering the mean position. The reduction in width that can be simulated numerically is limited in practice by the computational grid size – the grid spacing must be much less than the length scale over which the wavefunction changes appreciably. Figure (5.11) shows the simulation results for a wavefunction which has had the standard deviation reduced to 40% of the ground state standard deviation. (From Eq. (5.13), this corresponds to a squeezing parameter $\zeta = 0.459$.)

In both Figs. (5.10) and (5.11), at any given TC voltage the probability that the electron occupies the top channel after being carried past the tunnel barrier exhibits complicated oscillatory behaviour as a function of the barrier voltage. A second-order Butterworth filter [116] is therefore applied to separate the low- and high-frequency behaviour. Some of the features seen in Fig. (5.10) can be simply explained by considering the behaviour of the instantaneous eigenstates and eigenenergies in the tunnelling region as a function of the gate voltages. We define the energy difference of two eigenstates to be $\Delta_{ij} = |E_i - E_j|$ where E_i is the eigenenergy of state $|i\rangle$. A wavefunction which is a linear superposition of two states will have an oscillating probability density, and the frequency of this oscillation is $\omega_{ij} = \Delta_{ij}/\hbar$. From Eq. (5.10), a coherent state can be written as a Poissonian superposition of the eigenstates of a harmonic oscillator. Figure (5.2) shows that for a displacement of $\alpha = 1.2$, the probability $|p_n|^2$ of occupying an eigenstate with $n > 5$ is less than 1%. Most of the dynamical behaviour should therefore be understandable from a consideration of the first six eigenstates. These eigenstates are plotted in Fig. (5.12), and it should be noted that

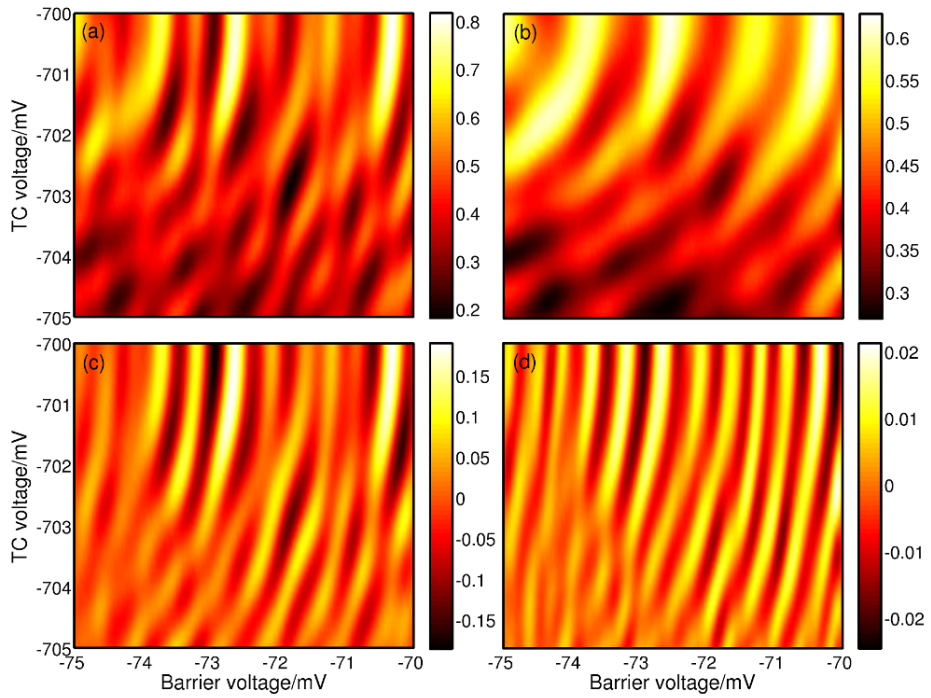

Figure 5.10: Simulation results for an initial state displaced laterally by 40 nm, with parts (b)-(d) showing the data after applying a second-order Butterworth filter as a function of the barrier voltage. The colour scale in a) and b) shows the probability of remaining in the SAW dot at the end of the simulation. In c) and d) the low-frequency background has been removed and the colour scale shows the variation in probability with respect to the background. a) Simulation results. b) Low frequency ($< 500V^{-1}$). c) High frequency ($> 500V^{-1}$). d) Higher frequency ($> 1500V^{-1}$).

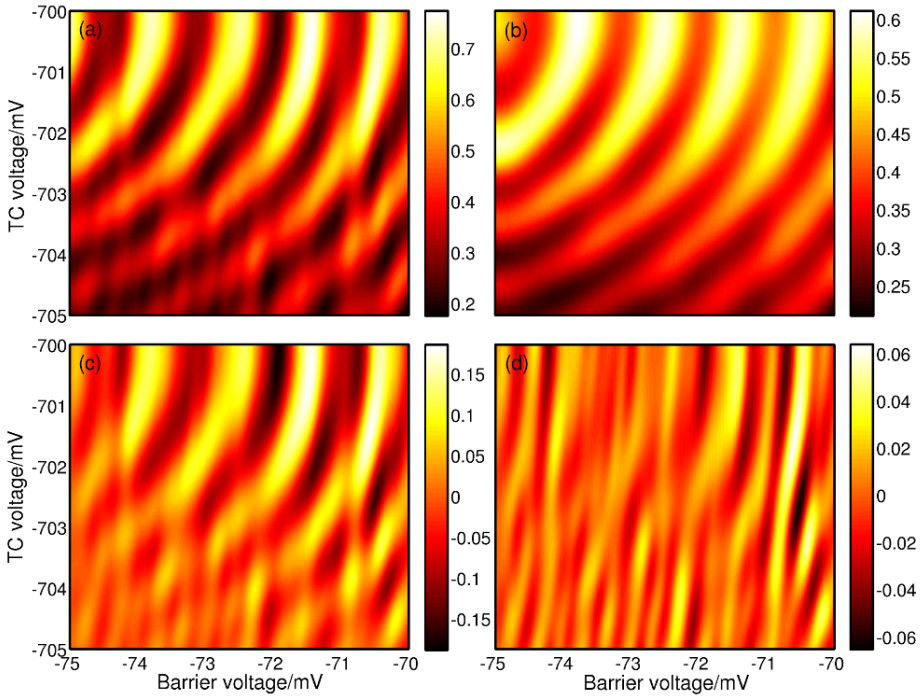

Figure 5.11: Simulation results for an initial state squeezed in width to 40%, with parts (b)-(d) showing the data after applying a second-order Butterworth filter as a function of the barrier voltage. The colour scale in a) and b) shows the probability of remaining in the SAW dot at the end of the simulation. In c) and d) the low-frequency background has been removed and the colour scale shows the variation in probability with respect to the background. a) Simulation results. b) Low frequency ($< 200V^{-1}$). c) Higher frequency ($> 200V^{-1}$). d) High frequency ($> 400V^{-1}$).

for all of the simulations performed here only the states $|0\rangle$ and $|1\rangle$ have a lower energy than the highest point of the barrier.

The low-frequency behaviour in Fig. (5.10b) is very similar to the oscillations seen for a two-level system in the previous chapter, and arises from oscillation between the $|0\rangle$ and $|1\rangle$ states. The linear combinations $|0\rangle \pm |1\rangle$ (we neglect a normalisation constant for brevity) are localised to one side of the barrier or the other, and in a similar manner the probability density for the states $|3\rangle \pm |5\rangle$ in Fig. (5.12) is almost entirely localised to either the upper or lower channel.

As the $|0\rangle$ and $|1\rangle$ states can be thought of as the symmetric and antisymmetric superpositions of two approximately Gaussian states which are localised to one

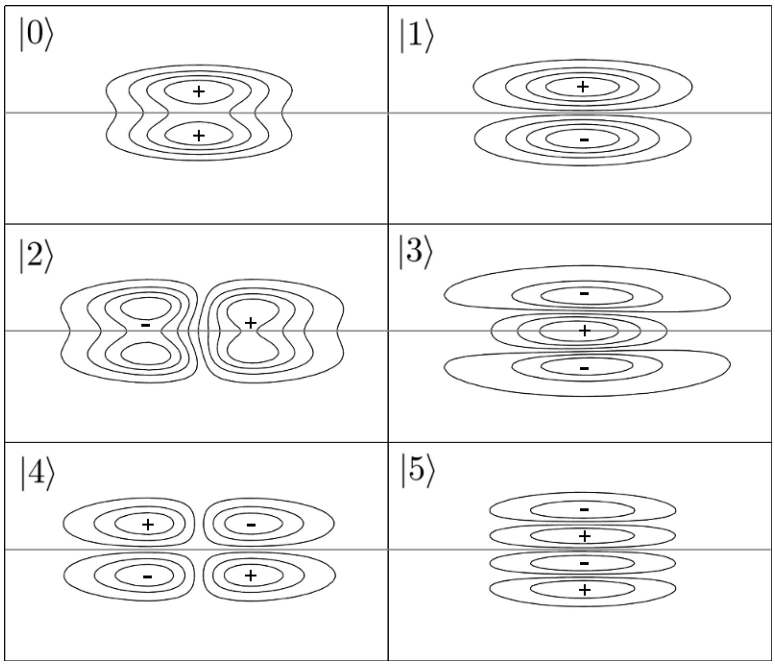

Figure 5.12: Contour plots of first six eigenfunctions at the centre of the SAW two-channel device. The grey line indicates the position of the tunnel barrier, and each plot shows a region which is 270×500 *nm.*

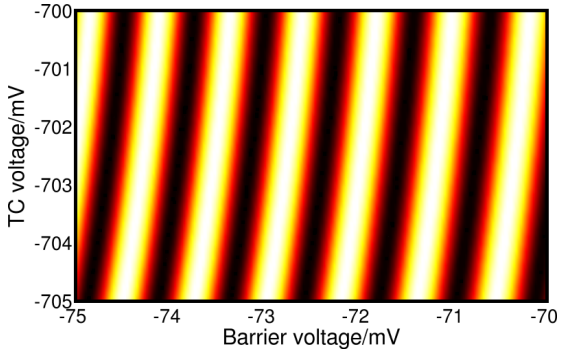

Figure 5.13: Expected behaviour of oscillations between symmetric and antisymmetric combinations of states $|3\rangle$ *and* $|5\rangle$ *in Fig. (5.12).*

or other of the channels, the energy difference Δ_{01} depends upon the overlap of these localised states. Changing the TC voltage will significantly change the penetration of the two localised states into the tunnel barrier, so Δ_{01} will be sensitive to changes in the TC voltage. Although similar considerations apply to the energy difference Δ_{35}, the states $|3\rangle$ and $|5\rangle$ are higher in energy than the barrier and so the dependence of Δ_{35} on the TC voltage will be weaker than that of Δ_{01}. Following the results in Section (4.4), the probability of remaining in the upper channel after a time T has elapsed is expected to be roughly $P_{35} \simeq \sin^2(\Delta_{35}T/\hbar)$. The energy difference Δ_{35} was found for the entire range of voltages from a numerical calculation of the eigenenergies, and P_{35} is plotted in Fig. (5.13) for a tunnelling region of length $T = 0.6$ ns. The figure shows a set of oscillations which are qualitatively similar to those seen in Fig. (5.10d), and in particular the weak dependence on TC voltage (relative to the $|0\rangle \leftrightarrow |1\rangle$ oscillation) is reproduced.

The amplitude of these high-frequency oscillations in the simulation is an order of magnitude less than the low-frequency behaviour arising from the $|0\rangle \leftrightarrow |1\rangle$ oscillation. From Eq. (5.10), $|\langle \alpha = 1.2|n = 5\rangle|^2 = 0.01$ so it is expected that the $|3\rangle \leftrightarrow |5\rangle$ oscillation be of much lower visibility. The superpositions $|2\rangle \pm |4\rangle$ correspond to a state which oscillates between the two channels as in the $|0\rangle \leftrightarrow |1\rangle$ case but with an added oscillation parallel to the direction of SAW motion (i.e., the overall behaviour is to oscillate diagonally). The extra oscillation parallel to

the SAW direction does not affect which channel is occupied, and so for these states the behaviour is found to be essentially identical to the $|0\rangle \leftrightarrow |1\rangle$ case.

Although the results for a squeezed state shown in Fig. (5.11) show some features which are broadly similar to those for the coherent state, the high-frequency behaviour shows more complex structure, and at present we have no simple physical description to offer for this. It is an open question whether or not plots such as those in Figs. (5.10) and (5.11) would be experimentally distinguishable given that the detailed structure in these plots is of relatively small amplitude. In practice, an experimental study would examine how such oscillations depend upon multiple gate voltages which change either the displacement or the width of the initial state, and it is likely that this would reveal differences between the two situations.

5.7 Conclusions

The focus of this chapter was an examination of coherent and squeezed states, which are excited states of the quantum harmonic oscillator which have a Gaussian wavefunction. These excited states might arise either due to a deliberate manipulation of an electron or an unwanted perturbation due to interaction with the environment. After reviewing the mathematical properties of these states some applications were discussed, and we saw that coherent states are a potentially useful resource in QIP. We then discussed how an electronic coherent state could be generated in a SAW device; this requires a sudden change in the potential experienced by the electron. The amplitude of the SAW was found to be a crucial factor – if the amplitude is too large the electron adiabatically follows the SAW minimum and remains in an instantaneous eigenstate. We then examined the effect that using coherent and squeezed states has upon the coherent oscillation of an electron between two parallel SAW channels separated by a tunnel barrier. This led to a modification of the results from the previous chapter, and the general behaviour was understood by considering how the spectrum of the double-well potential of such a device depends upon the voltages applied to the gates around the barrier region.

He that breaks a thing to find out what it is has left the path of wisdom.

Gandalf

6 Nonadiabatic dynamics

6.1 Introduction

This chapter will present a technique that can be used to create and measure nonadiabatic electron dynamics in a SAW device. After reviewing what the notion of adiabaticity means in quantum mechanics, the SAW device which will be studied in this chapter will be described. The device uses SAWs to carry an electron in a dynamic quantum dot past a tunnelling barrier. If the electron experiences a rapidly-changing potential it will be nonadiabatically excited, and the subsequent tunnelling current through the barrier can be used as a probe of this motion.

The energy spacing in a typical SAW dot is $\sim$ 1 meV, and a linear superposition of two states with this energy spacing will oscillate with a time period of $\sim$ 4 ps. Probing picosecond motion in semiconductor devices is extremely challenging, as it requires experimental parameters (such as gate voltages) to be pulsed on a picosecond timescale which is beyond typical experimental band-

widths. Also, Rahman *et al.* [117] showed that applying short voltage pulses ($\sim$ 100 ps duration) to gates will generate surface acoustic waves which could introduce unwanted effects in experiments on double dots such as those performed by Hayashi *et al.* [46] and Gorman *et al.* [47]. The technique introduced here does not require such pulses, instead taking advantage of the motion of a SAW to create a time-varying potential.

We will perform numerical simulations of the SAW device, and the simulation results will be seen to be in good agreement with experimental data. The simulations will explain the effect that changing the gate voltages around the barrier region has upon the measured tunnelling current, as well as explaining the effect of a perpendicular magnetic field. We will finally show that the tunnel barrier device could also be used to provide information about the initial state of the electron before the tunnelling region.

6.2 Adiabaticity in quantum mechanics

Adiabatic evolution is often associated with thermodynamic processes: in that context, it means a process which happens infinitesimally slowly so that the energy of the system does not change. One can extend this definition to quantum mechanics to consider quantum mechanical systems with Hamiltonians that change slowly with time, as follows.

We begin by considering the time-dependent Schrödinger equation for a time-dependent Hamiltonian $H(t)$,

$$i\hbar\frac{\partial\psi(t)}{\partial t} = H(t)\psi(t) \tag{6.1}$$

where we neglect the spatial dependence of H and ψ for notational brevity. We then define the unitary operator $U(t)$ that diagonalises the instantaneous Hamiltonian $H(t)$,

$$U^{-1}(t)H(t)U(t) = D(t) \tag{6.2}$$

so that $D(t)$ is diagonal, and we also define $\psi'(t)$ such that

$$U(t)\psi'(t) \equiv \psi(t) \tag{6.3}$$

Substituting Eqs. (6.2) and (6.3) into Eq. (6.1),

$$i\hbar\frac{\partial(U\psi')}{\partial t} = i\hbar\left(U\frac{\partial\psi'}{\partial t}+\frac{\partial U}{\partial t}\psi'\right) = HU\psi' \tag{6.4}$$

$$i\hbar\frac{\partial\psi'}{\partial t} = D\psi' - i\hbar U^{-1}\frac{\partial U}{\partial t}\psi' \tag{6.5}$$

where Eq. (6.4) has been left-multiplied by U^{-1} to arrive at Eq. (6.5). If H only changes slowly with time, then U and U^{-1} will also change slowly and the second term on the right hand side of Eq. (6.5) can be neglected. In this limit (given that D is diagonal by definition) if the initial state $\psi(0)$ is an eigenfunction of $H(0)$ then $\psi(t)$ will be an eigenstate of $H(t)$ for all time. Conversely, if the Hamiltonian (and therefore the time evolution operator) change sufficiently quickly with time then the time evolution will be *nonadiabatic*: the wavefunction will be excited into a linear superposition of the instantaneous eigenstates of the system.

The requirement that H "changes slowly with time" is often encoded in the requirement that [118]

$$\left|\frac{\langle E_m(t)|\dot{E}_n(t)\rangle}{E_m(t)-E_n(t)}\right| \ll 1 \tag{6.6}$$

where E_n and $|E_n\rangle$ are the instantaneous eigenvalues and eigenstates of a time-varying Hamiltonian. However, there has been much recent debate over whether this condition is sufficient in general [118–123] and Du *et al.* [124] have demonstrated experimentally that nonadiabatic effects are possible even if the above condition is satisfied. It is therefore worthwhile to develop new techniques that can probe nonadiabatic quantum behaviour.

Studying nonadiabatic quantum dynamics is also of interest more generally for the problem of electron transport in low dimensional systems. The Landauer-Büttiker formalism [125, 126] is often used to calculate the conductance through constrictions, and assumes that all incoming and outgoing waves are at the Fermi energy. However, nonadiabatic effects may lead to scattering which would invalidate this assumption. Similarly, the Kubo-Greenwood formalism [127] involves a first-order perturbation expansion to solve the time-dependent Schrödinger equation and neglects higher order processes. Payne [128] used a one dimensional potential of changing width as a description of a Q1DC, and showed that exci-

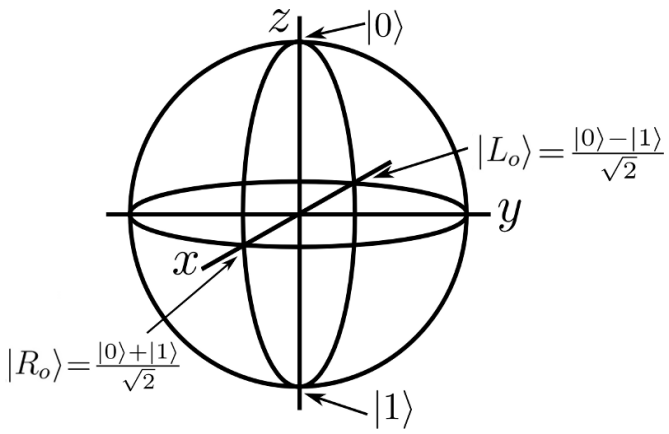

Figure 6.1: Bloch sphere representation used in this chapter.

tation into higher states is inevitable regardless of the rate at which the channel width is changed. Tang [129] then investigated the transmission probability of a wavepacket through a Q1DC using numerical simulations and found that nonadiabatic excitations led to a small deviation from the Landauer-Büttiker result. Thus, although nonadiabatic effects are often neglected in standard theory they may be needed for a complete description of low dimensional transport.

6.3 Notation and Bloch sphere

Much of the discussion in this chapter will centre upon potentials that are either harmonic or can be well approximated as harmonic. As a main focus of the discussion is the manipulation of quantum states, we will begin by defining some notation in the Bloch sphere representation. The nth eigenstate of a potential will be written $|n\rangle$, and in particular the first two eigenstates will be labelled $|0\rangle$ and $|1\rangle$. Also, we define two particular linear combinations of these states: $|L_o\rangle = (|0\rangle - |1\rangle)/\sqrt{2}$ and $|R_o\rangle = (|0\rangle + |1\rangle)/\sqrt{2}$. The $|0\rangle$ and $|1\rangle$ states will be placed on the z axis at the poles of the Bloch sphere, so the $|L_o\rangle$ and $|R_o\rangle$ states are located at opposite points on the x axis. σ_x and σ_z rotations in the $\{|0\rangle, |1\rangle\}$ basis can therefore be thought of as σ_z and σ_x rotations respectively in the $\{|L_o\rangle, |R_o\rangle\}$ basis. This notation is summarised in Fig. (6.1). Another set of important states will be denoted by $|L\rangle$ and $|R\rangle$, defined as $\alpha|0\rangle \pm \beta|1\rangle$ with

$|\alpha|^2+|\beta|^2=1$. The probability density of the $|L\rangle$ and $|R\rangle$ states will be displaced towards either the left or right of the dot, but the two states are not orthogonal unless $|\alpha|=|\beta|=1/\sqrt{2}$.

6.4 Creating & probing nonadiabatic dynamics

In this section we will describe the main features of the model for creating and measuring nonadiabatic excitation. A 1D potential well is used to represent a quantum dot (Fig. (6.2a)), and to the right hand side of this dot is a time-varying barrier (Fig. (6.2b)) which couples the dot to a reservoir. The barrier height is quickly lowered to excite nonadiabatic motion, and Fig. (6.2c) and Fig. (6.2d) show how the numerically-calculated probability density evolves with time for the cases of weak and strong dot-reservoir coupling respectively. In both cases the wavefunction oscillates from side to side at a frequency which is dependent upon the shape of the potential well. The first two eigenstates of the potential are plotted in Fig. (6.2e), and the $|L\rangle$ and $|R\rangle$ states arising from two linear combinations of these two states is shown in Fig. (6.2f). For the calculation presented in Fig. (6.2) this pair of states can be written $0.92|0\rangle \pm 0.38|1\rangle$ (there is negligible excitation into higher states), although we emphasise that the precise value of the coefficients is unimportant to this description. The important property of the $|L\rangle$ and $|R\rangle$ states is that the $|L\rangle$ state has essentially no overlap with the barrier and so has a much lower tunnelling rate than the state $|R\rangle$. The probability that the wavefunction remains in the dot as a function of time therefore exhibits a series of steps (shown in Fig. (6.3)) as the electron oscillates from side to side. The frequency of the oscillation depends upon the energy difference ΔE between the $|0\rangle$ and $|1\rangle$ states of Fig. (6.2e), and this can be controlled by changing the shape of the dot. For a fixed tunnelling time, changing the oscillation frequency is therefore expected to lead to an oscillatory behaviour in the probability that the wavefunction remains in the dot after the barrier height is raised to decouple the dot from the reservoir.

To summarise, this description consists of two key features. Firstly, a rapidly-changing potential is used to nonadiabatically excite an electron into a state which is displaced to one side in a quantum dot. Secondly, this leads to a probability

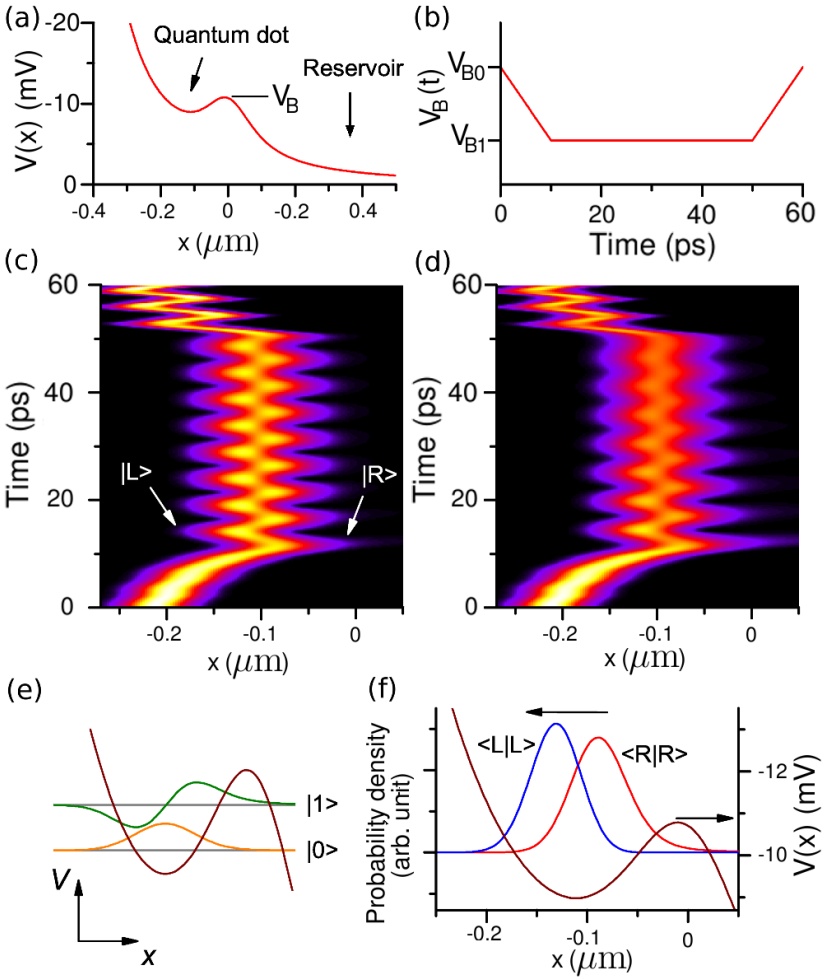

Figure 6.2: Nonadiabatic model. a) 1D potential defining a quantum dot adjacent to a reservoir. b) Variation of barrier height with time. c) and d) Time evolution of the probability density for a high tunnel barrier (c) and a low tunnel barrier (d); brighter colours indicate a higher probability density. e) First two eigenstates of the potential in (a). f) States with probability density displaced towards the left $|L\rangle$ and right $|R\rangle$ of the dot.

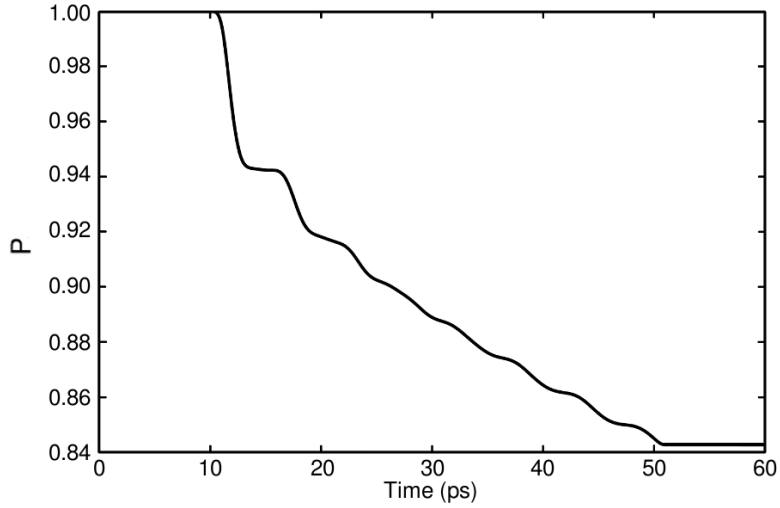

Figure 6.3: Probability P of electron being in the dot of Fig. (6.2a). For the first and last 10 ps the barrier completely suppresses tunnelling. In the middle 40 ps the wavefunction oscillates from side to side; when it is at the right hand side of the dot the wavefunction tunnels out at a greater rate than when at the left side.

density which oscillates from side to side at a frequency which can be controlled by changing the shape of the dot. If one side of the dot is then coupled to a reservoir, this dynamical behaviour leads to a tunnelling probability which also oscillates with time.

6.5 Description of experimental device

In order to verify that the technique discussed in Section (6.4) can be used to create and probe picosecond motion, Masaya Kataoka and Mike Astley [52] have performed a series of measurements on the device shown in Fig. (6.4), and all of the experimental data that will be shown in this chapter was provided by them. The device consists of two parallel channels separated by a tunnelling barrier. The voltages applied to the gates defining the top channel are sufficiently negative to completely deplete the 2DEG there, so when a SAW is applied a series of dynamic quantum dots move along the upper channel. The voltage applied to the gate at the entrance to the upper channel is chosen to ensure that each SAW minimum carries a single electron. The gates around the lower channel are only weakly

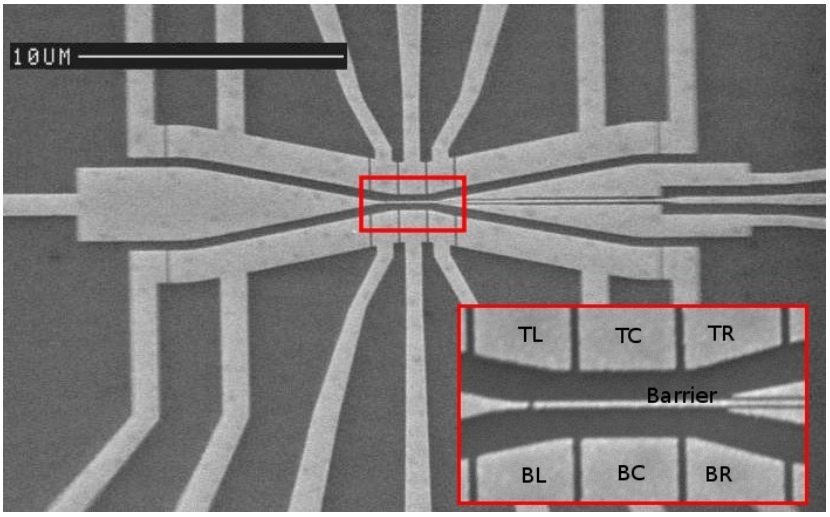

Figure 6.4: Scanning electron microscope image of two-channel SAW device. The inset shows the barrier region and the seven gates around it. A transducer to the left of the device (not shown) generates SAWs which travel from left to right, and the regions at the four corners are contacted with independent Ohmic contacts.

defined, so there is a quasi-1D reservoir connecting the lower-right 2DEG to the lower channel, and this reservoir extends to the barrier region. Figure (6.5) shows a typical potential landscape around the barrier, calculated using the method from Section (2.5.1). The entrance gate to the lower channel is pinched off, so no SAW current flows in this channel. Due to the presence of electrons in the lower channel we expect the SAW to be strongly screened there, and it will be assumed that the SAW has negligible amplitude in the lower channel. Each of the SAW-defined dynamic quantum dots in the upper channel therefore constitutes a quantum dot as shown in Fig. (6.2a), whilst the reservoir in that figure is provided by the lower channel. It should be noted that although all of the data shown here has the electron tunnelling from a SAW dot in the top channel into a reservoir in the bottom channel, similar results were seen when the roles of the two channels were reversed.

The tunnelling region is defined by the seven gates shown in the inset to Fig. (6.4). The three gates that define the top channel will be referred to as TL (top-left), TC (top-centre) and TR (top-right). Similarly, the three gates on the bottom channel will be referred to as BL, BC and BR, and the two channels

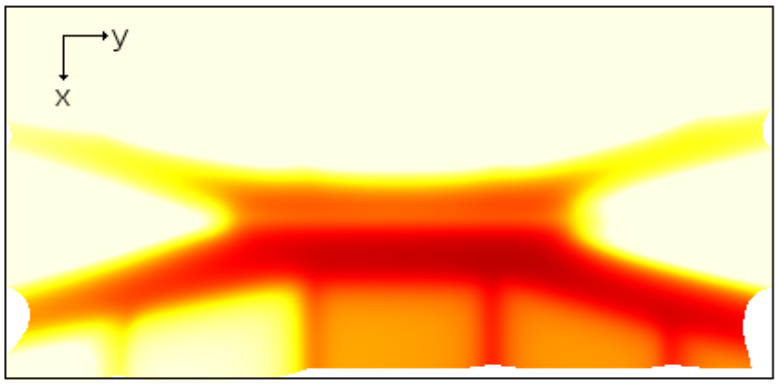

Figure 6.5: Potential arising from the gate design in Fig. (6.4). The top channel is depleted and has electrons injected into it by a SAW (not shown), travelling from left to right. The bottom channel is weakly defined and so forms a 1D reservoir connecting to the bottom right region. Brighter colours correspond to higher potential.

are then separated by the barrier gate. The voltage on the barrier gate will be denoted V_{bar}, whilst the voltages on the other six gates will be labelled V_{TC}, etc.

6.6 Modelling the experimental device

The experimental device will be modelled using a simple 1D potential. Although a 2D description might be more desirable, such an approach has some difficulties. The probability weight that tunnels out of the dot needs to be drained into a reservoir, which requires either absorbing boundary conditions or an extremely large computational domain. It is difficult to implement the former without introducing some inaccuracy, and as it is anticipated that we may be interested in very small variations of the tunnelling rate such a technique is undesirable. The alternative of using a large domain is impractical, as it greatly increases the computational resources required. Another difficulty with the 2D simulations is the length of time they take: in Section (6.8) we will present results for around 30,000 gate voltages. The 2D simulations presented in Chapter 4 take around 1–2 hours each, whereas the 1D simulations to be presented here each take no more than a few minutes. It is therefore extremely desirable to investigate a 1D model, which we will see is sufficient to capture the essential details of the physics.

The main goal of the later sections will be to perform simulations that can be easily compared to the experimental data. It is therefore best to have as few adjustable parameters in the simulation as possible. Therefore, only two gates from the device shown in Fig. (6.4) will be considered: the barrier and TC gates. By varying the voltages applied to these two gates as a function of time it is possible to generate a potential that is qualitatively similar to the potential that arises due to the full gate design in Fig. (6.4). Considering only these two gates allows the number of parameters that need to be tuned in the simulation to be greatly reduced. The reservoir is included in the model by extending the computational domain outside of the dot for a few tens of microns; this ensures that any part of the wavefunction that leaves the dot simply propagates away and does not interfere with the wavefunction that remains in the SAW dot. This represents the fact that in the experiment, any probability weight leaving the dot enters the quasi-1D reservoir in the lower channel and is then drained to an Ohmic contact at the bottom-right of the device.

When the SAW carries electrons (assumed to be in the ground state of the dot at the start of the simulation) from the entrance lead into the barrier region, the electron receives a nonadiabatic perturbation in the x direction due to a rapidly changing potential. Although it is possible that the gate geometry causes such an effect, the experimental results that will be discussed in Section (6.8) suggest that the perturbation is most likely due to an impurity potential. The main source of impurities is the randomly located ionised donors in the donor layer. This disorder will randomly make the barrier potential depicted in Fig. (6.5) weaker or stronger at different positions. As tunnelling through a barrier is typically exponentially sensitive to both barrier height and width, the dominant tunnelling contribution will therefore arise from the weakest part of the barrier. In order to approximate the changing barrier potential in the model, in the simulations the barrier gate voltage will be varied in time as follows. At the start of the simulation, a voltage of -0.5 V is applied to the barrier gate which ensures that the SAW dot is decoupled from the reservoir. The voltage is linearly decreased to some fixed voltage over 10 ps (see Fig. (6.2b)). This change will later be seen to be sufficiently rapid to be nonadiabatic, so induces a transition from the initial $|0\rangle$ state. The barrier gate voltage is then held constant for 40 ps during which

time the electron can tunnel into the reservoir. Finally, the barrier gate voltage is raised back to -0.5 V, again decoupling the SAW dot from the reservoir.

The exact form of the potential due to disorder is unknown, and due to its random nature it will be impossible to quantify exactly for a given experimental device. It is possible, however, to estimate the relevant length and energy scales of the potential arising due to disorder. The relevant length is the minimum distance from the 2DEG to the dopants. In the device considered here this distance is the thickness of the spacer layer, 40 nm. Given the SAW velocity of 2800 m/s this length scale corresponds to a time of 14 ps. A reasonable energy scale to use is the Coulomb potential arising from a point charge; at a distance of 40 nm this is 2.8 meV in GaAs. For comparison, we can use the results from Section (2.5.1) to calculate the change in potential at the 2DEG due to modifying the barrier gate voltage in the manner described above. The barrier gate voltages applied in the central 40 ps of the simulation will be of the order of -0.1 V. Given the initially applied voltage of -0.5 V, this is found to correspond to a $\sim$ 5 meV change in the height of the barrier potential. Having the barrier gate voltage change from -0.5 V in a 10 ps time is therefore not an unreasonable way to account for the effect a nearby charged impurity has on the barrier potential.

6.7 Other experimental considerations

In order for the proposed effect to be experimentally visible, the electron must remain in a coherent superposition for a time comparable to (or greater than) the 40 ps tunnelling time. One potential mechanism which would prevent this occurring is incoherent thermalisation. The experimental data in the following sections was taken at a temperature of 270 mK, corresponding to an energy of 23 μeV. This energy is very much smaller than the difference in energy between the two states, ΔE, and so thermal effects can be neglected. Another possible decoherence mechanism is electron-phonon interaction. As $\Delta E \gg kT$, only spontaneous phonon emission needs to be considered. Phonon emission from a quantum dot is greatly suppressed relative to bulk systems due to dots possessing a quantised spectrum, an effect sometimes known as the "phonon bottleneck" [130]. Typical scattering times due to acoustic phonon emission in GaAs quantum

dots have been calculated to be in the range of 100 ps – 10 ns (see, for example, Refs. [131, 132]). Also, Hayashi *et al.* [46] have observed coherent charge oscillations in a GaAs double quantum dot with a coherence time of approximately 1 ns. It is therefore expected that spontaneous phonon emission can be neglected given that the timescales considered here are a few 10s of picoseconds.

6.8 Gate voltage data

Figure (6.6) shows how the measured output current from the top SAW channel depends upon the voltages applied to the TC and TL gates depicted in Fig. (6.4). As the TC gate is made more negative the output current drops, because the electron is pushed closer to the tunnel barrier. The change in the tunnelling current appears to be fairly smooth, which is what one typically expects from tunnelling. However, oscillations are revealed if a smoothly-varying background contribution to the current is removed using a filter. The experimental data was taken by sweeping the TC voltage for each TL voltage, and so the filtering was performed in the TC direction. A second-order Butterworth bandpass filter [116] was used; the slowly-varying contribution is removed by filtering out frequencies below 21.4 V^{-1}, and noise above a frequency of 685.7 V^{-1} was also removed. The oscillations revealed after this filtering are shown in Fig. (6.6). The crescent-like features are of an unknown origin, but we see a set of oscillations in TC voltage that vary only very weakly as the TL gate is changed.

This behaviour is consistent with the model described earlier: as the TC gate voltage is swept, the confinement potential (and so the frequency of oscillation between the $|L\rangle$ and $|R\rangle$ states) is changed. Figure (6.3) showed that the occupation probability of the SAW dot exhibits a series of steps as a function of time, which is due to the very different tunnelling rates of the $|L\rangle$ and $|R\rangle$ states. Once the smoothly-varying contribution has been filtered out, the maxima in the filtered current flowing from the top channel seen in Fig. (6.6) correspond to situations where the final state of the wavefunction is $|L\rangle$ whilst the minima correspond to the final state being $|R\rangle$.

Figure (6.6) shows that the oscillations change only very weakly as the TL voltage is changed: although this gate could have a small effect on the confinement

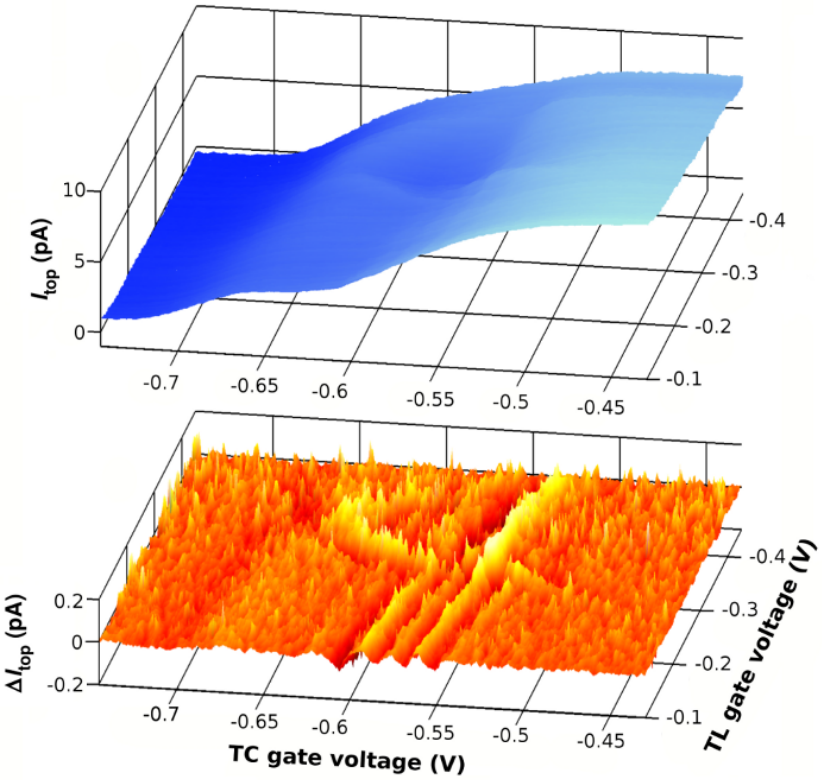

Figure 6.6: Behaviour of measured current with TC and TL voltage. Top: Output current I_{top} from the top channel. Bottom: Oscillations in the current ΔI_{top} appear when a slowly-varying contribution is removed from I_{top}. The origin of the curved feature around -0.3 V in TL voltage is unknown.

potential in the barrier region, it is further from the barrier region than the TC gate so should have a much-reduced effect (the TC oscillation period is of the order of 10 mV, whereas the TL range in Fig. (6.6) is ~ 0.3 V). This also implies that the dominant tunnelling contribution arises around the centre of the barrier region, as discussed in Section (6.6).

We next consider the behaviour of the oscillations as the barrier gate voltage is swept. Figure (6.7) shows the experimental data, again after filtering (frequencies below 35 V^{-1} and above 900 V^{-1} were removed). The oscillations move to a more negative TC voltage when the barrier gate is made more negative. This behaviour is reproduced in the results from the simulation; these results are also shown in Fig. (6.7) for comparison. The probability of remaining in the dot after the end of the tunnelling region can be calculated from the dynamical simulations. As in the experiments, a low-frequency background contribution is present and this was removed with a high-pass filter with a cutoff frequency of 18.75 V^{-1}. Making the barrier gate more negative increases the confinement of the SAW dot, and thus increases the side-to-side oscillation frequency. However, making the TC gate more negative weakens the confinement. If the barrier were *not* present (making the channel quasi-harmonic) a more negative TC voltage would increase the confinement energy. However, the anharmonicity introduced by the presence of the barrier means a more negative TC voltage has the opposite effect, as is clear from the behaviour of the oscillations in the simulation. Intuitively, this can be understood by considering the fact that making the TC gate more negative will not only change the shape of the dot but also effectively corresponds to weakening the barrier because the dot is raised in energy.

There is good agreement between the behaviour of the oscillations in the simulation and in the experimental data. In both cases, the oscillations have similar periods in TC and barrier voltages. The variation in probability of remaining in the SAW dot in the simulation ($\Delta p \simeq 0.05$) corresponds to an expected oscillation of 0.4 pA in the measured current, which is larger than the measured value of 0.1 pA. However, we expect the oscillation amplitude achieved in the simulation to be an upper bound on what is observed experimentally: for example, decoherence mechanisms will act to decrease the experimentally-observed oscillation amplitude.

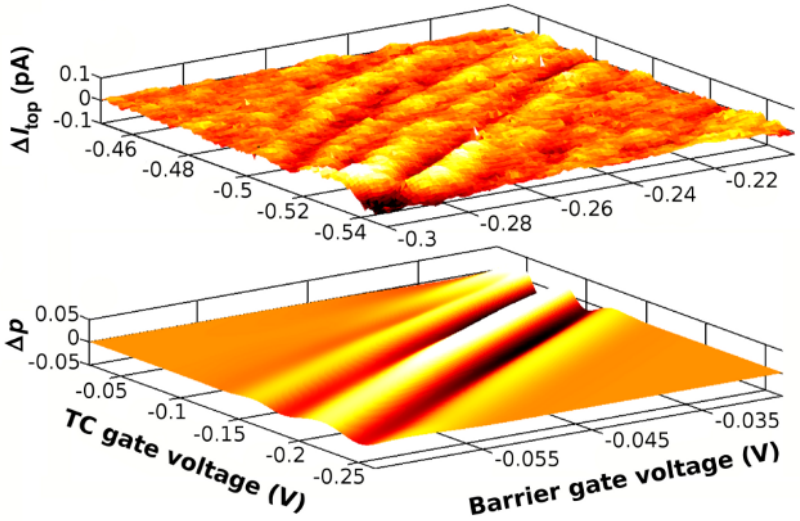

Figure 6.7: Behaviour of oscillations with TC and barrier voltage. Top: experimental data. Bottom: result from simulations, showing filtered probability Δp of remaining in the SAW dot.

The simulation results also explain why only a limited number of oscillations are visible. If the tunnelling rate is too large, the probability of remaining in the SAW dot drops to zero and so no oscillation in the final current is possible. Conversely, if the tunnelling rate is too small there will no tunnelling current to measure. The former case corresponds to the right-hand region of Fig. (6.7), whilst the left-hand region corresponds to the latter. Although this leads to a window of gate voltages in which the oscillating tunnelling current can be measured, the nonadiabatic excitation will still occur for a range of gate voltages outside this window.

6.9 Magnetic field data

Another parameter that can be varied experimentally is the strength of a perpendicular magnetic field; this is of interest because a magnetic field can be used to change the single-particle energy spacing (and thus the frequency of the side to side oscillation) in a dot. We begin by discussing how the eigenenergies

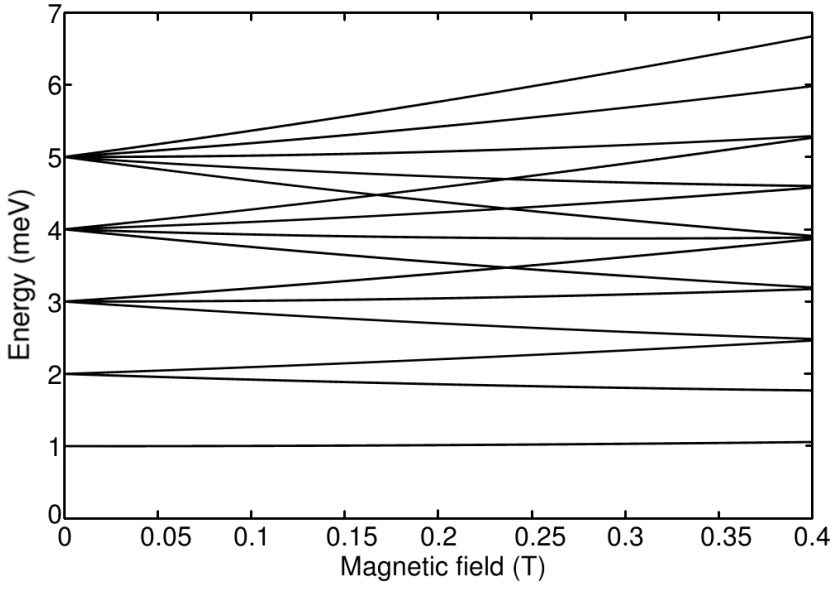

Figure 6.8: Darwin-Fock spectrum for the first few eigenstates of a circular quantum dot with energy gap $\hbar\omega = 1$ meV.

of a radially symmetric 2D quantum dot change in a perpendicular field. The eigenenergies of such a dot are described by the well-known Darwin-Fock spectrum [133, 134]. With a potential $V(r) = \frac{1}{2}m\omega_0^2 r^2$ (where $r^2 = x^2 + y^2$) and a perpendicular magnetic field of magnitude B, the eigenenergies are

$$E_{n,l} = \hbar\omega_c \left[b\left(n + \frac{1}{2}\right) + \frac{b|l| - l}{2} \right] \tag{6.7}$$

where $n = 0, 1, 2, 3\ldots$ and $l = 0, \pm 1, \pm 2\ldots$ are the usual quantum numbers,

$$b = \sqrt{1 + \frac{4\omega_0^2}{\omega_c^2}} \tag{6.8}$$

and the cyclotron frequency is $\omega_c = eB/m$. The first few eigenenergies for a dot with $\hbar\omega_0 = 1$ meV are plotted in Fig. (6.8).

The above result for a radially symmetric dot has been generalised by Madhav & Chakraborty [135] to the case of an elliptical dot described by the potential

$V = \frac{1}{2}m(\omega_x^2 x^2 + \omega_y^2 y^2)$. Defining

$$\Omega_{1,2}^2 = m^2(\omega_{x,y}^2 + \frac{1}{4}\omega_c^2) \tag{6.9}$$

$$\Omega_3^2 = [(\Omega_1^2 - \Omega_2^2)^2 + 2m^2\omega_c^2(\Omega_1^2 + \Omega_2^2)]^{1/2} \tag{6.10}$$

$$\alpha_1^2 = \frac{\Omega_1^2 + 3\Omega_2^2 + \Omega_3^2}{2(\Omega_1^2 + \Omega_2^2)} \tag{6.11}$$

$$\alpha_2^2 = \frac{3\Omega_1^2 + \Omega_2^2 - \Omega_3^2}{2(\Omega_1^2 + \Omega_2^2)} \tag{6.12}$$

$$\beta_1^2 = \frac{1}{4}\left(3\Omega_1^2 + \Omega_2^2 + \Omega_3^2\right) \tag{6.13}$$

$$\beta_2^2 = \frac{1}{4}\left(\Omega_1^2 + 3\Omega_2^2 - \Omega_3^2\right) \tag{6.14}$$

the energy levels of the elliptical dot in a magnetic field are then given by

$$E_{n_x',n_y'} = \left(n_x' + \frac{1}{2}\right)\frac{\alpha_1\beta_1\hbar}{m} + \left(n_y' + \frac{1}{2}\right)\frac{\alpha_2\beta_2\hbar}{m} \tag{6.15}$$

where n_x', n_y' are integers which label the eigenstate. For comparison with the Darwin-Fock spectrum, Fig. (6.9) shows the first few eigenenergies of an elliptical dot with $\hbar\omega_y = 0.67$ meV, $\hbar\omega_x = 1$ meV. The spectrum is broadly similar to the Darwin-Fock case, with the most obvious difference being that some of the degeneracies at zero field are lifted.

Figure (6.10) shows the experimental data for how the oscillatory tunnelling current behaves in a magnetic field. In the device, the y confinement is provided by the SAW potential whilst the x confinement is provided by the gates. The energy gap corresponding to the side-to-side oscillations discussed in Section (6.8) is therefore $\Delta E = E_{1,0} - E_{0,0}$; these two eigenenergies are indicated with arrows in Fig. (6.9). The dark crescent-shaped features in Fig. (6.10) correspond to voltages where an integer number of oscillations have been performed by the electron along the length of the barrier (this is when the final state is towards the right of the dot and next to the barrier, thereby decreasing the current from the top channel). These crescents therefore map out contours of constant energy gap ΔE.

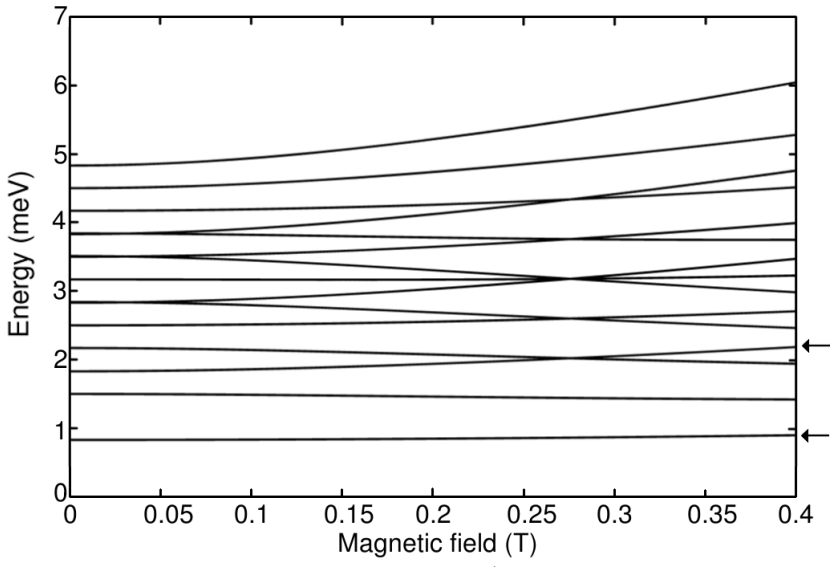

Figure 6.9: Part of the spectrum for an elliptical dot, from Eq. (6.15). Black arrows indicate the states with energy $E_{0,0}$ and $E_{1,0}$ as described in the text.

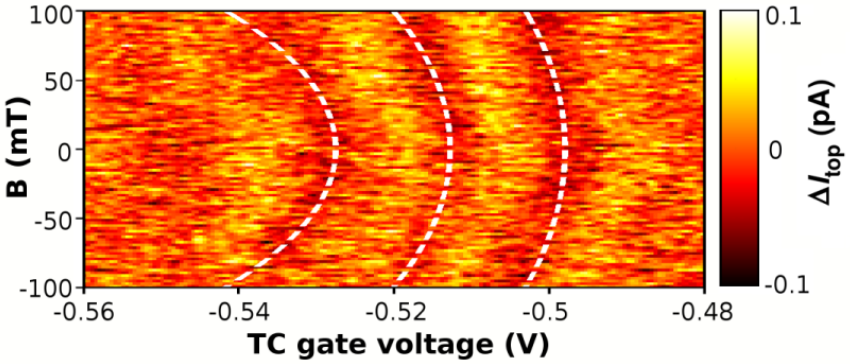

Figure 6.10: Behaviour of oscillations in magnetic field. White dashed lines show the fit from the analytic model described in the text.

In order to compare the experimental data to Eq. (6.15), we assume a sinusoidal SAW potential of amplitude 20 mV [65] and Taylor expand about a SAW minimum to determine that $\hbar\omega_y \simeq 0.67$ meV. We then assume a linear relationship between the TC gate voltage and ω_x. The three dark crescents in Fig. (6.10) correspond to N, $N+1$ and $N+2$ oscillations in the time for which tunnelling can occur. Along with the parameters that relate the TC voltage to ω_x, N and this tunnelling time are used as fitting parameters.

The result of the fit is shown by the white lines superimposed on the data in Fig. (6.10). There is good agreement with the experimental data, and in particular the changing curvature of the different crescents is very well reproduced. The fit suggests that the three dark crescents arise from 8, 9 and 10 oscillations in a time of 43 ps. The magnetic field data therefore provides independent confirmation of the theoretical description in Section (6.8) – for comparison, the simulation in Fig. (6.2c) shows 8 oscillations in 40 ps.

6.10 Choice of potential

It should be noted that one can consider changing the time-dependent potential in a different manner to that discussed earlier, as the time and voltage scales chosen are somewhat arbitrary. For example, rather than having a constant barrier height for the central 40 ps the barrier could change slowly with time, or there may be multiple points where the electron can tunnel from the SAW dot. The simulations presented here deliberately focus on the simplest possible case, but the same qualitative features were found to be reproduced for a range of parameters. One important quantity is the energy difference between the $|0\rangle$ and $|1\rangle$ states, as this sets the oscillation period. For the potentials used here this energy difference is typically $\sim$0.8 meV, but using potentials with energy splittings in the range 0.5–1 meV led to no qualitative difference in the behaviour of the oscillations. The number of oscillations performed is important, however. If many ($\gg 10$) oscillations occur, the visibility of the oscillations is poor as the difference in tunnelling current between performing N and $N+1$ oscillations becomes very small. On the other hand, having only a few oscillations occur requires a tunnelling region which is much shorter than the $\sim$100 nm used here, which is

unlikely in practice. Although the actual tunnelling duration in the experiment may not be 40 ps, this value is reasonable and illustrates the important features of the model. Some other experimental considerations are briefly discussed in the appendix to this chapter.

6.11 Effect of squeezing

The simulations presented to model the experimental data in this chapter assume that the electron was initially in the ground state prior to the nonadiabatic excitation. However, in Chapter 5 we examined the effect of using squeezed and coherent states upon the oscillations discussed in Chapter 4 and found that this could lead to new dynamical behaviour. In Section (6.12) we will investigate the effect of using an initial arbitrary linear combination of the $|0\rangle$ and $|1\rangle$ states. It was seen earlier in this chapter that the $|L\rangle$ and $|R\rangle$ states oscillate from side to side in a similar manner to coherent states, and in this section we will briefly investigate the effect of squeezing the initial wavefunction (i.e., changing its initial width).

In order to introduce squeezing in the simplest way possible, an infinitely high potential barrier was placed at $x = -0.5$ μm when the initial ground state was calculated numerically. In Fig. (6.4) the tunnelling barrier is centered at $x = 0$ and the edge of the TC gate is at $x = -0.4$ μm, so placing a hard barrier at $x = -0.5$ μm should have a fairly small effect on the initial state of the electron. The effect of the hard barrier will be to make the initial wavefunction slightly narrower than the width of the ground state of the potential used in the dynamical simulation. The simulation of Fig. (6.7) was then repeated, and the results are shown in Fig. (6.11). The figure shows the filtered probability Δp of remaining in the SAW dot, with the filtering applied both as a function of TC and barrier voltages (the simulated data shown in Fig. (6.7) was filtered only as a function of TC voltage). The main oscillations from earlier are still visible, but some new features also appear. After filtering as a function of barrier voltage, extra "ripples" can be seen on top of the main oscillations. Similar features were seen in Chapter 5 and were attributed to the introduction of higher-frequency temporal oscillations involving higher eigenstates. Filtering the results as a function of TC

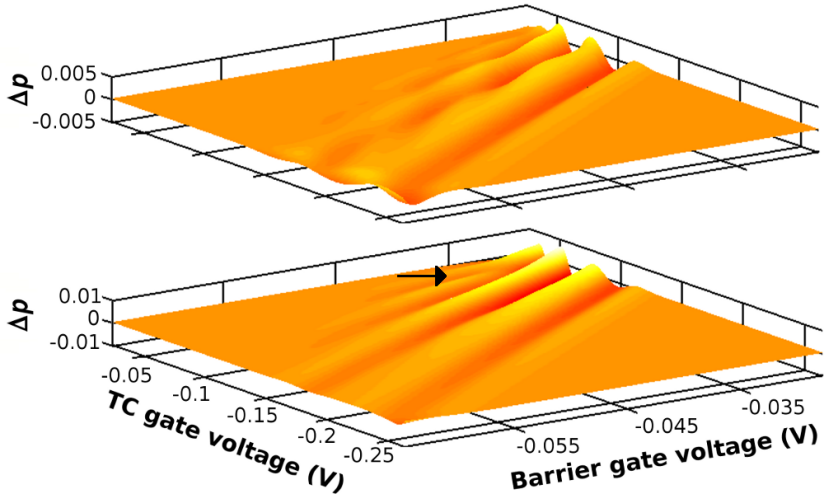

Figure 6.11: Behaviour of oscillations with TC and barrier voltage, showing filtered probability Δp of remaining in the SAW dot. Top: after filtering as a function of barrier voltage. Bottom: after filtering as a function of TC voltage. The arrow indicates the Y-shaped splitting described in the text.

voltage leads to the emergence of a new feature: a Y-shaped splitting around $V_{TC} = -0.05$ V, $V_{bar} = -0.035$ V (indicated by an arrow in the figure) is present.

It should be noted that these features are an order of magnitude smaller than those seen in the simulation in Fig. (6.7). Thus, even if the electron were not initially in the ground state in the experiment, it is unlikely that these features would be experimentally visible given the noise level in the experimental data. The detection of a squeezed initial state in this experiment may therefore require control over the state of the electron prior to the tunnelling region – for example, by using a channel that varies in width (similar to the design shown in Fig. (5.4)). Such an experiment may lead to observation of the distinctive features in Fig. (6.11), and this would be an interesting topic for future measurements.

6.12 Use as a measurement device

In the first part of this chapter, the electron was assumed to be in the ground state at the start of the simulations. The gate voltages defining the tunnelling region were then altered, which led to a set of oscillations in the tunnelling current from

the SAW dot. However, more generally one might want to first perform some unitary transformation on the electron and then measure its state. We will see in this section that the tunnel barrier device could be used in performing such a measurement, as the probability of remaining in the SAW dot after the tunnelling region is strongly dependent upon the initial electron state.

In the simulations that follow, the gate voltages defining the tunnelling region will be fixed and the probability of remaining in the SAW dot after the tunnelling region for different initial states will be calculated. The gate voltages used in these simulations are $V_{bar} = -35$ mV, $V_{TC} = -105$ mV, although we note that the results presented below were found to be qualitatively similar across a range of gate voltages used in the calculation of Fig. (6.6). The initial states $|\psi_i\rangle$ considered here are arbitrary linear combinations of $|0\rangle$ and $|1\rangle$, and so can be parameterised by the Bloch angles θ and ϕ:

$$|\psi_i\rangle = \cos\left(\frac{\theta}{2}\right)|0\rangle + e^{i\phi}\sin\left(\frac{\theta}{2}\right)|1\rangle \tag{6.16}$$

As in Section (6.6), the barrier gate voltage is initially sufficiently negative to suppress tunnelling from the dot. The barrier voltage is then decreased linearly over 10 ps to the final value of -35 mV. The initial barrier gate voltage used previously was -500 mV; changing the barrier gate voltage from this value to -35 mV led to the excitation of nonadiabatic dynamics. Two initial barrier gate voltages will initially be considered here: -225 mV and -400 mV. It will be seen that in the former case the potential change is approximately adiabatic, whilst in the latter the change is nonadiabatic.

Figure (6.12) shows the probability P of remaining in the SAW dot after it has passed the tunnelling region for the approximately adiabatic change in potential. At any fixed value of ϕ, increasing θ from 0 to π decreases $|\langle\psi_i|0\rangle|^2$ whilst $|\langle\psi_i|1\rangle|^2$ increases. This leads to a monotonic decrease in P because $|1\rangle$ is higher in energy than $|0\rangle$ and so has an increased probability of tunnelling from the dot. To understand the behaviour of P as a function of ϕ, we focus on states with $\theta = \pi/2$ for three values of ϕ: $\phi = 0$ ($|\psi\rangle = |0\rangle + |1\rangle$), $\phi = \pi/2$ ($|\psi\rangle = |0\rangle + i|1\rangle$) and $\phi = \pi$ ($|\psi\rangle = |0\rangle - |1\rangle$). The normalisation factor of $1/\sqrt{2}$ is omitted for brevity. The time evolution of the probability density for these

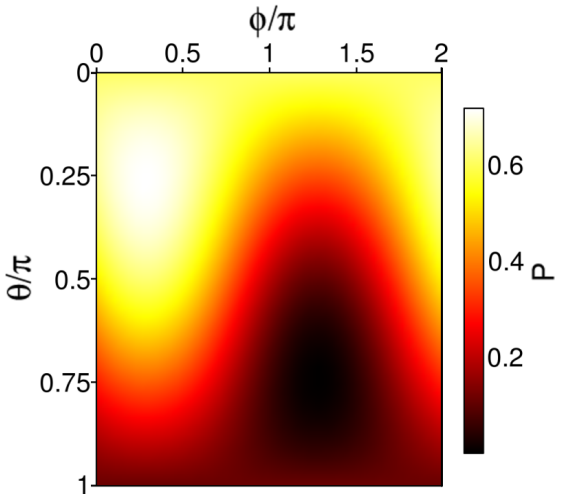

Figure 6.12: Probability P (plotted on the colour scale) of remaining in the SAW dot after the barrier region for different initial states defined by the Bloch angles θ, ϕ for a small (approximately adiabatic) change in the dot potential.

three states is shown in Fig. (6.13). The states with $\phi = 0$ and $\phi = \pi$ oscillate from left to right in the initial 10 ps, performing approximately 2.5 oscillations whilst the barrier height changes. The $\phi = 0$ state is initially displaced towards the right hand side of the dot, and so is at the left side (away from the barrier) when the barrier is low enough to allow tunnelling into the reservoir. This leads to an increased probability of remaining in the dot after the tunnelling region. Conversely, the $\phi = \pi$ state is next to the barrier after the initial 10 ps and so a significant probability weight tunnels out immediately after the initial 10 ps leading to the decrease in P seen in Fig. (6.12) at $\theta = \pi/2$, $\phi = \pi$.

The simulations were repeated with the barrier height changing over 12 ps rather than 10 ps, corresponding to approximately 3 oscillation periods. At the start of the tunnelling region the situation above is thus reversed – the $\phi = 0$ state is next to the barrier and the $\phi = \pi$ state is away from it. The effect of this is to translate the data in Fig. (6.12) by π in the ϕ direction (noting that ϕ is defined modulo 2π); this confirms the above interpretation that the important factor is whether the probability density is situated towards the left or the right of the dot when tunnelling commences.

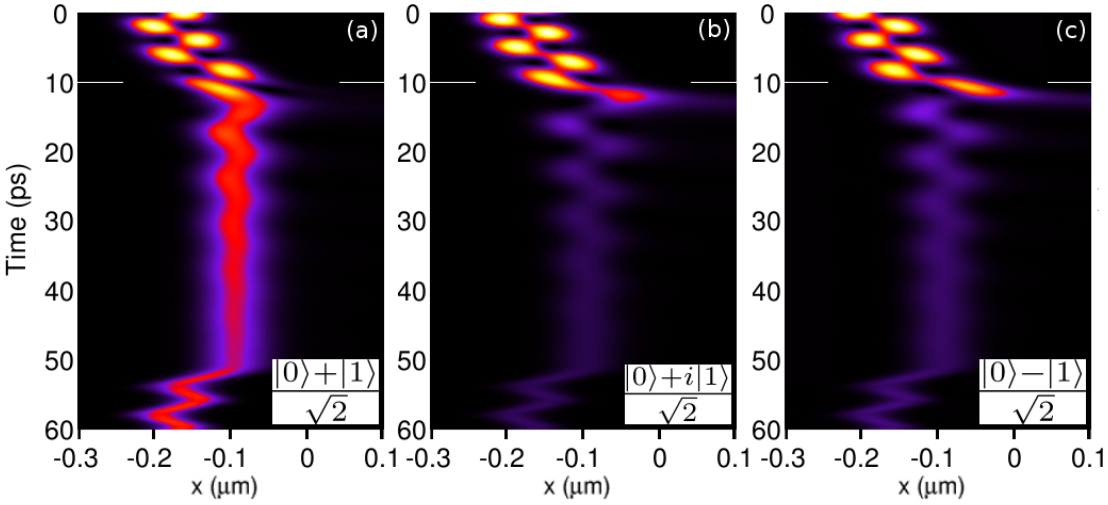

Figure 6.13: Time evolution of the probability density for a small change in barrier height, for three different initial states and a small (approximately adiabatic) change in the dot potential. The initial state is $\theta = \pi/2$ and a) $\phi = 0$, b) $\phi = \pi/2$, c) $\phi = \pi$. The same colour scale is used for all three plots. The white lines show the time at which the barrier height ceases to change.

Next, we consider a large initial barrier gate voltage so the change in potential over the initial 10 ps is nonadiabatic. The resulting behaviour of P is shown in Fig. (6.14), and the time evolution for the three initial states at $\theta = \pi/2$ with $\phi = 0, \pi/2, \pi$ is shown in Fig. (6.15). As before, for the states which are initially displaced from the centre of the dot, approximately 2.5 oscillations are performed in the first 10 ps. An important factor in determining the extent of the nonadiabaticity is the overlap of the electron state with the instantaneous eigenstates at 10 ps. At this time the dot is centered at ~ -0.1 μm, which is to the right of the initial dot position. As the $\phi = \pi$ state is at the right hand side of the dot after 10 ps it has a large overlap with the instantaneous ground state and so is subject to a smaller nonadiabatic excitation. Conversely, the $\phi = 0$ state is at the left side of the dot after 10 ps and so is subject to a much larger nonadiabatic excitation, as is clear from Fig. (6.15a). Increasing the time over which the barrier height changes from 10 to 12 ps again leads to a π translation in the ϕ direction, as discussed earlier.

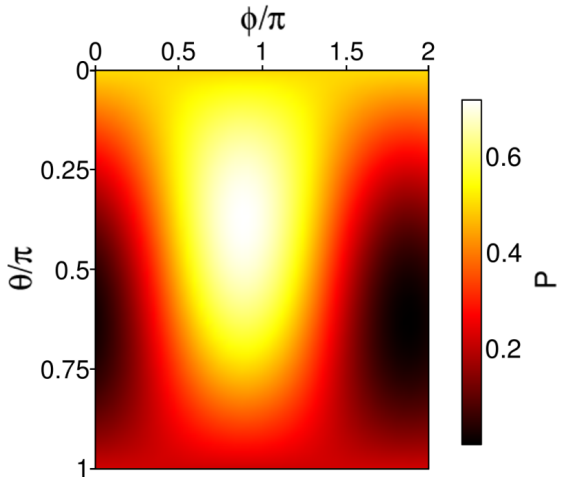

Figure 6.14: Probability P (plotted on the colour scale) of remaining in the SAW dot after the barrier region for different initial states defined by the Bloch angles θ, ϕ for a large (nonadiabatic) change in the dot potential.

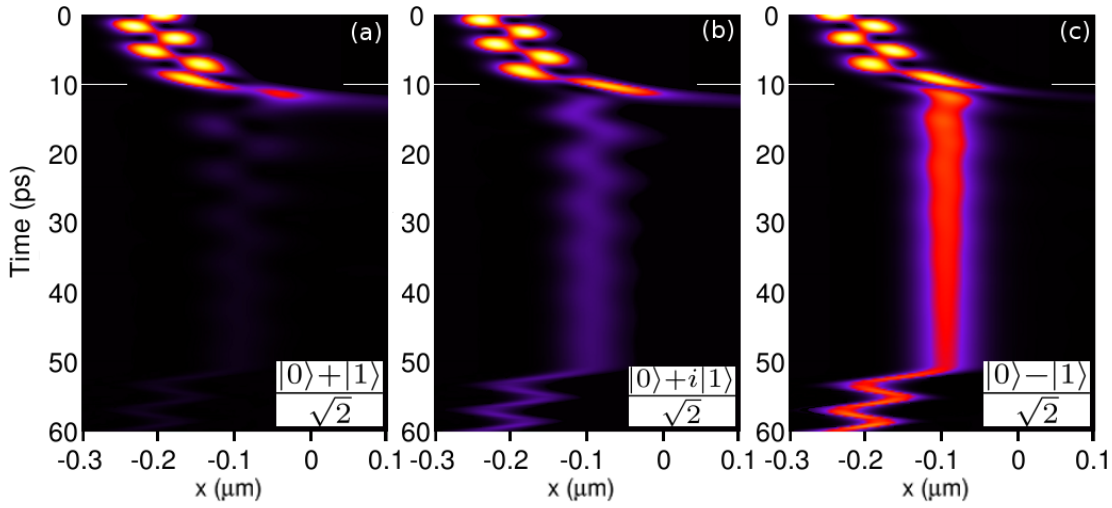

Figure 6.15: Time evolution of the probability density for a small change in barrier height, for three different initial states and a large change in the dot potential. The initial state is $\theta = \pi/2$ and a) $\phi = 0$, b) $\phi = \pi/2$, c) $\phi = \pi$. The same colour scale is used for all three plots. The white lines show the time at which the barrier height ceases to change.

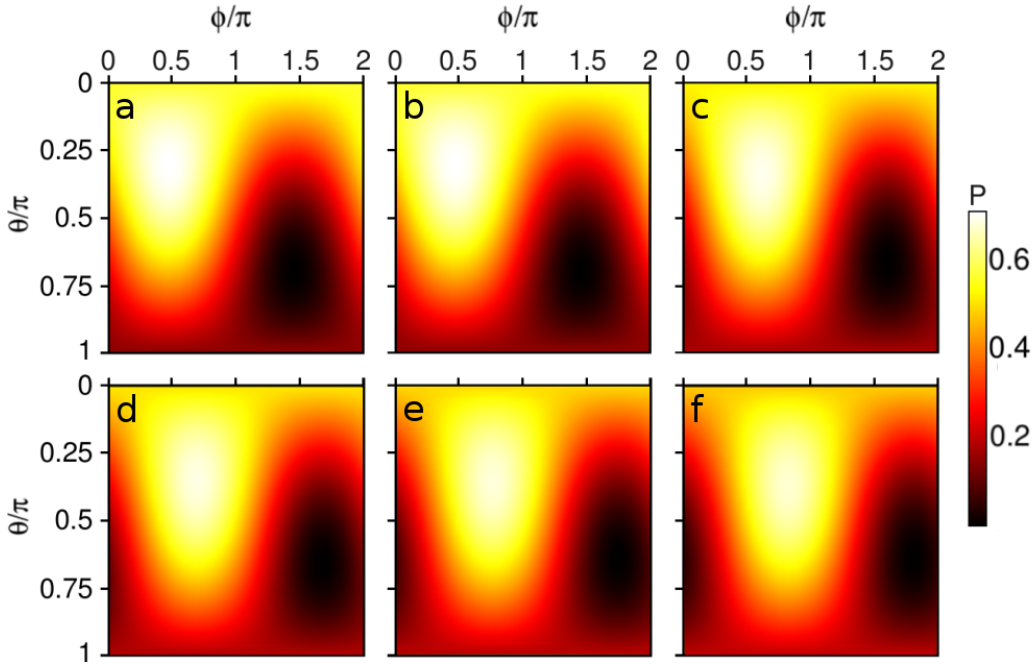

Figure 6.16: Probability P of remaining in the SAW dot for a range of initial barrier gate voltages: a) -250 mV, b) -275 mV, c) -300 mV, d) -325 mV, e) -350 mV, f) -375 mV. A larger initial barrier voltage leads to a more sudden change in the potential.

Finally, Fig. (6.16) shows the behaviour of P for a range of initial barrier gate voltages between the two values discussed above. The figure shows a smooth transition from the approximately adiabatic change in Fig. (6.12) to the strongly nonadiabatic change in Fig. (6.14). The results from an experiment may lie anywhere between these two extremes, and so by comparing experimental results to this sequence of plots it should be possible to gain some knowledge of how adiabatic the change in potential is.

6.13 Conclusions

In this chapter we have proposed a novel technique for producing and probing nonadiabatic dynamics in SAW devices. The motion of the SAW is used to create a rapidly-changing potential in the frame of a SAW-defined dynamic quantum dot; this rapid change in the potential creates an excited state which is displaced

from the centre of the dot. The subsequent dynamical behaviour involves an oscillation from side to side, and if the electron is able to tunnel from one side of the dot into a reservoir this leads to an oscillatory tunnelling probability. Because the tunnelling time is fixed by the device design, changing the frequency of this oscillation leads to an oscillation in the total current which tunnels from the dynamic quantum dot. Data from experimental measurements were presented, and numerical simulations based on the above description were used to explain the measurement results. The dependence of the measured tunnelling current upon the voltages applied to the gates around the tunnelling barrier was reproduced in the simulations, and the behaviour of the measurements in a magnetic field was explained using an analytic result for the spectrum of an elliptical dot.

We then considered how the tunnelling current depends upon the initial state of the electron. Using a wavefunction which had been reduced in width (see also the discussion on squeezed states in Chapter 5) led to the appearance of extra features in the tunnelling current, and it would be interesting to study the controllable creation of such features in a future experiment. Finally, we performed simulations to investigate the effect of using an arbitrary superposition of the lowest two eigenstates as the initial state. It was seen that measuring the tunnelling current gives some information about the initial state of the electron, and the dependence of the tunnelling current on the initial state varied depending upon how sudden the change in the potential was. Such a measurement might therefore be a useful way to determine how rapidly the potential changes in an experimental device.

Appendix: Elimination of other models

Although the model presented in this chapter gives a good qualitative description of the experimental data, one can also consider other possible origins of the observed oscillations. We will now briefly discuss some alternative possibilities and explain why they do not match the data; a full discussion of these effects is presented in Ref. [136].

Quantised states in 1D channel

The density of states in a Q1DC has a sharp peak at the bottom of each subband. Consequently, it may be possible to see a series of peaks in the current from the SAW dot as it passes resonantly past these levels in the neighbouring reservoir. However, the oscillations as a function of TC voltage were found to be highly insensitive to changes in the voltages applied to the three gates defining the bottom channel (BL, BC and BR) (see Fig. 4 of Ref. [136]). This indicates that the source of the oscillations depends only upon the properties of the SAW dot and the barrier, and not upon the properties of the one-dimensional reservoir.

Crosstalk

The current transported in SAW devices is highly sensitive to interference between the SAW wave and any other electromagnetic wave – for example, either reflected SAWs [137] or free-space waves [37] which can modulate the effective voltage applied to surface gates. This is because the process whereby SAWs capture electrons depends critically upon the electric field at a specific point in the channel [62]; the location of this point will change depending upon the relative phase between the SAW and any wave interfering with it. This effect can be eliminated by pulse modulating the signal applied to the SAW transducer [138] and so this interference can be ruled out as a possible origin of the oscillations.

Barrier impurity

The tunnel barrier is not expected to be perfectly smooth; impurities in the barrier region may permit resonant tunnelling when the SAW dot is at particular energies, or the probability of tunnelling through the barrier may be a non-monotonic function of energy. Either of these scenarios could lead to oscillatory behaviour in the tunnelling current. Although it is difficult to completely eliminate these possibilities, it is extremely unlikely that a set of impurities would lead to the four or five approximately periodic oscillations over a wide range of gate voltages seen in Fig. (6.7).

The beginning of knowledge
is the discovery of something
we do not understand.

Frank Herbert

7 Conclusions

The primary goal of this thesis was to use numerical simulations to study methods for the creation and measurement of different types of coherent electron dynamics in surface acoustic wave devices. After summarising the work discussed in this thesis, this chapter will conclude by suggesting some potential avenues for future research.

7.1 Summary of work

The focus of the numerical techniques used throughout this work was to solve the time-dependent Schrödinger equation with a general time-dependent potential. We chose in Chapter 2 to use finite-differencing methods to discretise the spatial part of the Schrödinger equation, and used the Crank-Nicolson method to perform the time evolution. These numerical techniques were then used in Chapter 3 to simulate the transmission of an electron through an Aharonov-Bohm ring. This demonstrated an important property of the numerical techniques we chose to use:

it is straightforward to apply them to devices with an arbitrary geometry, and so the simulations can be used to study effects which are not always included in analytic models. This enabled us to see how the Lorentz force leads to a decreasing AB oscillation amplitude as the magnetic field strength is increased. We also developed a straightforward implementation of absorbing boundary conditions which enabled the emergence of higher-order interference paths to be studied.

In Chapter 4, we studied a device consisting of two parallel SAW channels separated by a narrow tunnelling barrier. The simulations demonstrated that an electron will oscillate between these channels at a frequency which can be controlled with the voltages applied to the gates around the tunnelling region. The oscillation frequency also changed upon the application of a perpendicular magnetic field. An analytic model based upon a two-level system was developed to explain these results; the two basis states used are each localised to one of the two SAW channels. A perpendicular magnetic field was included in the model via the infinitesimal Aharonov-Bohm effect. The model then allowed the effect of a transverse electric field in combination with a perpendicular magnetic field to be calculated. Finally, it was shown that it is possible to create an arbitrary superposition of the two basis states by using a geometry similar to that of a Mach-Zehnder interferometer. The results of this chapter are potentially of use in SAW-based QIP schemes – the two-channel device could be used as a single charge qubit or two spin qubits. In the former case the results from this chapter directly describe single-qubit rotations. In the latter case a two-qubit operation could be performed using the device we discussed; understanding the two-qubit operation requires an understanding of how to control the oscillation frequency of a single electron.

Chapter 5 introduced coherent and squeezed states, which are two classes of excited state in a harmonic oscillator described by a Gaussian wavefunction. Coherent states have the same standard deviation as the ground state of a harmonic potential, but they are displaced away from the centre of the potential. Conversely, squeezed states are located at the centre of the potential but have a standard deviation which differs from that of the ground state. Coherent and squeezed light states have been the subject of much study in quantum optics, and we then saw that electronic coherent states could be a useful resource in

QIP. They can also be used to understand some of the effects that unwanted perturbations may have upon an electron carried by a SAW. This motivated an investigation of how to create coherent states in a SAW device, which can be achieved by suddenly changing the potential which the electron experiences. The amplitude of the SAW is an important factor, because if the SAW amplitude is too large the electron adiabatically remains in the instantaneous ground state. The velocity of the electron can change when a SAW of sufficiently low amplitude encounters a sloped potential; this leads to a more rapid change in the potential in the frame of the electron and thus to excitation out of the ground state. We then simulated the effect of using coherent and squeezed states in the two-channel device studied in the previous chapter. That chapter showed how the current flowing from the two channels depends upon the voltages applied to gates around a tunnelling barrier; using a coherent or squeezed state modifies these currents, and this might be a useful way to detect the creation of such states.

Chapter 6 presented a technique for creating and measuring states which oscillate from side to side in a dynamic quantum dot. These states can be created by using the motion of a SAW to create a rapidly (i.e., nonadiabatic) changing potential in the frame of the dot, and the tunnelling current through a barrier next to the dot is then used to probe this motion. An experimental device which is able to test these ideas was first described and then used as the basis for numerical simulations. Good agreement was seen between the simulations and measured data; the simulations then led to an explanation of how the measured data reflected changes in the properties of the dynamic dot as a function of gate voltages and perpendicular magnetic field. We then calculated how the tunnelling current changes when an arbitrary superposition of the first two eigenstates is used as the initial state. It was found that measuring the tunnelling current provides information about both the initial state of the electron and how rapid the change in potential was, and this could be of use in determining under what conditions a nonadiabatic quantum transition occurs.

7.2 Future work

7.2.1 Aharonov-Bohm rings

An important property of the techniques that were used to study transmission through an Aharonov-Bohm ring in Chapter 3 was that they can be easily adapted to more complicated potentials. Kvon *et al.* [95] suggested that disorder in AB rings could lead to the suppression of some interference effects arising from multiple trajectories around the ring. Randomly ionised donors are a significant source of disorder in semiconductor devices, and the results from a calculation of disorder such as those performed by Stopa [139, 140] could be incorporated into the AB ring simulations performed in this thesis.

7.2.2 Two-channel oscillations

Chapter 4 investigated the coherent oscillation of an electron in a two-channel SAW device. The parameters governing charge oscillation also relate to a two-qubit operation using spin qubits [40], and as spin coherence times in GaAs are generally much greater than charge coherence times it is likely that spin manipulation will be the subject of future experimental work. It would therefore be useful to extend the simulations of electron charge in a SAW to also include the spin degree of freedom. It is in principle straightforward to include a Zeeman term in the finite-differenced Hamiltonian, but this leads to a significant increase in the computational resources required and so would require further work.

An alternative method to coherently transfer a quantum particle from one potential well to another has been proposed by Greentree *et al.* [141], which they label "coherent transfer by adiabatic passage" (CTAP). The proposal uses three quantum dots, each of which has a single accessible state labelled $|1\rangle$, $|2\rangle$, $|3\rangle$. The dots are separated by controllable tunnelling barriers as shown in Fig. (7.1). It is shown in Ref. [141] that it is possible to completely transfer the initial state $|1\rangle$ to state $|3\rangle$ with no probability of occupying state $|2\rangle$ in the central dot. This is achieved through a counter-intuitive sequence of changing the interdot couplings with time: a pulse to lower the barrier between dots 2 and 3 is applied, followed

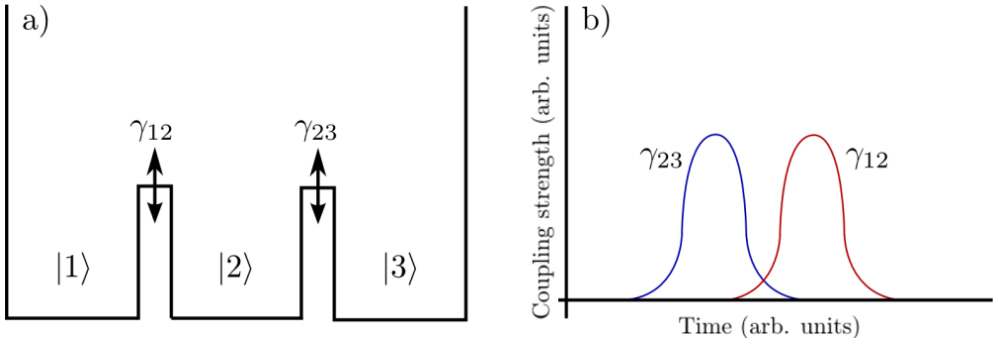

Figure 7.1: Illustration of system and pulse sequence for CTAP. a) Three dots each have a single accessible level $|i\rangle$ ($i = 1 \ldots 3$) and are separated by controllable barriers. b) Counter-intuitive pulse sequence required for CTAP. The coupling between dots 2 and 3 is switched on first (blue curve), followed by the coupling between dots 1 and 2 (red curve).

by a pulse to lower the barrier between dots 1 and 2. This leads to a highly robust transfer from state $|1\rangle$ to $|3\rangle$, whereas if the pulses are applied in the intuitive order complete transfer from $|1\rangle$ to $|3\rangle$ is only possible if the pulses are very carefully chosen. It should be possible to achieve such a time-varying potential with a SAW device consisting of three channels separated by narrow controllable barriers, and the simulations developed in Chapter 4 could be extended to aid in designing such a device. CTAP could then potentially be a useful method to controllably and coherently transfer electrons between different SAW channels.

7.2.3 Coherent and squeezed states

It was proposed in Chapter 5 that the generation of coherent and squeezed states could be achievable in a SAW device. An interesting theoretical goal would be to study potential uses of electronic coherent and squeezed states in more detail, to fully determine what analogies can be drawn with the well-established field of quantum optics. Although the controllable generation of these states was discussed, part of the motivation for studying coherent and squeezed states was that they could arise in an experiment due to unwanted perturbations. As discussed in Section (7.2.1), a realistic disordered potential could be incorporated

into the numerical simulations performed in this thesis which would then allow the effect of some unwanted perturbations to be investigated.

7.2.4 Nonadiabatic dynamics

It was suggested in Chapter 6 that the tunnel barrier device could be used as a measurement apparatus to measure the state of an incoming electron. An interesting future experiment would be to design a device which can controllably inject a single electron in an arbitrary state and then measure it with a tunnel barrier. As this would be experimentally challenging, a worthwhile starting point would be to restrict the desired set of initial states to those which are controllably displaced from the centre of the entrance channel. This would require a simpler gate design than that needed to prepare an arbitrary initial state, and the results from simulations similar to those performed in Chapter 6 would allow interpretation of the measured results.

The tunnel barrier device could also be used to study the interaction between two nonadiabatically-excited electrons. As well as being an interesting study of fundamental quantum mechanical behaviour, such interactions might have application in quantum information processing. A possible device to study this is shown schematically in Fig. (7.2), and would consist of two parallel channels each of which generates the side-to-side oscillating state discussed in Chapter 6. The channels would then be separated by a controllable barrier which allows the interaction between the electrons to be changed. After the interaction region each channel would then need to couple to a reservoir in order to be measured using the method outlined in Section (6.12). Although the work in this thesis focussed on single-electron dynamics, Giavaras *et al.* [142] numerically simulated in 1D the interaction between an electron carried in a SAW minimum and an electron trapped in a static quantum dot. It should be possible to adapt the method used there to study the two-electron interaction discussed above.

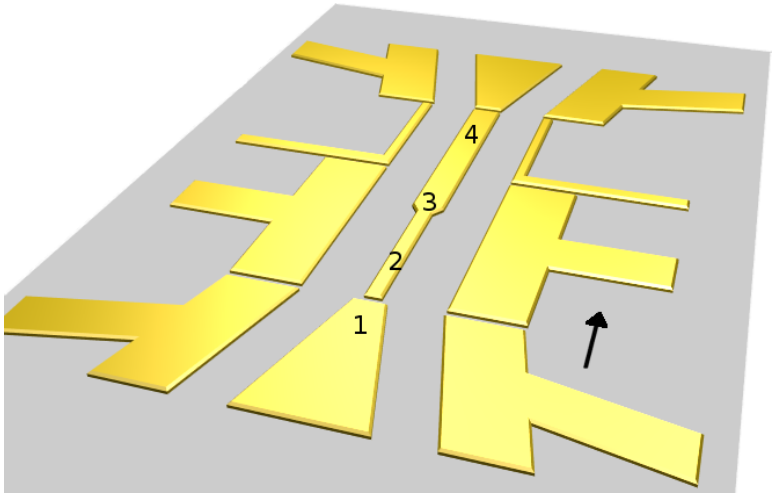

Figure 7.2: Schematic illustration of device to probe electron-electron interaction. The arrow indicates the direction of SAW motion. 1) Two neighbouring electrons are brought together. 2) The electrons interact via a direct Coulomb interaction. 3) The barrier between the two channels is raised to halt the interaction. 4) Each electron passes a tunnel barrier which allows measurement.

References

[1] A. M. Turing. "On computable numbers, with an application to the Entscheidungsproblem". *Proceedings of the London Mathematical Society Series* **2**, 230 (1936)

[2] R. L. Rivest, A. Shamir & L. Adleman. "A method for obtaining digital signatures and public-key cryptosystems". *Communications of the ACM* **21**, 120 (1978)

[3] R. P. Feynman. "Quantum mechanical computers". *Opt. News* **11**, 11 (1985)

[4] D. Deutsch. "Quantum theory, the Church-Turing principle and the universal quantum computer". *Proc. Roy. Soc. A* **400**, 97 (1985)

[5] P. W. Shor. "Polynomial time algorithms for prime factorization and discrete logarithms on a quantum computer". *SIAM J. Sci. Statist. Comput.* **26**, 1484 (1997)

[6] L. K. Grover. "A fast quantum mechanical algorithm for database search". In *Proceedings of the 28th annual ACM symposium on Theory of computing*, pages 212–219. ACM New York, NY, USA (1996)

[7] D. P. DiVincenzo. "The Physical Implementation of Quantum Computation". *Fortschritte der Physik* **48**, 771 (2000)

[8] M. A. Nielsen & I. L. Chuang. *Quantum computation and quantum information*. Cambridge University Press (2000)

[9] A. Messiah. *Quantum Mechanics (Volume 2).* North-Holland Publishing Company (1962)

[10] E. Farhi, J. Goldstone, S. Gutmann, J. Lapan, A. Lundgren & D. Preda. "A Quantum Adiabatic Evolution Algorithm Applied to Random Instances of an NP-Complete Problem". *Science* **292**, 472 (2001)

[11] D. Aharonov, W. van Dam, J. Kempe, Z. Landau, S. Lloyd & O. Regev. "Adiabatic Quantum Computation is Equivalent to Standard Quantum Computation". *Arxiv preprint quant-ph/0405098* (2004)

[12] M. Steffen, W. van Dam, T. Hogg, G. Breyta & I. Chuang. "Experimental implementation of an adiabatic quantum optimization algorithm". *Phys. Rev. Lett.* **90**, 067903 (2003)

[13] X. Peng, J. Du & D. Suter. "Quantum phase transition of ground-state entanglement in a Heisenberg spin chain simulated in an NMR quantum computer". *Phys. Rev. A* **71**, 012307 (2005)

[14] A. Mitra, A. Ghosh, R. Das, A. Patel & A. Kumar. "Experimental implementation of local adiabatic evolution algorithms by an NMR quantum information processor". *Journal of Magnetic Resonance* **177**, 285 (2005)

[15] X. Peng, Z. Liao, N. Xu, G. Qin, X. Zhou, D. Suter & J. Du. "Quantum adiabatic algorithm for factorization and its experimental implementation". *Phys. Rev. Lett.* **101**, 220405 (2008)

[16] P. Zanardi & M. Rasetti. "Holonomic quantum computation". *Physics Letters A* **264**, 94 (1999)

[17] F. Wilczek & A. Zee. "Appearance of gauge structure in simple dynamical systems". *Phys. Rev. Lett.* **52**, 2111 (1984)

[18] E. L. Hahn. "Spin echoes". *Phys. Rev.* **80**, 580 (1950)

[19] J. Jones, V. Vedral, A. Ekert & G. Castagnoli. "Geometric quantum computation using nuclear magnetic resonance". *Nature* **403**, 869 (2000)

[20] R. G. Unanyan, B. W. Shore & K. Bergmann. "Laser-driven population transfer in four-level atoms: Consequences of non-abelian geometrical adiabatic phase factors". *Phys. Rev. A* **59**, 2910 (1999)

[21] L.-M. Duan, J. I. Cirac & P. Zoller. "Geometric Manipulation of Trapped Ions for Quantum Computation". *Science* **292**, 1695 (2001)

[22] L. Faoro, J. Siewert & R. Fazio. "Non-abelian holonomies, charge pumping, and quantum computation with josephson junctions". *Phys. Rev. Lett.* **90**, 028301 (2003)

[23] P. Solinas, P. Zanardi, N. Zanghì & F. Rossi. "Semiconductor-based geometrical quantum gates". *Phys. Rev. B* **67**, 121307 (2003)

[24] E. Sjöqvist. "A new phase in quantum computation". *Physics* **1**, 35 (2008)

[25] J. Nielsen. *Niels Bohr. Collected Works. Vol. 3. The Correspondence Principle (1918–1923).* North-Holland, Amsterdam (1976)

[26] V. B. Braginsky & F. Y. Khalili. "Quantum nondemolition measurements: the route from toys to tools". *Rev. Mod. Phys.* **68**, 1 (1996)

[27] Y. Aharonov, D. Z. Albert & L. Vaidman. "How the result of a measurement of a component of the spin of a spin-1/2 particle can turn out to be 100". *Phys. Rev. Lett.* **60**, 1351 (1988)

[28] T. Bhattacharya, S. Habib & K. Jacobs. "Quantum Physics Title: The Emergence of Classical Dynamics in a Quantum World". *Arxiv preprint quant-ph/0407096v1* (2002)

[29] D. G. Cory, M. D. Price, W. Maas, E. Knill, R. Laflamme, W. H. Zurek, T. F. Havel & S. S. Somaroo. "Experimental quantum error correction". *Phys. Rev. Lett.* **81**, 2152 (1998)

[30] E. Knill, I. Chuang & R. Laflamme. "Effective pure states for bulk quantum computation". *Phys. Rev. A* **57**, 3348 (1998)

[31] J. J. Cirac & P. Zoller. "Quantum computations with cold trapped ions". *Phys. Rev. Lett.* **74**, 4091 (1995)

[32] M. H. Devoret, A. Wallraff & J. M. Martinis. "Superconducting qubits: A short review". *Arxiv preprint cond-mat/0411174* (2004)

[33] D. Loss & D. P. DiVincenzo. "Quantum computation with quantum dots". *Phys. Rev. A* **57**, 120 (1998)

[34] A. Galindo & M. A. Martin-Delgado. "Information and computation: Classical and quantum aspects". *Rev. Mod. Phys.* **74**, 11 (2002)

[35] S. Adachi. "GaAs, AlAs, and AlGaAs: Material parameters for use in research and device applications". *Journal of Applied Physics* **58**, R1 (1985)

[36] Lord Rayleigh. "On Waves Propagated along the Plane Surface of an Elastic Solid". *Proceedings of the London Mathematical Society* **1**, 4 (1885)

[37] J. M. Shilton, V. I. Talyanskii, M. Pepper, D. A. Ritchie, J. E. F. Frost, C. J. B. Ford, C. G. Smith & G. A. C. Jones. "High-frequency single-electron transport in a quasi-one-dimensional gaas channel induced by surface acoustic waves". *J. Phys. Condens. Matter* **8**, L531 (1996)

[38] V. I. Talyanskii, J. M. Shilton, C. G. Pepper, M. Smith, C. J. B. Ford, E. H. Linfield, D. A. Ritchie & G. A. C. Jones. "Single-electron transport in a one-dimensional channel by high-frequency surface acoustic waves". *Phys. Rev. B* **56**, 23 (1997)

[39] T. J. B. M. Janssen & A. Hartland. "Accuracy of quantized single-electron current in a one-dimensional channel". *Physica B* **284**, 1790 (2000)

[40] C. H. W. Barnes, J. M. Shilton & A. M. Robinson. "Quantum computation using electrons trapped by surface acoustic waves". *Phys. Rev. B* **62**, 8410 (2000)

[41] R. J. Schneble, R. P. G. McNeil, M. Kataoka, T. Kasama, R. E. Dunin-Borkowski, J. M. Feinberg, R. J. Harrison, C. J. B. Ford, C. H. W. Barnes, D. H. Y. Tse, T. Trypiniotis, J. A. C. Bland, D. Anderson, G. A. C. Jones &

M. Pepper. "Localised magnetic fields in arbitrary directions using pattened nanomagnets". *To be submitted* (2008)

[42] C. L. Foden, V. I. Talyanskii, G. J. Milburn, M. L. Leadbeater & M. Pepper. "High-frequency acousto-electric single-photon source". *Phys. Rev. A* **62**, 011803 (2000)

[43] J. R. Gell, M. B. Ward, A. J. Shields, P. Atkinson, S. P. Bremner, D. Anderson, M. Kataoka, C. H. W. Barnes, G. A. C. Jones & D. A. Ritchie. "Temporal characteristics of surface-acoustic-wave-driven luminescence from a lateral pn junction". *Appl. Phys. Lett.* **91**, 013506 (2007)

[44] J. M. Elzerman, R. Hanson, L. H. W. van Beveren, B. Witkamp & L. P. Kouwenhoven. "Single-shot read-out of an individual electron spin in a quantum dot". *Nature* **430**, 431 (2004)

[45] M. Field, C. G. Smith, M. Pepper, K. M. Brown, E. H. Linfield, M. P. Grimshaw, D. A. Ritchie & G. A. C. Jones. "Non-invasive detection of single-electron processes". *Semiconductor Science and Technology* **11**, 1498 (1996)

[46] T. Hayashi, T. Fujisawa, H. D. Cheong, Y. H. Jeong & Y. Hirayama. "Coherent manipulation of electronic states in a double quantum dot". *Phys. Rev. Lett.* **91**, 226804 (2003)

[47] J. Gorman, D. G. Hasko & D. A. Williams. "Charge-qubit operation of an isolated double quantum dot". *Phys. Rev. Lett.* **95**, 090502 (2005)

[48] Y. Nakamura, Y. A. Pashkin & J. S. Tsai. "Coherent control of macroscopic quantum states in a single-Cooper-pair box". *Nature* **398**, 786 (1999)

[49] J. H. Plantenberg, P. C. de Groot, C. J. P. M. Harmans & J. E. Mooij. "Demonstration of controlled-not quantum gates on a pair of superconducting quantum bits". *Nature* **447**, 836 (2007)

[50] P. Bordone, A. Bertoni, M. Rosini, S. Reggiani & C. Jacoboni. "Coherent transport in coupled quantum wires assisted by surface acoustic waves". *Semiconductor Science and Technology* **19**, S412 (2004)

[51] The Condor high-throughput computing project. http://www.cs.wisc.edu/condor (2009)

[52] M. Kataoka, M. R. Astley, A. L. Thorn, D. K. L. Oi, C. H. W. Barnes, C. J. B. Ford, D. Anderson, G. A. C. Jones, I. Farrer, D. A. Ritchie & M. Pepper. "Coherent time evolution of a single-electron wave function" (2009). To be published in Phys. Rev. Lett.

[53] J. von Neumann & H. H. Goldstine. "Numerical inverting of matrices of high order". *Bull. Amer. Math. Soc.* **53**, 1021 (1947)

[54] W. F. Ames. *Numerical Methods for Partial Differential Equations.* New York Academic Press (1977)

[55] W. H. Press, S. A. Teukolsky, W. T. Vetterling & B. P. Flannery. *Numerical Recipes in C++: The Art of Scientific Computing.* Cambridge University Press (2002)

[56] J. Crank & P. Nicolson. "A practical method for numerical evaluation of solutions of partial differential equations of the heat-conduction type". *Proc. Cambridge Philos. Soc.* **43**, 50 (1947)

[57] D. R. Hofstadter. "Energy levels and wave functions of Bloch electrons in rational and irrational magnetic fields". *Phys. Rev. B* **14**, 2239 (1976)

[58] S. Rahman, M. Kataoka, C. H. W. Barnes & H. P. Langtangen. "Numerical investigation of a piezoelectric surface acoustic wave interaction with a one-dimensional channel". *Phys. Rev. B* **74**, 035308 (2006)

[59] J. H. Davies, I. A. Larkin & E. V. Sukhorukov. "Modeling the patterned two-dimensional electron gas: Electrostatics". *Journal of Applied Physics* **77**, 4504 (1995)

[60] G. H. Meisters. "Polygons have ears". *Amer. Math. Monthly* **82**, 648 (1975)

[61] G. R. Aizin, G. Gumbs & M. Pepper. "Screening of the surface-acoustic-wave potential by a metal gate and the quantization of the acoustoelectric current in a narrow channel". *Phys. Rev. B* **58**, 10589 (1998)

[62] A. M. Robinson & C. H. W. Barnes. "Classical dynamics of electrons in quantized-acoustoelectric-current devices". *Phys. Rev. B* **63**, 165418 (2001)

[63] P. A. Maksym. "Quantized electron transport through a time-dependent potential barrier". *Phys. Rev. B* **61**, 4727 (2000)

[64] G. Gumbs, G. R. Aizin & M. Pepper. "Coulomb interaction of two electrons in the quantum dot formed by the surface acoustic wave in a narrow channel". *Phys. Rev. B* **60**, R13954 (1999)

[65] R. J. Schneble, M. Kataoka, C. J. B. Ford, C. H. W. Barnes, D. Anderson, G. A. C. Jones, I. Farrer, D. A. Ritchie & M. Pepper. "Quantum-dot thermometry of electron heating by surface acoustic waves". *Appl. Phys. Lett.* **89**, 122104 (2006)

[66] M. R. Astley, M. Kataoka, C. J. B. Ford, C. H. W. Barnes, D. Anderson, G. A. C. Jones, I. Farrer, D. A. Ritchie & M. Pepper. "Energy-Dependent Tunneling from Few-Electron Dynamic Quantum Dots". *Phys. Rev. Lett.* **99**, 156802 (2007)

[67] H. P. Langtangen. *Computational Partial Differential Equations: Numerical Methods and Diffpack Programming*. Springer (2003)

[68] N. Watanabe & M. Tsukada. "Finite element approach for simulating quantum electron dynamics in a magnetic field". *Journal of the Physical Society of Japan* **69**, 2962 (2000)

[69] T. Iitaka. "Solving the time-dependent Schrödinger equation numerically". *Phys. Rev. E* **49**, 4684 (1994)

[70] J. C. Butcher. *The numerical analysis of ordinary differential equations: Runge-Kutta and general linear methods*. Wiley-Interscience New York, NY, USA (1987)

[71] P. A. Maksym (2009). Private communication

[72] C. Leforestier, R. H. Bisseling, C. Cerjan, M. D. Feit, R. Friesner, A. Guldberg, A. Hammerich, G. Jolicard, W. Karrlein, H. D. Meyer, N. Lipkin,

O. Roncero & R. Kosloff. "A comparison of different propagation schemes for the time dependent Schrödinger equation". *Journal of Computational Physics* **94**, 59 (1991)

[73] Y. Aharonov & D. Bohm. "Significance of electromagnetic potentials in the quantum theory". *Phys. Rev.* **115**, 485 (1959)

[74] A. E. Hansen, A. Kristensen, S. Pedersen, C. B. Sørensen & P. E. Lindelof. "Mesoscopic decoherence in Aharonov-Bohm rings". *Phys. Rev. B* **64**, 045327 (2001)

[75] R. G. Chambers. "Shift of an electron interference pattern by enclosed magnetic flux". *Phys. Rev. Lett.* **5**, 3 (1960)

[76] R. A. Webb, S. Washburn, C. P. Umbach & R. B. Laibowitz. "Observation of h/e Aharonov-Bohm Oscillations in Normal-Metal Rings". *Phys. Rev. Lett.* **54**, 2696 (1985)

[77] G. Timp, A. M. Chang, J. E. Cunningham, T. Y. Chang, P. Mankiewich, R. Behringer & R. E. Howard. "Observation of the Aharonov-Bohm effect for $\omega_c t > 1$". *Phys. Rev. Lett.* **58**, 2814 (1987)

[78] C. J. B. Ford, T. J. Thornton, R. Newbury, M. Pepper & H. Ahmed. "Electrostatically defined heterojunction rings and the Aharonov-Bohm effect". *Appl. Phys. Lett.* **54**, 21 (1989)

[79] M. Kataoka, C. Ford, G. Faini, D. Mailly, M. Simmons, D. Mace, C. Liang & D. Ritchie. "Detection of Coulomb Charging around an Antidot in the Quantum Hall Regime". *Phys. Rev. Lett.* **83**, 160 (1999)

[80] J. Cao, Q. Wang, M. Rolandi & H. Dai. "Aharonov-Bohm Interference and Beating in Single-Walled Carbon-Nanotube Interferometers". *Phys. Rev. Lett.* **93**, 216803 (2004)

[81] E. Buks, R. Schuster, M. Heiblum, D. Mahalu & V. Umansky. "Dephasing in electron interference by a which-path detector". *Nature* **391**, 871 (1998)

[82] M. Field, C. G. Smith, M. Pepper, D. A. Ritchie, J. E. F. Frost, G. A. C. Jones & D. G. Hasko. "Measurements of Coulomb blockade with a noninvasive voltage probe". *Phys. Rev. Lett.* **70**, 1311 (1993)

[83] D. Chang, G. Khym, K. Kang, Y. Chung, H. Lee, M. Seo, M. Heiblum, D. Mahalu & V. Umansky. "Quantum mechanical complementarity probed in a closed-loop Aharonov–Bohm interferometer". *Nature Physics* **4**, 205 (2008)

[84] M. Büttiker, Y. Imry & M. Y. Azbel. "Quantum oscillations in one-dimensional normal-metal rings". *Phys. Rev. A* **30**, 1982 (1984)

[85] P. Vasilopoulos, O. Kálmán, F. M. Peeters & M. G. Benedict. "Aharonov-Bohm oscillations in a mesoscopic ring with asymmetric arm-dependent injection". *Phys. Rev. B* **75**, 35304 (2007)

[86] B. Szafran & F. M. Peeters. "Time-dependent simulations of electron transport through a quantum ring: Effect of the Lorentz force". *Phys. Rev. B* **72**, 165301 (2005)

[87] B. Szafran & F. M. Peeters. "Lorentz-force-induced asymmetry in the Aharonov-Bohm effect in a three-terminal semiconductor quantum ring". *Europhysics Letters* **70**, 810 (2005)

[88] W. R. Frensley. "Boundary conditions for open quantum systems driven far from equilibrium". *Rev. Mod. Phys.* **62**, 745 (1990)

[89] T. Shibata. "Absorbing boundary conditions for the finite-difference time-domain calculation of the one-dimensional Schrödinger equation". *Phys. Rev. B* **43**, 6760 (1991)

[90] J.-P. Kuska. "Absorbing boundary conditions for the Schrödinger equation on finite intervals". *Phys. Rev. B* **46**, 5000 (1992)

[91] S. J. Wright. Private communication (2008)

[92] J.-B. Yau, E. P. De Poortere & M. Shayegan. "Aharonov-Bohm Oscillations with Spin: Evidence for Berry's Phase". *Phys. Rev. Lett.* **88**, 146801 (2002)

[93] J. Liu, W. X. Gao, K. Ismail, K. Y. Lee, J. M. Hong & S. Washburn. "Correlations between Aharonov-Bohm effects and one-dimensional subband populations in GaAs/$Al_xGa_{1-x}As$ rings". *Phys. Rev. B* **48**, 15148 (1993)

[94] W. C. Tan & J. C. Inkson. "Landau quantization and the Aharonov-Bohm effect in a two-dimensional ring". *Phys. Rev. B* **53**, 6947 (1996)

[95] Z. Kvon, D. Kozlov, E. Olshanetsky, A. Plotnikov, A. Latyshev & J. Portal. "Ultra-high Aharonov–Bohm oscillations harmonics in a small ring interferometer". *Solid State Communications* **147**, 230 (2008)

[96] J. Anandan. "Quantum interference and the classical limit". *International Journal of Theoretical Physics* **19**, 537 (1980)

[97] M. O. Scully & M. Suhail Zubairy. *Quantum Optics*. Cambridge University Press (1997)

[98] Y. Ji, Y. Chung, D. Sprinzak, M. Heiblum, D. Mahalu & H. Shtrikman. "An electronic Mach-Zehnder interferometer." *Nature* **422**, 415 (2003)

[99] I. Neder, N. Ofek, Y. Chung, M. Heiblum, D. Mahalu & V. Umansky. "Interference between two indistinguishable electrons from independent sources". *Nature* **448**, 333 (2007)

[100] R. Rodriquez, D. K. L. Oi, M. Kataoka, C. H. W. Barnes, T. Ohshima & A. K. Ekert. "Surface-acoustic-wave single-electron interferometry". *Phys. Rev. B* **72**, 85329 (2005)

[101] D. J. Tannor. *Introduction to Quantum Mechanics: A time-dependent perspective*. University Science Books (2007)

[102] E. Schrödinger. "Der stetige Übergang von der Mikro- zur Makromechanik". *Naturwissenschaften* **14**, 664 (1926)

[103] A. Messiah. *Quantum Mechanics (Volume 1)*. North-Holland Publishing Company (1961)

[104] R. J. Glauber. "Coherent and incoherent states of the radiation field". *Phys. Rev.* **131**, 2766 (1963)

[105] L. Mandel & E. Wolf. *Optical Coherence and Quantum Optics*. Cambridge University Press (1995)

[106] D. Walls & G. Milburn. *Quantum Optics*. Springer Verlag (2006)

[107] T. C. Ralph, A. Gilchrist, G. J. Milburn, W. J. Munro & S. Glancy. "Quantum computation with optical coherent states". *Phys. Rev. A* **68**, 042319 (2003)

[108] A. P. Lund, T. C. Ralph & H. L. Haselgrove. "Fault-tolerant linear optical quantum computing with small-amplitude coherent states". *Phys. Rev. Lett.* **100**, 030503 (2008)

[109] D. F. Walls. "Squeezed states of light". *Nature* **306**, 141 (1983)

[110] J. Rai & C. L. Mehta. "Coordinate representation of squeezed states". *Phys. Rev. A* **37**, 4497 (1988)

[111] D. Gottesman, A. Kitaev & J. Preskill. "Encoding a qubit in an oscillator". *Phys. Rev. A* **64**, 012310 (2001)

[112] C. M. Caves. "Quantum-mechanical radiation-pressure fluctuations in an interferometer". *Phys. Rev. Lett.* **45**, 75 (1980)

[113] A. F. Pace, M. J. Collett & D. F. Walls. "Quantum limits in interferometric detection of gravitational radiation". *Phys. Rev. A* **47**, 3173 (1993)

[114] M. Xiao, L.-A. Wu & H. J. Kimble. "Precision measurement beyond the shot-noise limit". *Phys. Rev. Lett.* **59**, 278 (1987)

[115] Agata M. Brańczyk and T. C. Ralph. "Teleportation using squeezed single photons". *Phys. Rev. A* **78**, 052304 (2008)

[116] P. Horowitz & W. Hill. *The Art of Electronics*. Cambridge University Press (1989)

[117] S. Rahman, T. M. Stace, H. P. Langtangen, M. Kataoka & C. H. W. Barnes. "Pulse-induced acoustoelectric vibrations in surface-gated GaAs-based quantum devices". *Phys. Rev. B* **75**, 205303 (2007)

[118] D. M. Tong, K. Singh, L. C. Kwek & C. H. Oh. "Quantitative conditions do not guarantee the validity of the adiabatic approximation". *Phys. Rev. Lett.* **95**, 110407 (2005)

[119] K. P. Marzlin & B. C. Sanders. "Inconsistency in the Application of the Adiabatic Theorem". *Phys. Rev. Lett.* **93**, 160408 (2004)

[120] Y. Zhao. "Reexamination of the quantum adiabatic theorem". *Phys. Rev. A* **77**, 32109 (2008)

[121] D. M. Tong, K. Singh, L. C. Kwek & C. H. Oh. "Sufficiency Criterion for the Validity of the Adiabatic Approximation". *Phys. Rev. Lett.* **98**, 150402 (2007)

[122] R. MacKenzie, A. Morin-Duchesne, H. Paquette & J. Pinel. "Validity of the adiabatic approximation in quantum mechanics". *Phys. Rev. A* **76**, 44102 (2007)

[123] Z. Wu & H. Yang. "Validity of the quantum adiabatic theorem". *Phys. Rev. A* **72**, 12114 (2005)

[124] J. Du, L. Hu, Y. Wang, J. Wu, M. Zhao & D. Suter. "Experimental Study of the Validity of Quantitative Conditions in the Quantum Adiabatic Theorem". *Phys. Rev. Lett.* **101**, 60403 (2008)

[125] A. Szafer & A. D. Stone. "Theory of Quantum Conduction through a Constriction". *Phys. Rev. Lett.* **62**, 300 (1989)

[126] M. Büttiker. "Quantized transmission of a saddle-point constriction". *Phys. Rev. B* **41**, 7906 (1990)

[127] H. U. Baranger & A. D. Stone. "Electrical linear-response theory in an arbitrary magnetic field: A new Fermi-surface formation". *Phys. Rev. B* **40**, 8169 (1989)

[128] M. C. Payne. "Adiabaticity in quantum transport." *J. Phys. Condens. Matter* **1**, 4939 (1989)

[129] E. Tang. *Non-adiabaticity in quantum transport through nanostructures.* Master's thesis, University of Cambridge (2008)

[130] H. Benisty. "Reduced electron-phonon relaxation rates in quantum-box systems: Theoretical analysis". *Phys. Rev. B* **51**, 13281 (1995)

[131] U. Bockelmann. "Phonon scattering between zero-dimensional electronic states: Spatial versus landau quantization". *Phys. Rev. B* **50**, 17271 (1994)

[132] J. I. Climente, A. Bertoni, G. Goldoni & E. Molinari. "Phonon-induced electron relaxation in weakly confined single and coupled quantum dots". *Phys. Rev. B* **74**, 035313 (2006)

[133] C. G. Darwin. *Proc. Cambridge Philos. Soc.* **27**, 86 (1930)

[134] V. Fock. *Z. Phys.* **47**, 446 (1928)

[135] A. V. Madhav & T. Chakraborty. "Electronic properties of anisotropic quantum dots in a magnetic field". *Phys. Rev. B* **49**, 8163 (1994)

[136] M. Kataoka, M. R. Astley, A. L. Thorn, C. H. W. Barnes, C. J. B. Ford, D. Anderson, G. A. C. Jones, I. Farrer, D. A. Ritchie & M. Pepper. "Investigation of single-electron dynamics in tunnelling between zero-and one-dimensional states". *Physica E* **40**, 1017 (2008)

[137] M. R. Astley, M. Kataoka, C. J. B. Ford, C. H. W. Barnes, D. Anderson, G. A. C. Jones, I. Farrer, H. E. Beere, D. A. Ritchie & M. Pepper. "Examination of multiply reflected surface acoustic waves by observing acoustoelectric current generation under pulse modulation". *Phys. Rev. B* **74**, 193302 (2006)

[138] M. Kataoka, C. J. B. Ford, C. H. W. Barnes, D. Anderson, G. A. C. Jones, H. E. Beere, D. A. Ritchie & M. Pepper. "The effect of pulse-modulated surface acoustic waves on acoustoelectric current quantization". *Journal of Applied Physics* **100**, 063710 (2006)

[139] M. Stopa. "Quantum dot self-consistent electronic structure and the Coulomb blockade". *Phys. Rev. B* **54**, 13767 (1996)

[140] M. Stopa. "Single-mode quantum wires". *Phys. Rev. B* **53**, 9595 (1996)

[141] A. D. Greentree, J. H. Cole, A. R. Hamilton & L. C. L. Hollenberg. "Coherent electronic transfer in quantum dot systems using adiabatic passage". *Phys. Rev. B* **70**, 235317 (2004)

[142] G. Giavaras, J. H. Jefferson, M. Fearn & C. J. Lambert. "Generation of Einstein-Podolsky-Rosen pairs and interconversion of static and flying electron spin qubits". *Phys. Rev. B* **76**, 245328 (2007)